January 2018

Wireless Power Transfer For Biomedical Applications

Reem Shadid

Follow this and additional works at: https://commons.und.edu/theses

WIRELESS POWER TRANSFER FOR BIOMEDICAL APPLICATIONS

by

Reem Shadid
Bachelor of Science, University of Jordan, 2003
Master of Science, University of Jordan, 2015

A Dissertation

Submitted to the Graduate Faculty

of the

University of North Dakota
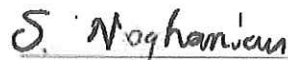
In partial fulfillment of the requirements

for the degree of

Doctor of Philosophy

Grand Forks, North Dakota
May
2018

This thesis, submitted by Reem Shadid in partial fulfillment of the requirements for the Degree of Ph.D. in Electrical Engineering from the University of North Dakota, has been read by the Faculty Advisory Committee under whom the work has been done and is hereby approved.

Sima Noghanian, Chairperson

Arash Nejadpak, Co-Chair,

Kouhyar Tavakolian, Committee Member,

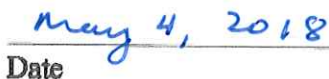Reza Fazel-Rezai, Committee Member,

Aaron Kennedy, Member-at-Large,

This thesis is being submitted by the appointed advisory committee as having met all of the requirements of the School of Graduate Studies at the University of North Dakota and is hereby approved.

Dr. Grant McGimpsey
Dean of the School of Graduate Studies

May 4, 2018
Date

PERMISSION

Title   Wireless power transfer for biomedical applications

Department Electrical Engineering

Degree   Doctor of Philosophy

   In presenting this dissertation in partial fulfillment of the requirements for a graduate degree from the University of North Dakota, I agree that the library of this University shall make it freely available for inspection. I further agree that permission for extensive copying for scholarly purposes may be granted by the professor who supervised my dissertation work or, in her absence, by the Chairperson of the department or the dean of the School of Graduate Studies. It is understood that any copying or publication or other use of this dissertation or part thereof for financial gain shall not be allowed without my written permission. It is also understood that due recognition shall be given to me and to the University of North Dakota in any scholarly use which may be made of any material in my dissertation.

<div align="right">

Reem Shadid
May 7th, 2018

</div>

ACKNOWLEDGMENT

ABSTRACT

In this research wireless power transfer using near-field inductive coupling is studied and investigated. The focus is on delivering power to implantable biomedical devices.

The objective of this research is to optimize the size and performance of the implanted wireless biomedical sensors by: (1) proposing a hybrid multiband communication system for implantable devices that combines wireless communication link and power transfer, and (2) optimizing the wireless power delivery system. Wireless data and power links are necessary for many implanted biomedical devices such as biosensors, neural recording and stimulation devices, and drug delivery and monitoring systems.

The contributions from this research work are summarized as follows:

1. Development of a combination of inductive power transfer and antenna system.

2. Design and optimization of novel microstrip antenna that may resonate at different ultra-high frequency bands including 415 MHz, 905 MHz, and 1300MHz. These antennas may be used to transfer power through radiation or send/receive data.

3. Design of high-frequency coil (13.56 MHz) to transfer power and optimization of the parameters for best efficiency.

4. Study of the performance of the hybrid antenna/coil system at various depths inside a body tissue model.

5. Minimizing the coupling effect between the coil and the antenna through addressed by optimizing their dimensions.

6. Study of the effects of lateral and angular misalignment on a hybrid compact system consisting of coil and antenna, as well as design and optimize the coil's geometry which can provide maximum power efficiency under misalignment conditions.

7. Address the effects of receiver bending of a hybrid power transfer and communication system on the communication link budget and the transmitted power.

8. Study the wireless power transfer safety and security systems.

TABLE OF CONTENTS

LIST OF FIGURES

LIST OF TABLES

21

ABBREVIATIONS

AM	Amplitude Modulated
EV	Electrical Vehicle
EX	External antenna/coil combination
GSM	Global System for Mobile
IFAC	Institute of Applied Physics
IM	Implanted antenna/coil combination
IPT	Inductive Power Transfer
KAIST	Korea Advanced Institute of Science & Technology
LOS	Line of Sight
MIT	Massachusetts Institute of Technology
PSC	Printed Spiral Coil
PTE	Power Transfer Efficiency
RF	Radio Frequency
RFID	Radio Frequency Identification
RX	Receiver Coil
SAR	Specific Absorption Rate
SRF	Self-Resonance Frequency
TX	Transmitter Coil
WPC	Wireless Power Consortium
WPT	Wireless Power Transfer

1 INTRODUCTION

Wireless Power Transfer (WPT) refers to the technology of transmitting electric power without connecting wires. There are many techniques that have been developed to transfer power wirelessly using optical methods, ultrasound, and Radio-Frequency (RF). However, wireless powering through RF electromagnetic waves is the most established one. WPT is important for applications where the interconnecting wire is not possible, is too hard and inconvenient, or can casue saftey problems. Providing wireless power can elp reducing toxic material waste resulted from disposing of 6 billion batteries each year used for battery-operated electronic devices (e.g. laptops, mobile devices, and toys) [1].

1.1 History of Wireless Power Transfer

In 1820 Han Oersted, during a lecture, noticed a needle deflection of a compass when electric current flows in one wire cable which proved the magnetic effect of electricity. In 1826, Andre-Marie Ampere, through his circuital law, formulated the relationship between electric current and the produced magnetic field. In 1831 discovery of Faraday's law described that the electromagnetic force could be induced in a conductor by varying a magnetic flux. In 1888, Heinrich Hertz confirmed that electromagnetic radiation exists. In 1891 Nicola Tesla improved Hertz's wireless transmitter and registered it as a patent [2].

In 1894 Hutin and Leblanc's patent on wireless power transmission at 3kHz was issued [3]. In the same year, Tesla successfully energized a light lamp using a pair of coils, as shown in Fig. 1.1, [4]..
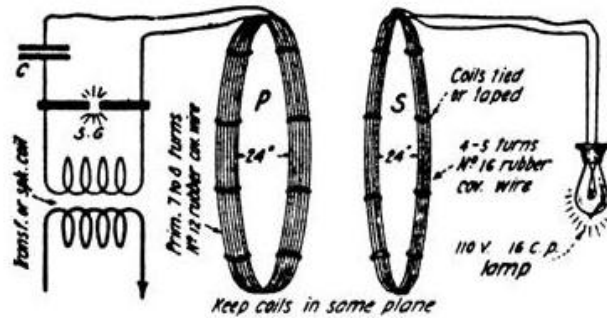
Fig. 1.1. The electrical model of the planar spiral inductor [4].

In 1895, Jagdish Bose was able to ring a bell remotely from 75 feet distance through a wall using electromagnetic wave. Marconi successfully sent radio transmission over distance 1.5 miles in 1896. Tesla performed wireless power transmission to 48 km distance [5].

In 1904, a prize was offered for a successful attempt to drive a 0.1 horsepower (75W) airship motor by energy transmitted through space at a distance greater than or equal to 100 feet [6]. In 1926 Yagi and Uda invented their high gain directional array antenna. In 1960, William Brown published his article about possibilities of microwave power transfer and demonstrated a helicopter model that receives the microwave beam [7]. In 1968, Peter Glaser demonstrates the principle of solar power satellite through his proposal, showng that the wireless energy transmitted from the Sun could be captured [8]. In 1973, the first passive system of Radio Frequency Identification (RFID) receivers in Los Alamos National Lab was energized by electrodynamic induction from a few feet distance. WPT research between 2001-2013 is summarized in [9], with a citation for more than 50 papers.

According to [9], the most productive authors are Fu and Imura.The authors find the top four active countries in this field are USA, South Korea, China, and Japan.

In [10] the history of WPT is summarized and a literature survey for the non-radiative and radiative power transfer methods is provided. This summary is also provided in Section 1.2.

1.2 Types of Wireless Power Transfer

WPT methods are classified into two categories depending on the mechanism of energy transfer: (1) non-radiative, and (2) radiative [11].

1.2.1 Non-Radiative Power Transfer

In order to consider any region to be non-radiative or near-field (short- and medium-range) the following condition should be satisfied: if the maximum diameter of both the transmitter and receiver (D_{max}) is shorter than half of the operating wavelength (λ) or $D_{max} < \lambda/2$, the near-field region operates at transfer distance (r) less than λ ($r < \lambda$). If $D_{max} > \lambda/2$ the near-field region is defined where $r < 2D_{max}^2/\lambda$ [6].

Non-radiative power transfer is divided into two categories, as follows.

A. *Short-Range Non-Radiative Power Transfer*

Short-range non-radiative power transfer refers to the case of transferring power within a distance less than the maximum diameter of the coil ($r < D_{max}$). Two techniques are used to transfer power wirelessly in this range:

- *Inductive Coupling:*

    Inductive coupling is the process of transferring power by connecting a source generating a varying magnetic field to a primary coil that induces a voltage across the receiver secondary coil, which transfers the power to the load accordingly. More details about this method are explained in section 1.3.2.

- *Capacitive Coupling:*

    In capacitive coupling, energy is transferred through the electric field (*E*) between two electrodes [6]. The amount of transferred energy increases with increasing frequency. It has the capability of transferring power through metals. This method has been used for low-power devices, due to hazardous issues when a high-voltage is applied to the electrodes. Additionally, many materials are strongly affected by high-power electric fields, including the human body. This yields limitation in using this technology in biomedical applications.

    There are two types of circuits that are used for capacitive coupling: (1) transverse of bipolar design, where the receiving plates should always be aligned to the charging plates, and (2) longitudinal or unipolar design.

B. Medium Range Non-Radiative Power Transfer

A region is considered to be in mid-range if the power transfer distance varies from one to ten times the maximum diameter of the transmitting coil ($D_{max} < r < 10\ D_{max}$) [12]. Its operating frequency usually ranges between 10 kHz–200 MHz. Two, three, and four coil-systems have been used for this range [11]. This method can be used to energize and

transfer power to devices utilized in residential or office environments. Resonant inductive or capacitive coupling power transfer method falls under this type.

The use of resonant frequency principle has been favored because it reduces the leakage, and therefore, it allows transferring the power to a further distance. In [13], a research team from Massachusetts Institute of Technology (MIT) explained the magnetic resonance coupling method to transfer power. In the same paper, they also reported their implementation of two identical helical copper coils ($D_{max} = 25\ cm$) to transfer 60 W power to a light bulb at 2 m distance (4 times the diameter of the coil), with 40% efficiency. This team used 9.9 MHz resonant frequency. Colpitts oscillators waere used as the source coil and their schematic diagram is shown in Fig. 1.2. In the same paper, authors suggested that the efficiency could be improved by silver-plating the coils. They also noticed the possibility of making the coil small enough to fit into a portable device without decreasing the system's efficiency.
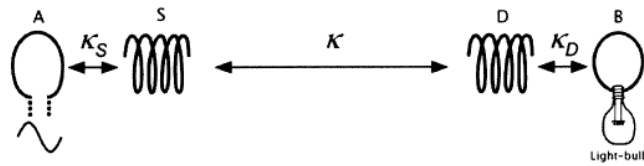
Fig. 1.2. Schematic diagram for MIT experiment [13].

Using magnetic resonant coupling to transfer power to multi-receivers is reported in [14]. Authors set up a magnetic resonant coupling experiment with one large source coil to generate a signal at the frequency of 8.3 MHz. Multiple resonant coil receivers were made using lumped capacitors at the terminal in order to match them to the resonant

frequency. It was shown that the efficiency was increased by adding the matching capacitors.

In [15], the relationship between the frequency between (11 MHz–17 MHz) and power efficiency was studied using electromagnetic field analysis for different air-gap separations for a magnetic coupling resonance circuit. The authors also studied the relation between the maximum efficiency (η_{21}) and the air-gap separation. Their results showed that two resonant frequencies appeared for 49 cm and 80 cm air-gaps, and one resonant frequency happened for 170 cm and 357 cm air-gaps. The peak efficiencies versus different air-gaps are shown in Fig. 1.3 .
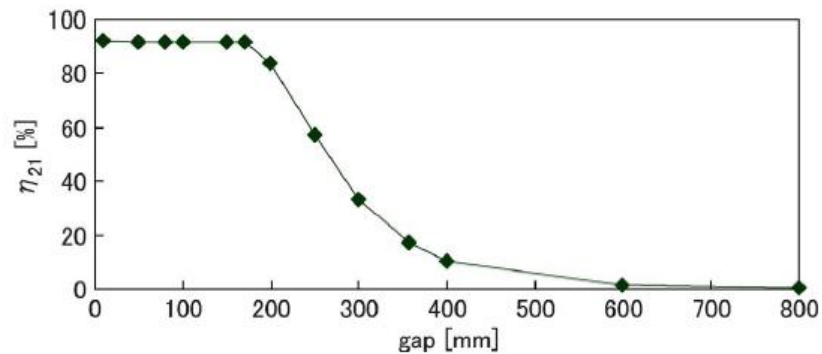
Fig. 1.3. Peak efficiency versus air-gap separation [15].

A team of researchers from Korea Advanced Institute of Science and Technology (KAIST) University proposed a 20 kHz frequency Inductive Power Transfer (IPT) resonant system [16]. They used dipole structure coil with a ferrite core. The core was long and narrow to be easily installed on the ceiling or the corner of a room. The overall configuration is shown in Fig. 1.4. The maximum output power for 3 m, 4 m, and 5 m, at

20 kHz frequency were 1403 W, 471 W, and 209 W, respectively. The efficiency was 29%, 16%, 8% for each distance, respectively.
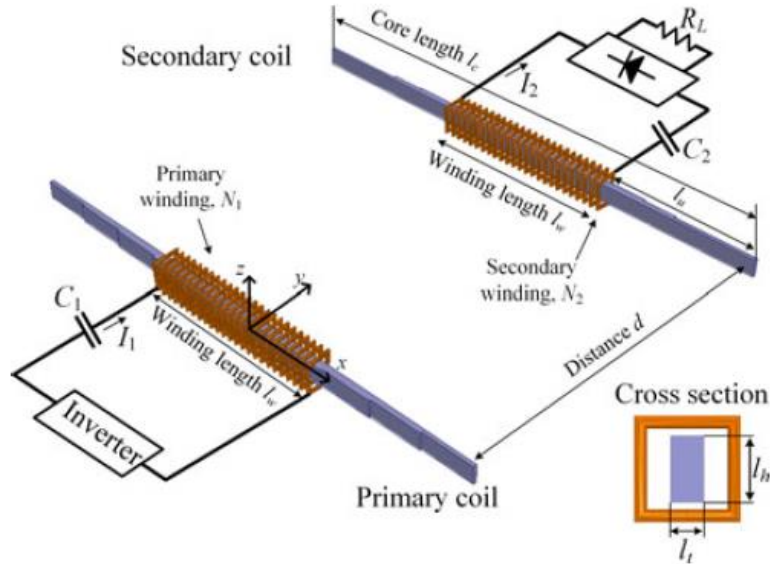
Fig. 1.4. Overall configuration the system proposed in [16].

1.2.2 Radiative Power Transfer

Radiative power transfer, or far-field power transfer, uses the propagation of electromagnetic waves in the far-field, where $r > 2\lambda$ for $D_{max} < \lambda/2$, or $r > 2D_{max}^2/\lambda$ if $D_{max} > \lambda/2$. Two types of radiative power transfer are used: directive and non-directive. Microwaves with frequencies 300 MHz – 300 GHz and laser (ten of a micrometer to nanometer wavelength) are used to transmit far-field power. For microwave propagation, rectennas are used to convert the received microwave signals to DC power. A review of WPT using this method can be found in [17]. In this method delivering power to a device is done using antennas. In [18], microwave power transfer at 2.45 GHz frequency was proposed to be used to transfer solar power from satellites. This study showed that the size

of transmitter antenna should be at least 1 km, where the rectenna size at receiver needs to be 10 km, which is impractical. It was stated that increasing frequency can minimize the antenna dimension but the drawback would be the effect of the atmospheric absorption of the waves. Recently, directive microwave was used to send power to Electric Vehicles (EVs) [19]. It was suggested that a roadside system that utilizes directed power transmitter sends power to a rectenna, to collect 10 kW power with 80% efficiency conversion to energize EVs [20]. Commercializing these systems is expensive depending on design and infrastructure. Additionally, the electromagnetic compatibility for these systems should be considered. In [21], [22] it is claimed that the mobile devices could be powered through high-frequency microwaves,

(e.g. 60 GHz). However, the practicability requires further experimental evaluation.

For a non-directive application, omnidirectional RF broadcast may be used to transfer power to portable devices. In [23], [24] it is discussed that if the energy is transmitted omni-directionally, the same way as the radio signals are transmitted, it can be used for powering ultra-low-power microcontroller, for up to 10 m of operating range. Usually, the limitations on the achievable efficiency prevent us from using directional RF power transfer technology.

RF beam with power densities between 20200 μW/cm^2 can be utilized to wirelessly charge sensor networks, using non-directive RF charging. In [25] the authors implemented transmitter with 1.79 mW power to 0.68 mW receiver for an ultra-low power sensor platform, powered by far-field method, to achieve the data rate of 500 kbps. Also,

similar work has been done for wirelessly charging sensors with batteries as presented in [26], [27].

RF energy harvesting is another technology to convert ambient RF radio wave to DC power. RF power harvesting usually providing power at the level of milli-Watts to micro-Watts. Power harvesting is used for low power sensors and electronic devices and calculators. Some of these systems have been commercialized (e.g. TX91501 power caster transmitter and P2210 power harvester). More detailed review of harvesting technologies can be found in [28], [29].

Ambient waves have many forms [30]. In [31], authors used TV broadcasting signals to collect energy. In other papers there are published results of using other sources of ambient waves such as Amplitude Modulated (AM) radio broadcast waves [32], 900 MHz and 1800 MHz bands of Global System for Mobile (GSM) communications [33], WiFi transmission signal [34], the signal power from cellular base stations [35], and satellites' electromagnetic waves [36], [37].

The challenge in using far-field systems is the improvement of directivity and efficiency. Although many systems have been built using microwave with high gain antennas to transfer power over kilometer distance with 90% efficiency range [38], these systems still suffer from the need for Line of Sight (LOS) (point-to-point) connection. Furthermore, there is a need to transfer power using omnidirectional antennas to cover more areas.

Summarization of methods to transfer power wirelessly are shown in Table 1.1.

Table 1.1. Electromagnetic properties at 13.56 MHz

	Categories	Range	Transferring Method	Frequency Range	Penetration	Efficiency	Drawbacks	Flexibility in Moving	Advantage
Wireless Power Transfer	Non-Radiative (Near-Field)	Short-Range	Inductive Coupling	10kHz-1MHz	Strong	High	Induce Eddy current through metal	Depending on design of charging pad	High efficiency
			Capacitive Coupling	High Frequency	Strong	High	Strongly interact with materials and human body	Less flexibility for load location	Could be transferred through metal
				Low Frequency			Require large coupling area		
		Mid-Range	Resonant Inductive Coupling	10kHz-200MHz	Medium	Medium	Maximum efficiency when impedances are matching cannot exceed 50% also using operating frequency larger 10MHz will increase the cost and switching losses	Used for portable devices	High efficiency for few centimeters to few meters Charging multiple devices simultaneously
			Resonant Capacitive Coupling						
	Radiative (Far-Field)	Long Range	RF/Microwave	300MHz-300GHz	Weak	Weak	Need directivity to transfer power (point – point) and in case of Omni-directional efficiency will be low	Less flexibility for load location in case of LOS.	Useful for mobile devices when using omnidirectional RF range
			Laser Photo Electricity	Millimeter to Micrometer wavelength (frequency up to ten of THz)	Weak	Weak	Harmful radiation	Require a direct LOS with the receiver	Transmitted for large distance usually from several meters to several kilometers

1.3   Wireless Power Transfer for Biomedical Devices

WPT systems for biomedical devices have the same general structure despite their varieties. This structure consists of three components: power transmitter, power receiver, and possibly a middle power resonator. This structure is shown in Fig. 1.5 [6]. For the first component, the power transmitter is located in the air outside the human body. It is possible to be worn or placed in the surrounding area. The power transmitter circuit consists of primary power antenna, tuning circuit, a DC-AC converter that enables the transfer of power at the proposed operating frequency, a DC-DC converter (linear regulator) and a power management that allows the data connectivity to send data to the receiver, and also as a feedback to receive information sent by the receiver.
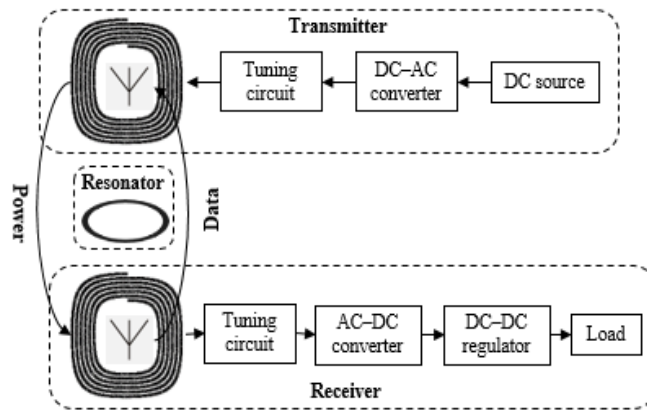
Fig. 1.5. Model of WPT system for biomedical device [6].

For the second component, the power receiver is implanted inside the body below the tissue or even patched on human skin. The receiver receives the wireless power and provides a stable energy for the load or use the energy to charge a battery. The receiver circuit consists of a secondary power antenna, a tuning circuit, an AC–DC converter, a DC-DC converter (regulator), and a power management unit to interact with the transmitter.

14

For the third (possible) component, the middle power resonator is used as a third part to resonate at the operating frequency and to help in delivering the power to places at further distances. This component is possible to be worn or embedded inside the human body.

The main goal to for any WPT system design is to transfer power with high efficiency and stability. The following subsections describe the implantable devices, inductive coupling WPT, and literature review of research on the biomedical power transfer power based on inductive coupling method.

1.3.1 Implantable Devices

Implantable devices are widely used in various biomedical applications such as cochlear implants, cardiac defibrillators, electrocardiogram (ECG) implanted recorders and pacemakers. These devices are mainly powered by a battery. Implantable devices interact with physiological processes including sensing, drug delivery, and stimulation, to monitor or influence their progression. However, minimizing the size of implanted devices make them more suitable to be installed on the small corporeal cavities and narrow channels inside the human body. While recent progress in microfabrication has dramatically minimized the size of electronic and mechanical components, electrochemical energy storage has been much slower to miniaturize. In most of the existing devices, the battery constitutes the bulk of the implant [39]. However, every time batteries need to be replaced, new surgical procedures have to be performed [6]. Moreover, possible failure of the *in-vivo* batteries, which are mainly made of Lithium Iodine substances, may lead to catastrophic damage to the organs and/or living cells.

Most biomedical devices applications use operating frequencies in the range of 100 kHz to 50 MHz for power transfers. Comparing the wavelength at this range (3000 m–6 m in vacuum) with the typical transmission distance which is between 1 cm–11 cm, the corresponding wavelength of the electromagnetic field is relatively much longer than the transmission distance. Therefore, the system is working in the near-field [6].

1.3.2 Inductive Coupling Concept for Wireless Power Transfer

An Inductive Power Transfer (IPT) system consists of two coils referred to as primary transmitter and a secondary receiver. Fig. 1.6 shows the system model.
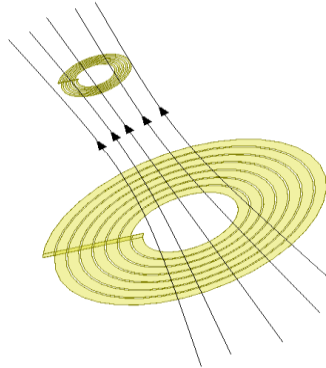
Fig. 1.6. Inductive coupling principle.

Power transfer occurs when a primary source generates varying magnetic fields H, that induce voltage V at the secondary receiver:

$$V = -N\frac{d\Phi}{dt} = iN\omega\Phi = iN\omega\mu \int \vec{H}.\vec{ds} \tag{1.1}$$

Where N is the number of turn, ω is the operating angular frequency, Φ is the magnetic flux linkage, and μ is the permeability of transfer medium. According to (1.1) coupling

between coils depends mainly on the amount of Φ between the primary and secondary coils. Decreasing the distance between the primary transmitter and the secondary receiver while increasing the area of the coupling helps to increase the amount of coupled magnetic flux.

The advantages of inductive WPT include its low-cost and high-efficiency. The drawbacks are: (1) the amount of power is limited to the coil geometries, (2) the power transmission is achieved at limited distances; and (3) the lateral and angular misalignment between the transmitter and receiver coil antenna is not completely controllable. Misalignments can cause efficiency loss.

1.3.3 History of Wireless Power for Biomedical Devices

The first developed inductive WPT links for biomedical applications was introduced in the 1960s' and focused on an artificial heart system [40]. Since then many implantable devices have used similar methods for power transfer. In 1970's, IPT was used in other biomedical applications [41]–[50]. Research in that field continues to be developed. Tables 1.2, 1.3, and 1.4 summarizes the comparison and information about these systems that are proposed in the literature, that includes a collection of research papers on the topic of WPT based on IPT technology for biomedical applications. Research papers are sorted in a descending order based on the year they were published, so the most recent research is mentioned first. If two papers have the same year of publication, they are sorted based on the operating frequency (from a higher frequency to lower frequency in a descending order).

Table 1.2. Implantable power device modeled in tissue.

Ref	Journal	Year	Freq	Power [mW]	Optimization method for Inductor dimension	Transmitter Dimension [mm²]	Receiver Dimension [mm²]	Gap [mm]	Efficiency [%]	Simulation Model
[51]	IEEE Transactions on Power Electronics	2015	800 KHz	30e3	Based on method in [52]	d_{outT} = 83.2 d_{inT} = 59.6 Circular (CST MWS)	d_{outT} = 24.2 d_{inT} = 19.2 Circular (CST MWS)	20	95	One layer of Skin (effect on simulation calculated)
[53]	IEEE Transactions on Biomedical Circuits and Systems	2015	200 MHz	0.224	Based on flowchart in same paper	d_{outT} = 70 d_{inT} = 34 Circular Litz wire (FE)	d_{outR} = 70 d_{inR} = 34 Circular Litz wire (FE)	12	0.56	the link was wrapped in a 10 mm thick layer of beef
[54]	Sensors (Switzerland)	2014	13.56 MHz	150	Based on method in [55]	d_{outT} = 24 Printed Hexagon (HFSS)	d_{outR} = 1 Wire wound (HFSS)	6	32 to 80	Three layer of 70×60×6mm 1mm skin, 2mm fat & 3mm Muscle
[56]	IEEE Transactions on Industrial Electronics	2014	8.1 MHz	29.8~ 93.3	Optimization for frequency has been done	d_{outT} = 56 d_{inT} = 10 Printed Spiral (Matlab, HFSS, FE & SEMCAD)	d_{outR} = 11.6 d_{inR} = 0.5 Printed Spiral (Matlab, HFSS, FE & SEMCAD)	12~20	47.6 to 65.4	Various type of tissue including blood
[57]	2013 Proceedings of the ESSCIRC (ESSCIRC)	2013	160 MHz	>183	Based on method in [58], [59]	d_{outT} = 30 Printed Square (HFSS)	d_{outR} = 20 Printed Square (HFSS)	10	0.8	7.5mm of Muscle layer and 2.5mm air
[60]	IEEE Transactions on Circuits and Systems	2013	13.56 MHz	10	Based on method in [61]	d_{outT} = 14.5 Printed Square (Momentum EM & HFSS)	d_{outT} = 2.2 Printed Square (Momentum EM & HFSS)	10~50	0.16 to 58.2	Two layers of pork tissue in front and behind Receiver
[59]	IEEE Electron Device Letters	2013	6.78 MHz	10	Based on method in [62]	60×25 Printed Rectangle (HFSS & CST EM)	25×10 Printed Rectangle (HFSS & CST EM)	5 & 12	23.8 & 4.2	One layer of Muscle tissue
[63]	IEEE Trans Biomed Circuit Sys	2009	13.56 MHz		Based on method in [61]	d_{outT} = 20 Printed square (HFSS)	d_{outT} = 4.5 Printed square (HFSS)	10	30.84	Two layer of Muscle in front and behind Receiver
[64]	IEEE Transactions on Biomedical Circuits and Systems	2007	6.785 MHz	1~10	Based on flow chart in same paper	d_{outT} = 24 d_{inT} = 9.4 Printed Square (HFSS)	d_{outR} = 10 d_{inR} = 7.2 Printed Square (HFSS)	1~10	51 to 74	One layer of skin (effect)
[65]	2007 IEEE International Symposium on Circuits and Systems	2007	6.78 MHz	<100	dinT≈ 0.18doutT dinR≈ 0.75doutR	d_{outT} = 30 Circular Litz wire	d_{outR} = 30 Circular Litz wire	15	10 to 20	Mentioned as body tissue (Effect)
[66]	IEEE Transactions on Circuits and Systems	2005	1 MHz	250	Geometric and frequency dependent coil effective (ESR) series resistance formulations	d_{outT} = 40 Circular Litz wire	d_{outT} = 22 Circular Litz wire	7	67	A tissue through retinal prosthesis
[67]	IEEE Transactions on Circuits and Systems	2005	1 MHz	>250	by allocating lower frequency for the power and higher frequency for forward data carriers	d_{outT} = 40 d_{inT} = 32 Disk	d_{outR} = 22 d_{inR} = 18 Disk	7 & 15	33.3 to 65.8	A tissue through retinal prosthesis
[68]	Sensors and Actuators, A: Physical	2004	700 KHz	50	using a self-developed design tool and equations in paper itself	d_{outT} = 60 Pancake/Disk	d_{outR} = 20 Solenoid	30	36	One layer of Skin (effect)

Table 1.3. Implantable power device modeled in air.

Ref	Journal	Year	Frequency	Output power [mW]	Optimization method for the inductor dimension	Transmitter Dimension [mm]	Receiver Dimension [mm]	Gap [mm]	η [%]	Simulation Model
[53]	IEEE Transactions on Biomedical Circuits and Systems	2015	200 MHz	0.224	Follow flow chart in the paper	d_{outT} = 24 Printed Hexagonal (HFSS)	d_{outR} = 1 Wire wound (HFSS)	12	1.02	Air
[57]	European Solid State Circuit Conference (ESSCIRC)	2013	160 MHz	>183	Based on the method in [58], [59]	d_{outT} = 14.5 Printed Square (Momentum EM & HFSS)	d_{outT} = 2.2 Printed Square (Momentum EM & HFSS)	10	1.5	Air
[69]	Hindawi: Active and Passive Electronic Components	2012	211.9 KHz	125	Based on the method in [68]			10	12.5	Air
[70]	Proceedings of the Annual International Conference of the IEEE Engineering in Medicine and Biology Society, EMBS	2011	13.56 MHz	27	Based on the method in [61]	d_{outT} = 27 d_{inT} = 11 Printed Spiral	12×10 Rectangle Wire wound litz	7		Air, worn as a jacket on back of a rat
[71]	IEEE Transactions on Biomedical Circuits and Systems	2011	13.56 MHz	49.5	Follow flow chart in the paper	2-Coil d_{outT} = 37 Printed Spiral (HFSS)	2-Coil d_{outR} = 10 Printed Spiral (HFSS)	10	75.7	Air
				43.4		3-Coil d_{outT} = 43 Printed Spiral (HFSS)	3-Coil d_{outR} = 10 Printed Spiral (HFSS)		78.6 3-Coil	
				3.9		4-Coil d_{outT} = 36.5 Printed Spiral (HFSS)	4-Coil d_{outR} = 10 Printed Spiral (HFSS)		83.5 4-Coil	
[72]	ELSEVIER: Procedia Engineering	2011	1 MHz	380		Area = 1000mm^2 Spiral Litz wire	Area = 520mm^2 Spiral Litz wire	10	50	Air
[73]	IEEE Transactions on Bio Circuits and Systems	2011	700 KHz	100	Follow flow chart in the paper	d_{outT} = 64 Spiral Litz wire (Spice)	d_{outR} = 22 Spiral Litz wire (Spice)	20	82	Air
[74]	2010 3rd International Symposium on Applied Science in Biomedical and Communication Technology	2010	27 MHz	794	Coil built based on [75], no optimization used		d_{outR} = 15 Square (CST MWS)	15	80	Air
[76]	IEEE Transactions on Circuits and Systems	2010	13.56 MHz	11.2	Based on the method in [77]	d_{outT} = 20 d_{inT} = 10 Printed Square	d_{outR} = 10 d_{inR} = 6 Printed Square	5~20	1 to 14.1	Air
[78]	IEEE Transactions on Biomedical Circuits and Systems	2010	13.56 MHz		Based on the method in [61]	d_{outT} = 79 d_{inT} = 11.2 Printed Square (HFSS)	d_{outR} = 10 d_{inR} = 2.96 Printed Spiral (HFSS)	10	56.65	Air
[79]	IEEE International Solid-State Circuits Conference	2009	13.56 MHz	7.05	Based on the method in [61]	d_{outT} = 168 Printed Hexagon (HFSS)	d_{outR} = 30 Wire wound Solenoid (HFSS)	70	80.2	Air
[68]	ELSEVIER Sensors and Actuators	2004	700 KHz	50	Using a self-developed design tool and equations	d_{outT} = 60 Panca];pke/Disk (FastHenry and Matlab)	d_{outR} = 20 Solenoid (FastHenry and Matlab)	30	36	One layer of skin

Ref	Journal	Year	Frequency	Output power [mW]	Optimization method for Inductor dimension	Transmitter Dimension [mm²]	Receiver Dimension [mm²]	Gap [mm]	η [%]	Simulation Model
[63]	IEEE Transaction Biomedical Circuit System	2009	13.56 MHz		Based on the method in [61]	$d_{outT}=38$ $d_{inT}=14.9$ Printed Square (HFSS)	$d_{outR}=10$ $d_{inR}=5.8$ Printed Square (HFSS)	10	72.22	Air
[65] [61]	2007 IEEE International Symposium on Circuits and Systems IEEE Transactions on Circuits and Systems	2007 2007	6.78 MHz 1 MHz	<100	$d_{inT}\approx 0.18d_{outT}$ $d_{inR}\approx 0.75d_{outR}$ Follow flow chart in the paper	$d_{outT}=52$ $d_{inT}=10$ Printed Spiral $d_{outT}=69$ $dinT=8$ Printed Square (HFSS)	$d_{outR}=10$ $d_{inR}=5$ Printed Spiral $doutR=20$ $dinR=8$ Printed Square (HFSS)	15 10	10 to 20 41.2	Air Air
[80] [80]	IEEE Transactions on Circuits and Systems IEEE Transactions on Circuits and Systems	2007 2007	5 MHz 125 KHz 125 KHz	810 125	Based on method in [81] Based on the method in [81]	$d_{outT}=70$ $d_{inT}=8$ Printed Square (HFSS) $d_{outT}=36$ $d_{inT}=13$ Spiral Litz wire (Fast-Henry-2) $d_{outT}=64$ $d_{inT}=14$ Spiral Litz wire (Fast-Henry-2)	$d_{outR}=20$ $d_{inR}=8$ Printed Square (HFSS) $d_{outR}=26$ $d_{inR}=12$ Spiral Litz wire (Fast-Henry-2) $d_{outR}=22$ $d_{inR}=6$ Spiral Litz wire (Fast-Henry-2)	10 10 18	85.8 50 50	Air
[81] [81]	IEEE Transactions on Biomedical Engineering IEEE Transactions on Biomedical Engineering	1996 1996	500 KHz 2 MHz		Based on method in [82] $d_{inT}\approx 0.4d_{outT}$	$d_{outT}=44$ $d_{inT}=14$ Spiral Litz wire (Fast-Henry-2) $d_{outT}=24$ $d_{inT}=22.5$ Spiral $d_{outT}=15.86$ $d_{inT}=13.58$ Spiral	$d_{outR}=22$ $d_{inR}=7$ Spiral Litz wire (Fast-Henry-2) $d_{outR}=24$ $d_{inR}=22.5$ Spiral $d_{outR}=15.86$ $d_{inR}=13.58$ Spiral	10 1~25	29.9 5 to 90	Air
[83], [84]	IEEE Transactions on Power Electronics	1992	53~123 KHz	48e3	Based on method in [85], [86]	$d_{outT}=24$ with 3.55 Turn Spiral	$d_{outR}=24$ with 3.55 Turn Spiral	10~20	72 to 76	Air
[83], [84]	IEEE Transactions on Power Electronics	1992	53~123 KHz	48e3	Based on the method in [85], [86]	Area = 37mm²	Area = 37mm²	10~20	72 to 76	Air

Table 1.4. Other model of implantable power device.

Ref	JOURNAL	Year	Frequency	Output power [mW]	Optimization method for inductor dimensions	Transmitter Dimension [mm²]	Receiver Dimension [mm²]	Gap [mm]	η [%]	Simulation Model
[57]	European Solid State Circuit Conference (ESSCIRC)	2013	160 MHz	>183	Based on the method in [58], [59]	$d_{outT}=14.5$ Printed Square (Momentum EM & HFSS)	$d_{outT}=2.2$ Printed Square (Momentum EM & HFSS)	10	1	7mm of 0.2 molar NaCl layer and 3mm air
[87]	IEEE Transactions on Biomedical Engineering	2012	13.56 MHz	24	Based on the method in [88][13]	$d_{outT}=480$ Circular Built under floor	Capsule 13×27	1000	3.04	Endoscopic capsule
[89]	ELSEVIER: Procedia Engineering	2010		300			Capsule 16×28	Free move		Endoscopic capsule
[63]	IEEE Transaction Biomedical Circuit System	2009	13.56 MHz		Based on the method in [61]	$d_{outT}=30$ $d_{inT}=11.1$ Printed Square	$d_{outR}=10$ $di_{nR}=5.5$ Printed Square	10	51.8	Saline

A. *Efficiency and Frequency*

Fig. 1.7 shows the output or delivered power versus efficiency that the receiver collects it from the transmitter for the papers listed in Tables 1.2, 1.3, and 1.4. It should be noted that the efficiency increases at high delivered power. However, various efficiencies may have been achieved for the same delivered power depending on the system design.
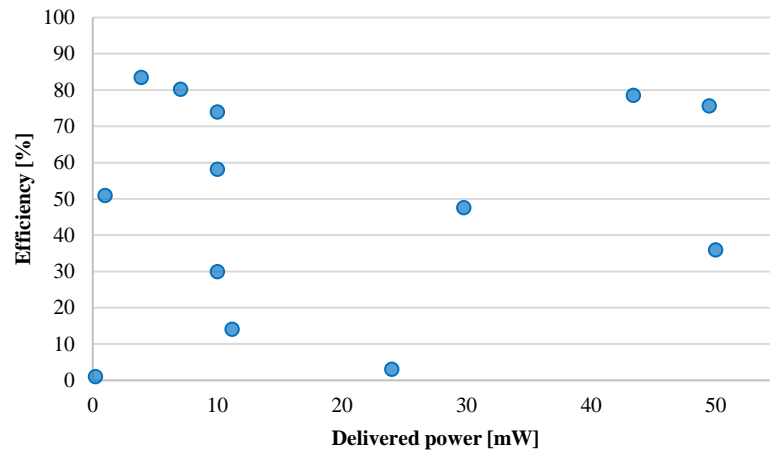
Fig. 1.7. Efficiency vs delivered power for various biomedical devices listed in Tables 1.2, 1.3, and 1.4.

Fig. 1.8 shows the frequency versus efficiency. It is clear that the frequency range for most biomedical applications is below 50 MHz for the papers in this survey.

21
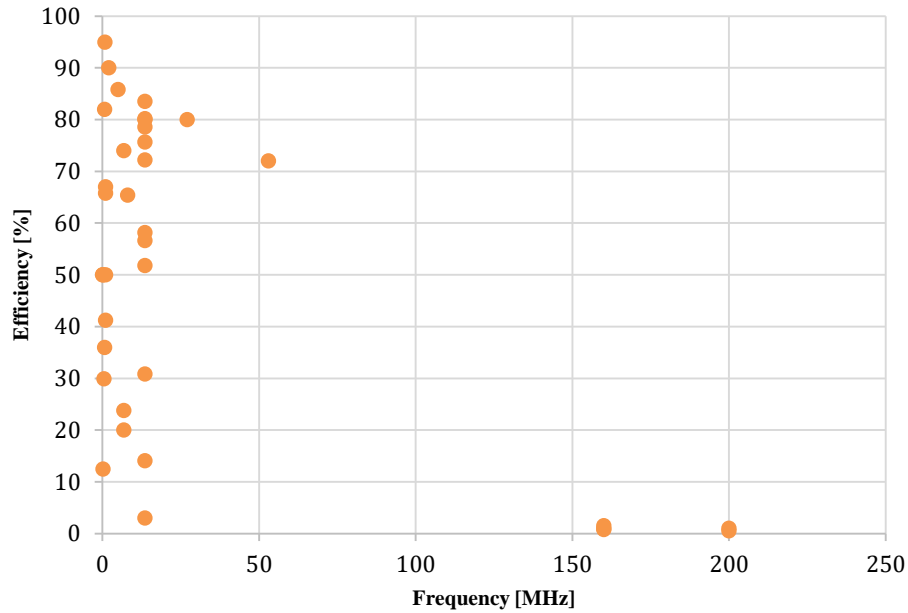
Fig. 1.8. Efficiency vs frequency for the research listed in Tables 1.2, 1.3, and 1.4.

B. *Optimization Methods*

The sixth column of Tables 1.2, 1.3, and 1.4 indicates the optimization method that each paper performed. Collected research in [60]–[79] of Tables 1.2, 1.3, and 1.4 use the optimization method described in [61]. This optimization method is used when the operating frequency of the design is known. This method applies five steps to optimize the dimensions of the transmitter and receiver antenna. The first step is to apply the design constraints for the receiver. The second step is to set the initial values for coils dimensions based on fabrication limitation. The third step is to optimize the size and fill-factor for the transmitter coil. The fourth step is to set the line width and fill-factor for the receiver coil side. The fifth step returns back to the third step and resets the size and line width of the transmitter side. After that, the third, fourth and fifth steps are repeated iteratively until the

22

value of the required tolerance of the efficiency value is achieved, this study didn't consider the misalignment effects during optimization.

In [54] Harrison's method to optimize the coil size [65] is used for designing coils with planar spiral pancake shapes. In [65] it was assumed that the inner transmitter diameter (d_{iTX}), outer transmitter diameter (d_{oTX}), inner receiver diameter (d_{iRX}) and outer receiver diameter (d_{oRX}) are possible to be optimized by considering $d_{iTX} = 0.18 \times d_{oTX}$ and $d_{iRX} = 0.75 \times d_{oRX}$. The paper results are based on an experimental study which was conducted using multiple coils, and measuring the dimensions at the maximum achieved efficiency.

Collected research in [72]–[89] of Tables 1.2, 1.3, and 1.4 didn't use any optimization process to calculate the geometries of coils.

1.4 Research Objective

In this research WPT using near-field inductive coupling was considered to deliver power to implantable biomedical devices. The WPT system consists of a transmitter and receiver coils. The assumption is that the transmitter is located on the skin layer outside the body. The receiver is implanted deep into the body under the fat layer.

This research presents a design methodology to transfer power wirelessly to centimeter-sized implantable biomedical devices. Optimization takes into account the effect of lateral and angular misalignment between the transmitter and receiver coil. The optimal operating frequency and coil geometries are found such that the maximum Power Transfer Efficiency (PTE) is achieved.

2   WIRELESS POWER TRANSFER USING PRINTED SPIRAL COIL (PSC)

In Chapter 2, the detail of the design of a Printed Spiral Coil (PSC) is discussed. The calculation of different coils geometries and the design of circuit model of WPT using inductive coupling for implantable biomedical devices are explained in order to calculate the PTE. This work has been published in [90].

2.1   Coil Design

PSCs are viable candidates for inductive near-field wireless power transmission to the upcoming generation of implanted devices with size constraints. It has the ability to conform to the body curvature with thin flexible substrates.

The electrical model of spiral inductors printed on the circuit board is shown in Fig. 2.1. It consists of the inductor in series with a resistor. The combination of inductor and resistor is in parallel with a capacitor.
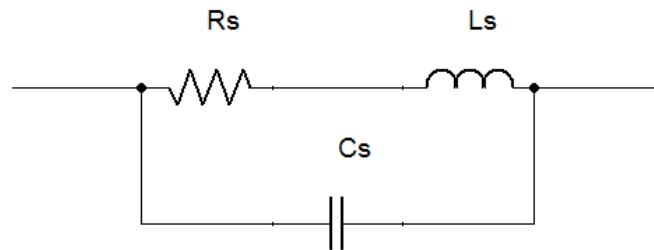
Fig. 2.1. The electrical model of the planar spiral inductor.

In this work, all PSCs are spiral circular shaped with the layout shown in Fig. 2.2. For a given shape, an inductor is specified completely by the outer diameter (d_o), inner diameter (d_i), turn width or trace (w), turn spacing (s) and a number of turns (n).
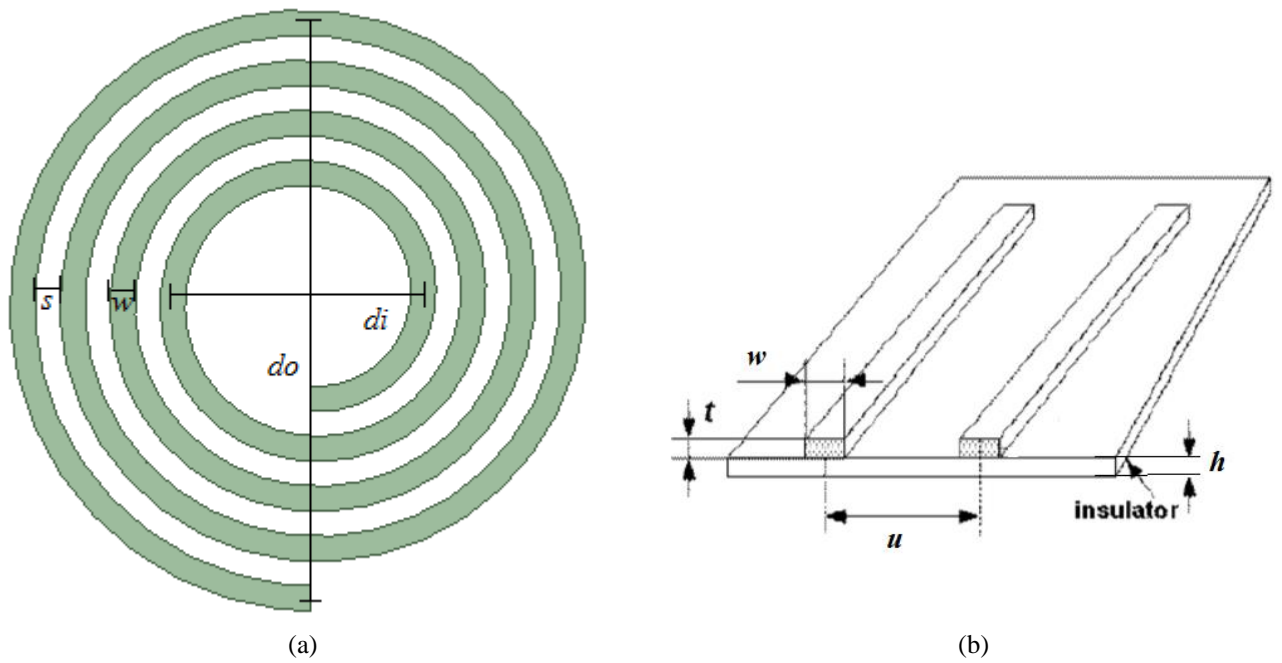
Fig. 2.2. Geometric parameters of spiral coil. (a) Top view of on-board spiral inductor. (b) A pair of parallel conductor 3D view [91].

2.2 Inductive and Radiative WPT Comparison

In this study, two methods of WPT for implanted biomedical devices are compared: inductive and radiative methods. The inductive system that we designed was compared with a radiative method designed by Dr. Sajal from Minot State University.

For both methods, the transmitter is placed directly on the skin. The receiver is embedded in the muscle in various depths, from 10 mm to 110 mm, with increments of 10 mm. The real part of the input and output powers (P_{in}, P_{out}) were used to calculate the AC-AC efficiency at each distance according to below equation:

$$\eta_P = \text{Re}(Pout)/\text{Re}(Pin) \tag{2.1}$$

25

Three layers of tissues model consisting of skin (3 mm thick), fat (7 mm thick) and muscle (100 mm thick) were considered. Frequency of 13.56 MHz was used for inductive method while 2.45 GHz was considered for the radiative setups. The electromagnetic properties at each frequency were obtained from Institute of Applied Physics (IFAC) [92] and summarized in Table 2.1.

Table 2.1. Electromagnetic properties at 13.56 MHz.

Parameter	Dry Skin	Fat	Muscle (Transverse)
Thickness (mm)	3	7	100
Mass density (kg/m^3)	1100	910	1041
Relative Permittivity ε @ 13.56MHz	285.250	11.827	138.440
Relative Permittivity ε @ 2.45GHz	38.007	5.2801	52.729
Conductivity σ [S/m] @ 13.56MHz	0.238	0.030	0.628
Conductivity σ [S/m] @ 2.45GHz	1.464	0.104	1.738
Loss Tangent @ 13.56MHz	1.106	3.402	6.015
Loss Tangent @ 2.45GHz	0.282	0.145	0.242

2.2.1 Inductive Power Transmission

There are two possible ways to perform the simplest optimization for inductive transmitter coil geometry: the first one assumes the transfer distance is known (r is fixed and constant). It is suitable for medical applications where the device is implanted in a certain location inside the tissues. Based on that, the optimum transmitter coil radius (a) is calculated as follows:

$$a = \sqrt{2}\, r \tag{2.2}$$

This equation is derived by calculating the maximum H that could be generated by the transmitter coil [6].

The second optimization method is presented for those applications having portable receivers or a changeable transfer distance with a predicted range, such as the case where the receiver is located at different distances from the transmitter. Transmitter coil radius is optimized by calculating $\vec{H}$ in the whole transfer range (x) [6]:

$$\int_{x1}^{x2} \vec{H}.d\vec{x} = \int_{x1}^{x2} \frac{I\,N\,a^2}{2\,\sqrt{a^2 + x^2}}dx \tag{2.3}$$

where I is current in Amperes, N is the number of coil turns, x_1 is the beginning of the range and x_2 is the end of the range. In order to find the optimized shape of the transmitter, we modeled (2.3) on MATLAB (Mathworks, Natik, MA) to determine the optimum coil radius for a range of distances vary from (10 mm–110mm). Fig. 2.3 shows the results. The optimized transmitter radius for the transfer range is found as 19 mm.
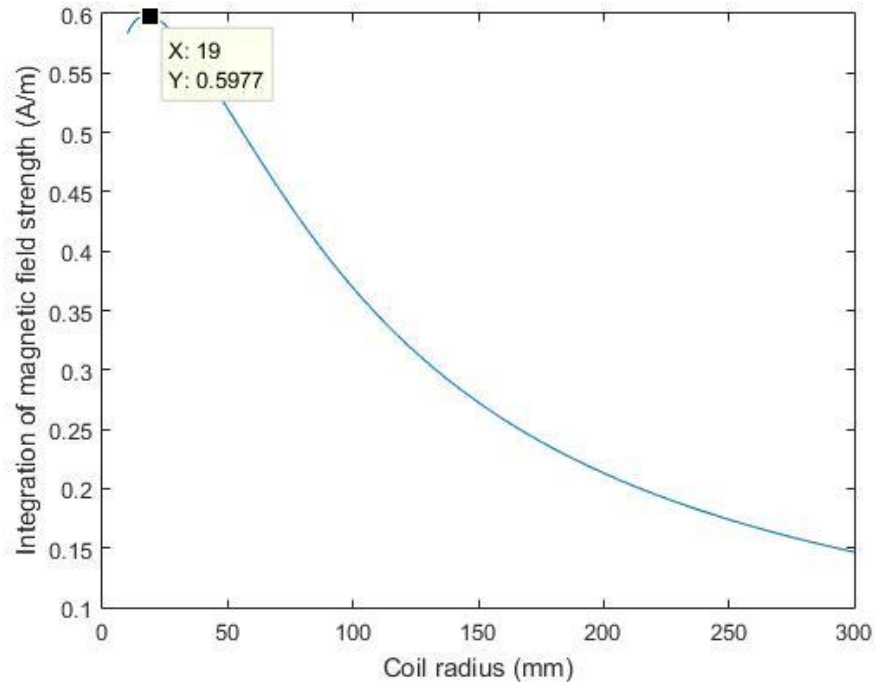
Fig. 2.3. Magnetic field integration for specified transfer range.

The remaining dimensions are taken from [63]. The specifications of the coils are summarized in Table 2.2.

Table 2.2. Dimensions of the coils for the inductive link.

Parameter	Symbol	Transmitter	Receiver
Outer diameter	d_o (mm)	38	10
Inner diameter	di (mm)	13.5	5.0
Conductor trace	w (μm)	1500	250
Conductor space	s (μm)	250	250
Number of turns	n	7	5
Conductor thickness	t (μm)	18	18
Substrate dielectric constant(Roger RT/duroid 6002 material) [93]	ε_r	2.94	2.94
Substrate thickness	h (mm)	1.750	0.508
Transfer distance	r (mm)	[10–110]	

The simulated inductive link model is shown in Fig. 2.4.

(a)   (b)
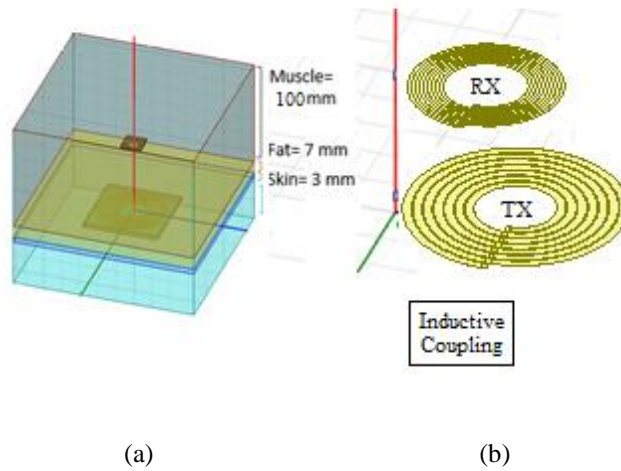
Fig. 2.4. A simplified circuit for (a) coils modeled in the layered tissue model, and (b) in the air

2.2.2 Radiative Power Transmission

This design consists of two patch antennas resonating at 2.45 GHz as shown in .

The TX antenna was placed close to the skin in the air and the receiver antenna was placed

in the muscle layer. Both antennas were simulated on Rogers TMM4 substrate, with relative permittivity, $(\varepsilon_r = 4.5)$ and loss tangent $(\tan \delta = 0.002)$. The thickness of 1.52 mm was considered. Copper was used as a conductor. Antennas have a reflection coefficient of -11.69 dB at 2.45 GHz and a gain of 5.93 dBi. The radiative link model is shown in Fig. 2.6.

(a)   (b)
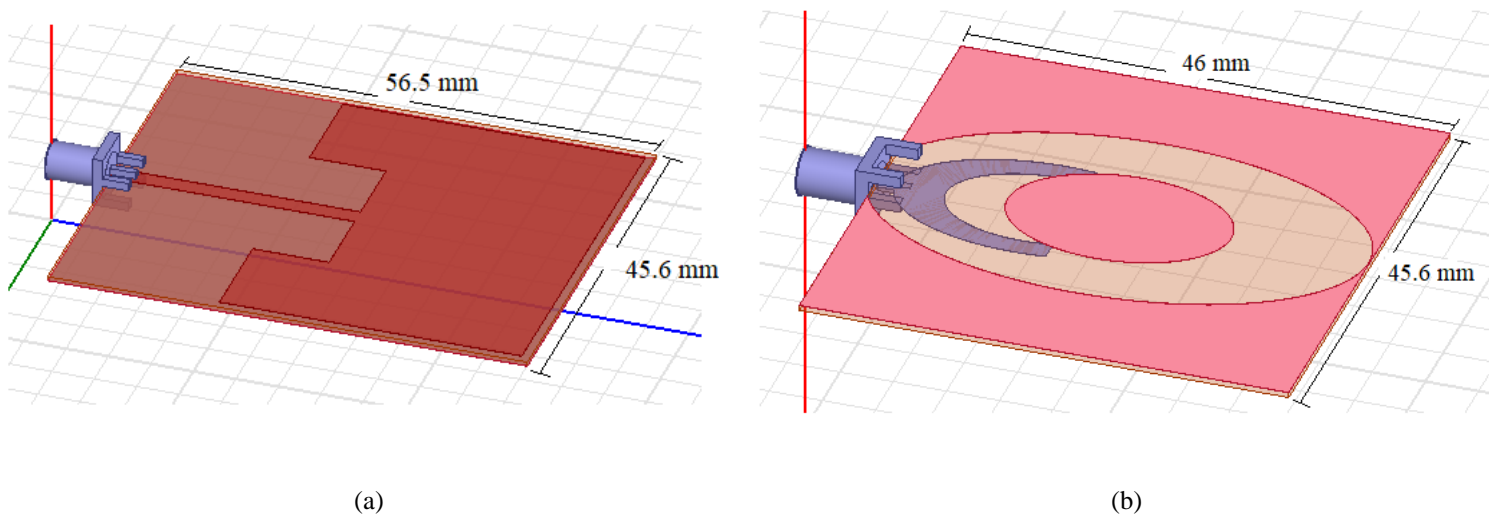
Fig. 2.5. Antenna design for radiative link (a) TX, and (b) RX.

(a)   (b)
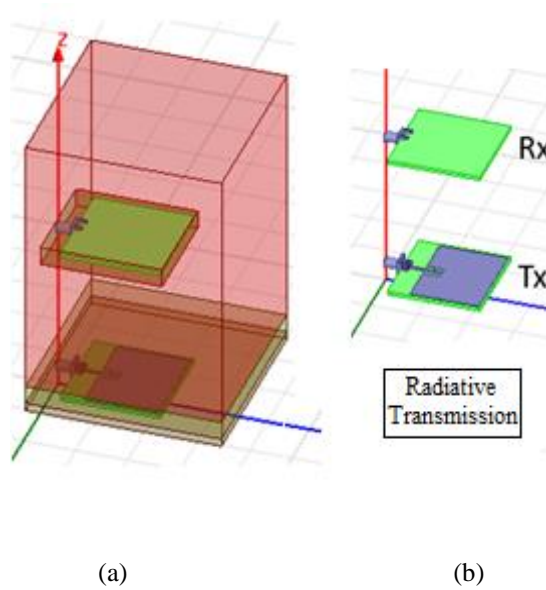
Fig. 2.6. A simplified circuit for (a) radiative transmission in layered tissue model, and (b) in the air.

2.3 Circuit Model and Efficiency

The simplified diagram of the inductive WPT circuit is shown in Fig. 2.7 [61]. L_1 is the primary transmitter coil that is located outside the body, and L_2 is the secondary receiver coil that is implanted in the body, often with the rest of the implant electronics. Coil windings have parasitic capacitance and resistance associated with them, which are shown as elements (R_{s1}, R_{s2}), and (C_{s1}, C_{s2}). Capacitors C_T and C_R are added to the circuit to form a pair of resonance LC-tank circuits with L_1 and L_2, respectively. R_L is the load resistance, its value is 500 Ω for inductive link and 50 Ω for radiative link.
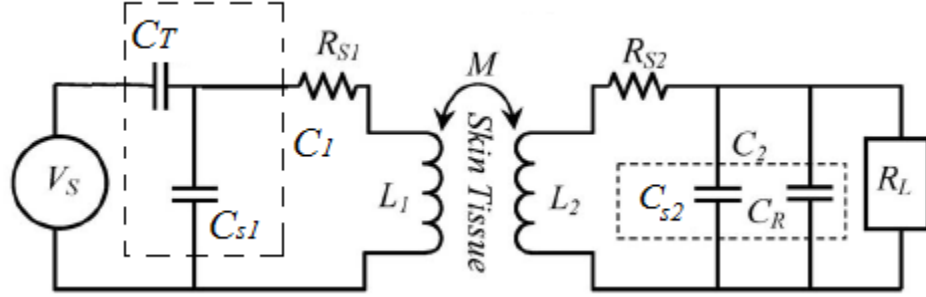
Fig. 2.7. Circuit model of inductive coupling.

The highest voltage gain and efficiency is achieved when both LC tanks are tuned at the operating frequency of the link $\omega_o = 1/\sqrt{L_1 C_1} = 1/\sqrt{L_2 C_2}$, where C_1 and C_2 are a combination of the lumped capacitor and the parasitic capacitance of the primary and secondary coils respectively.

The delivered power to the primary LC tank divides between the R_{s1} which is wasted as heat, and the secondary loading which is reflected into the secondary through mutual inductance (M). M is related to the coupling coefficient (k) according to:

$$k = \frac{M}{\sqrt{L_1 L_2}} \tag{2.4}$$

The quality factors for the transmitter (Q_1), receiver (Q_2) and load (Q_L) circuit are calculated as follows:

$$Q_1 = \frac{\omega_o L_1}{R_{s1}}, \qquad Q_2 = \frac{\omega_o L_2}{R_{s2}}, \qquad Q_L = \frac{R_L}{\omega_o L_2} \tag{2.5}$$

The total efficiency, η_P, is calculated according to (2.6):

$$\eta_P = \frac{k^2 Q_1 Q_2}{1 + k^2 Q_1 Q_2 + \frac{Q_2}{Q_L}} \times \frac{1}{1 + \frac{Q_L}{Q_2}} \tag{2.6}$$

31

Simulation models for both methods were developed and the comparison was made in terms of PTE at different spacing between the transmitter and receiver.

2.4 Simulation Results

Simulations for inductive link have been done using ANSYS Maxwell (Ansoft, Pittsburgh, PA [94]) to calculate the value of L_1, L_2, R_{s1}, R_{s2}, C_{s1}, C_{s2}, and k. Then the simulated design was imported to ANSYS Simplorer to calculate the efficiency. Similarly, ANSYS HFSS was used to simulate the radiative system, and the equivalent circuit was exported from HFSS to ANSYS Simplorer to calculate the PTE.

In both cases, simulations were run by changing the spacing between the transmitter and receiver from 10 mm to 110 mm with a 10 mm increments. Simulation results for both methods are shown in Fig. 2.8. One simulation was performed at exactly 26 mm spacing.
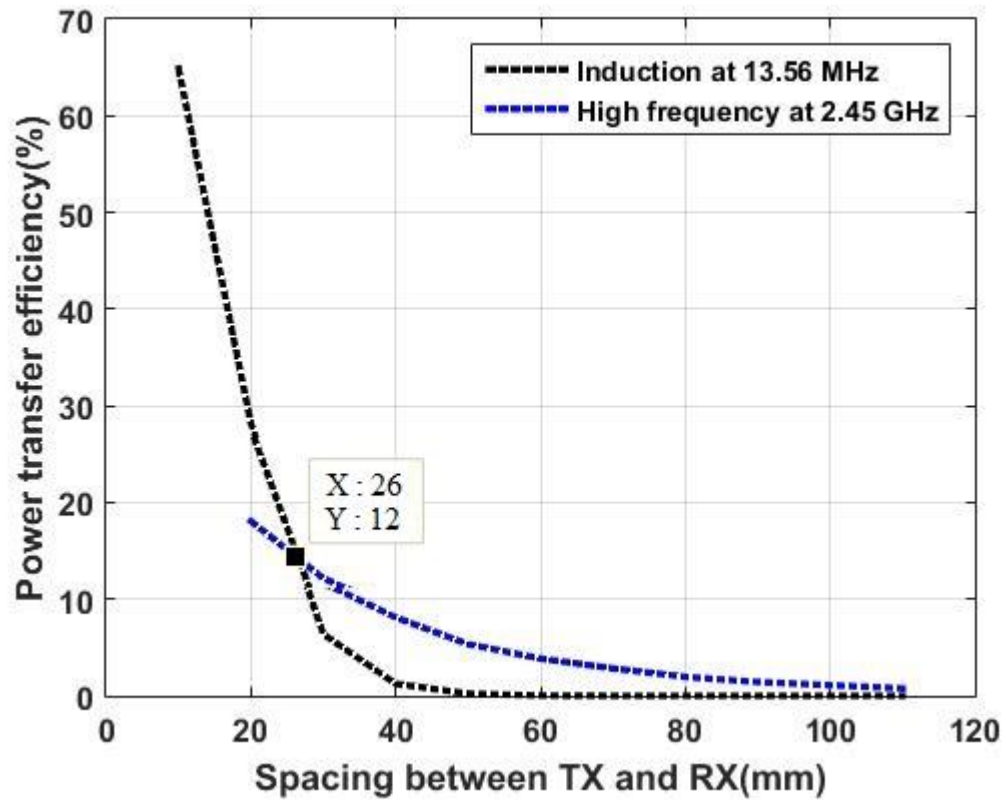
Fig. 2.8. Power transfer efficiency comparison.

It is concluded that the inductive coupling performs better than the radiative transmission at small spacing between the transmitter and receiver coils (12% efficiency is achieved for both methods at the 26 mm distance). As spacing is increased the inductive method becomes inefficient and the radiative transmission has more efficiency. Therefore, it is recommended to use radiative method for deep in-body power transfer.

3 HYBRID COIL AND ANTENNA SYSTEM FOR BIOMEDICAL IMPLANTED DEVICES

Recently, WPT technologies have been widely adopted as a power source for implanted and wearable biomedical devices, since they provide convenience and portability. While the use of WPT is a nice addition to health-monitoring systems that have greatly affected the human healthcare [95]-[96], they should be carefully designed and studied to make sure the reliability of their performance. The communication link and WPT may require large size antennas and coils for the two systems. The system includes two parts: the external combination (EX) and the implanted (IM) combination. An example of such systems is a glucose monitoring system. The IM is a sensor that through the wireless communication channels sends the sensor signals of glucose level and blood pressure to EX equipment. These types of sensors fall under health-monitoring systems that are being developed for multiple purposes such as monitoring patients, fire-fighters, astronauts, and soldiers.

WPT and wireless communication need bulky transmitters and receivers. Therefore, our major challenge is miniaturizing the communication and WPT systems. The unification and combining WPT and communication antennas provides the means of miniaturization of the overall system.

In proposing such system we consider: (1) a method that system can be adopted for multiple frequencies, and (2) combining the WPT and communication links in a hybrid system to minimize the form-factor. Multi-band is used to control multiple IM devices simultaneously. Also, each frequency band might be used for a different wireless link sending data, images, or control signals. The major limiting factors in these devices are the

size of antennas and coils. Many techniques and methods have been proposed and used to minimize the size of microstrip antennas at a certain frequency. One common method to reduce antenna size is the use of high permittivity substrate [97]. However, this method has a negative influence on impedance bandwidth. Other methods have been used such as slot loading of the patch, e.g. U-shaped or H-shaped slots on the patch, to enhance the effective electrical length of the current path and to minimize the antenna size [98], [99]. In [100], authors applied a shorting pin technique to design a compact microstrip antenna working in free-space.

In this research, we propose a compact hybrid design consisting of a pair of optimized inductive coils to transfer power wirelessly, and a novel antenna in a G-shaped design for data communication. Shorting pin is used to reduce the antenna size, whereas the location of the shorting pin inside the antenna is adjusted to determine its resonance frequency (f_{oEX} and f_{oIM}, for EX and IM, respectively). The coil size was optimized for the best efficiency and size.

3.1   System Model

For this design we consider that the EX antenna/coil combination is placed directly at the outer surface of the skin, and the IM antenna/coil combination is embedded inside the muscle tissue. It is assumed that a layer of fat and a layer of skin are coving the muscle layer. We started the design by assuming that IM combination is at located at h=15 mm from the EX combination. A layered body model consisting of three tissue layers is shown in Fig. 3.1Fig. 3.1. Layer model and drawings of the hybrid design of the EX and IM antenna/coil combinations.: the skin layer (3 mm), the fat layer (7 mm), and the muscle layer (125 mm). All three layers have 212 mm $\times$ 212 mm surface area. IM and EX are assumed to be covered

35

by a layer of silicone with a thickness of 100 μm. The details of EX and IM dimensions are presented in Sections 3.2 and 3.3.
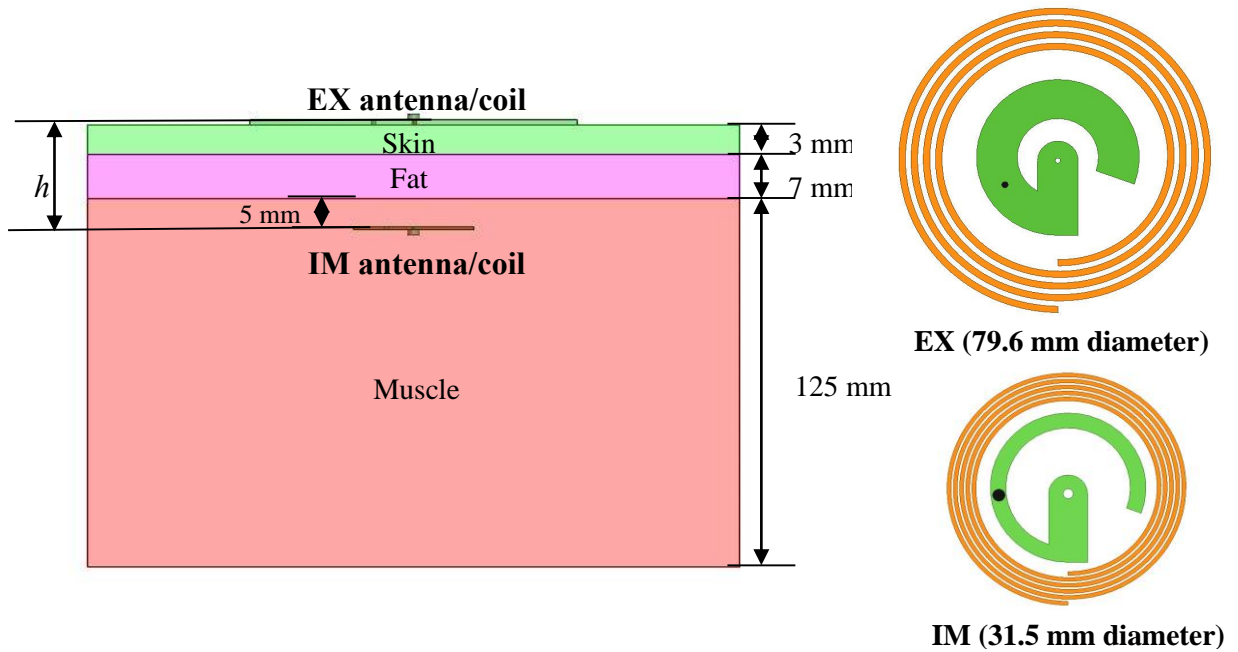
Fig. 3.1. Layer model and drawings of the hybrid design of the EX and IM antenna/coil combinations.

The electromagnetic properties of each layer at each frequency were obtained from the Institute of Applied Physics (IFAC) database [92] and are summarized in Table 3.1. The permittivity of the tissue layers affects the antenna's performanc. However, it has very small effects on the inductive coupling.

EX and IM combinations are integrated on FR4 substrate ($\varepsilon_r = 4.4$ and $\tan\delta = 0.02$) is considered. The substrate thickness for EX is 1.52 mm, while for IM thickness is assumed to be 0.8 mm. The copper thickness is assumed to be 35.56 μm.

Table 3.1. Tissue electromagnetic properties at different frequencies

f (MHz)	Tissue	ε_r	σ	$\tan\delta$
13.56	Muscle	138.44	0.63	6.01
	Fat	11.83	0.03	3.4
	Skin	285.25	0.24	1.10
415	Muscle	57.00	0.80	0.61
	Fat	5.57	0.04	0.32
	Skin	46.50	0.69	0.65
905	Muscle	55.00	0.94	0.34
	Fat	5.46	0.05	0.18
	Skin	41.40	0.87	0.42
1300	Muscle	54.20	1.09	0.28
	Fat	5.40	0.06	0.15
	Skin	39.90	1.00	0.34

3.2 Antennas Design

The EX and IM microstrip antennas have a G-shape profile. This design provides simplicity and low fabrication cost. The patch antenna is fed by a probe. The antenna geometry is shown in Fig. 3.2 where R_{out} is the outer radius, R_{in} is the inner radius, R_e is the middle edge radius, g is the distance between the center of the antenna circle and the feeding probe, R_g is the ground circular slot radius, D_s is diameter of the shorting pin, D_f is the diameter of the feeding probe, and Φ is the arc angle.

The designed parameters values for EX and IM antennas are presented in

Table 3.2. The antennas were simulated using ANSYS HFSS software [94].
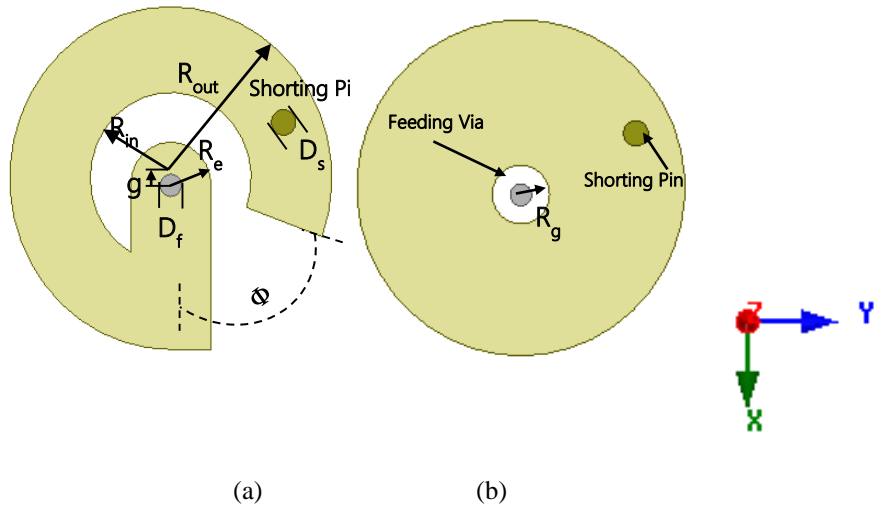
Fig. 3.2. Antenna geometry of (a) top radiating patch layer, and (b) ground plane.

Table 3.2. Parameters of antennas geometries.

Parameter	EX antenna	IM antenna
R_{out} (mm)	20	10
R_{in} (mm)	10	8
R_e (mm)	5	2.5
g (mm)	0.8	0.8
R_g (mm)	2	2
D_s (mm)	1.6	1.6
D_f (mm)	1.3	1.3
Φ (degree)	70	70

Shorting pin is used to reduce the antenna size. This process produces the same frequency response at half the size of a similar antenna without using the shorting pin.

The position of shorting pin location affects the resonance frequency (f_o) of the microstrip patch antenna. In free-space [101], the resonance frequency, f_o, can be obtained from equation (3.1).

38

$$f_o = \frac{c}{2(R_{out} + R_{in})\phi_{radians}\sqrt{\varepsilon_{eff}}}$$

(3.1)

where c is the speed of light in vacuum and ε_{eff} is the effective dielectric constant.

We used optimization frequency domain solver in HFSS to find the best location of the shorting pin in order to achieve the antenna resonance frequencies at three UHF frequencies (415 MHz, 905 MHz, and 1300MHz). the pin positions are shown in Table 3.3. These antenna designs do not require any matching circuit, since the antenna is matched to 50 Ω at all three frequencies.

Table 3.3. Shorting pin locations for EX and IM antennas assuming antenna center at (0,0).

Antenna	f_o [MHz]	415	905	1300
EX	x (mm)	-6.50	6.75	11.00
	y (mm)	14.00	-13.00	-5.50
IM	x (mm)	2.25	1.08	6.72
	y (mm)	8.70	-8.80	-5.95

3.3 Coil Design

Coil geometry and design are shown in Fig. 3.3 is the most important part of the physical implementation of WPT system to maximize efficiency and power transfer. The main difficulty of this design is to minimize the coupling effect between the antenna and the coil. Therefore, via Ansys Maxwell simulation, the optimum dimensions to keep the system compact while reducing the coupling effects should be found at first.

The rest of coil geometries parameters of coil trace (w), coil space (s), and the number of turns (n) have been optimized using the parametric optimization tool in Ansys Maxwell [94]. The values have been selected based on the maximum coupling coefficient (k) that

39

could be achieved between the EX and IM coils taking into consideration the maximum outer diameter (d_{out}) that we need to design the coils for.
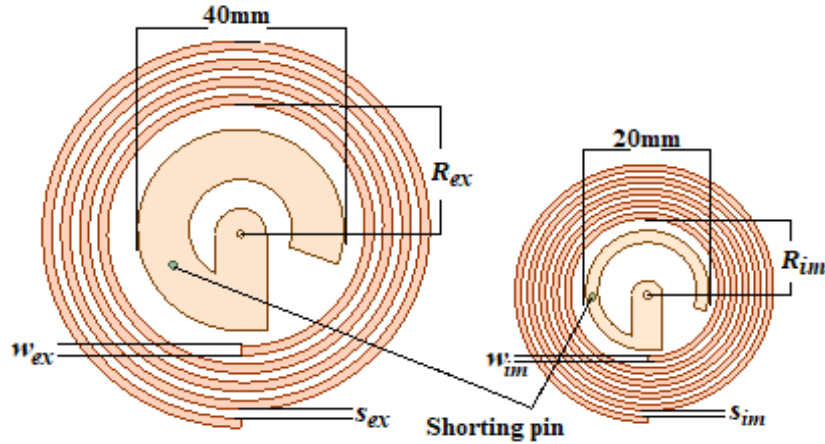
Fig. 3.3. Coil and antenna design for (a) EX coil: w_{ex}=1.6 *mm*, s_{ex}=1.4 *mm* and R_{ex} [21to 30] *mm*, and (b) IM coil: w_{im}=500 *μm*, s_{im}=300 μm and R_{im} [10.5 to 14] *mm*.

Initially the antennas were designed and simulated in the absence of the coils. The minimum reflection coefficients for the EX and IM antennas, S_{11} and S_{22}, respectively were achieved at 905 MHz, with -10 dB reflection coefficient bandwidth of 827 MHz – 1 GHz. In order to place the coil at a proper distance away from the antenna to minimize the interaction and coupling effects between the coil and the antenna, the value of the inner radius for EX and IM coils, R_{ex} and R_{im}, respectively, were optimized using the parametric tool solver in ANSYS HFSS. First, the values of w_{ex} and s_{ex} were set then the value of R_{ex} was swept, starting from 21 mm, which is 1mm more than the radius of EX antenna, with the increments of 1 mm, up to a maximum of 30 mm. The effects of the addition of coil on S_{11} and S_{22} were studied. Then the optimum value for R_{ex} was selected. Secondly, the same process was done for the IM coil by sweeping R_{im} from 10.5 mm to 14 mm, with 0.5 mm increments and the optimum value of R_{im} was selected though.

Fig. 3.4 shows S_{11} and S_{21} versus frequency at different values of R_{ex}, marked by different colors. The maximum coupling effects occur at R_{ex} = 21 mm where f_{oEX} was shifted to 970 MHz. This was expected since it is the closest distance between the EX coil and the antenna. The f_{oEX} of 905 MHz was achieved at R_{ex} = 27 mm. S_{21} achieved its maximum value at f_{oEX} = 905 MHz.
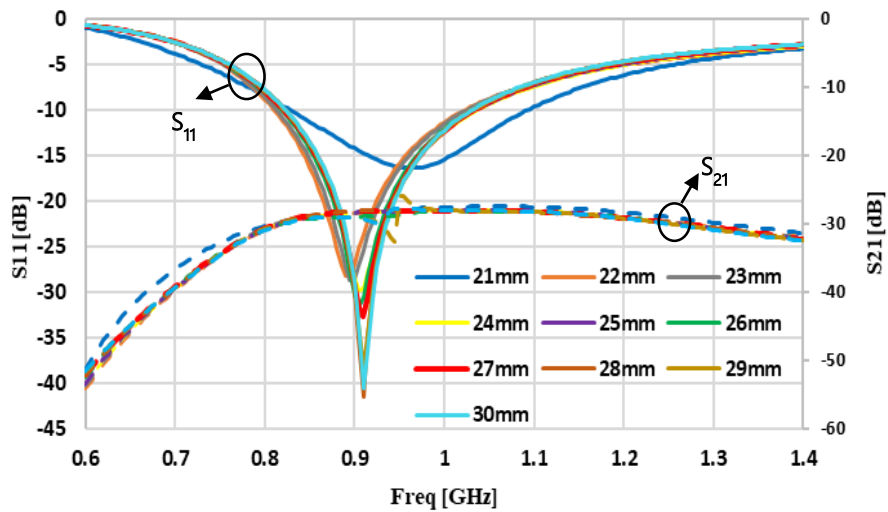
Fig. 3.4. S_{11} and S_{21} for EX antenna at different coil radii(R_{ex}) vs frequency.

Fig. 3.5 shows S_{22} and S_{21} versus frequency, at different values of R_{im}. As expected the worst set-up of coupling case occurred at the closest distance between IM coil and antenna at 10.5 mm. Other values of R_{im} gave better results due to minimization of coupling effects when the separation of antenna and coil is increased. The best result was achieved at 11.5 mm and S_{21} achieved its maximum value at (f_{oIM} = 905 MHz).
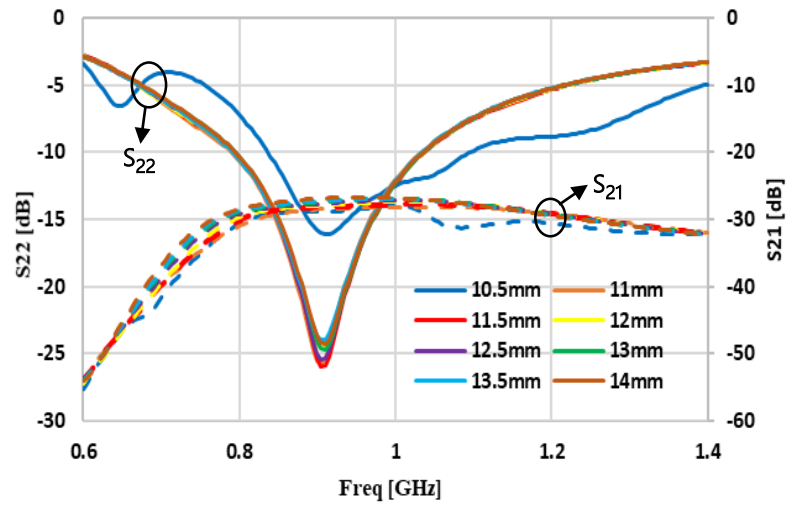
Fig. 3.5. S_{22} and S_{21} for the IM antenna at different coil radius (R_{im}) vs frequency.

The EX and IM coil geometries are summarized in Fig. 3.6 and

Table 3.4 and our research work is published in [102]. The coils were designed to transfer

power at f_{coil} = 13.56 MHz.
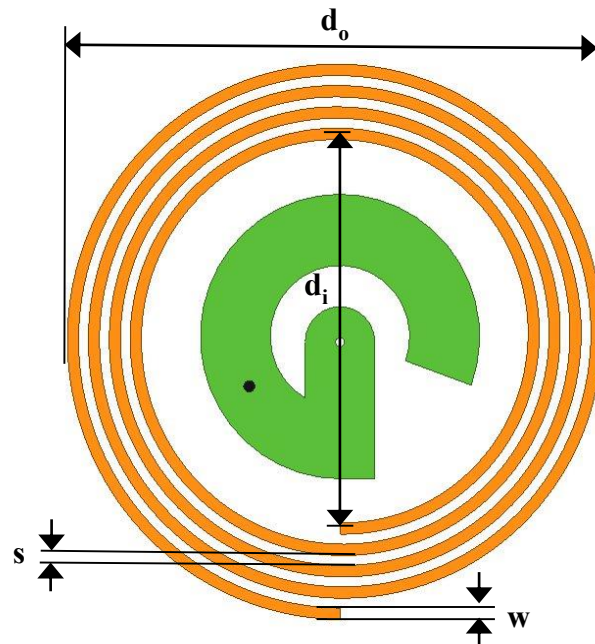
Fig. 3.6. Geometrical parameters of a circular planar spiral coil.

Table 3.4. Parameters of coil geometries.

Parameter	EX coil	IM coil
d_o (mm)	79.6	31.5
d_i (mm)	54	23
s (µm)	1400	300
w (µm)	1600	500
n	4	5

3.4   Circuit Model

The simplified circuit diagram of the power flow through coils inductive link, as well as the lumped capacitors elements, added for matching, are shown in Fig. 3.7. L_{EX}, R_{EX}, C_{EX} represent the inductance, resistance and the matching capacitance of the EX coil, respectively. L_{IM}, R_{IM}, C_{IM} represent the inductance, resistance and the matching capacitance of the IM coil, respectively. R_s is the source resistance, R_L is the load resistance, and k is the coupling coefficient between the EX and IM coils. The value of C_{EX} and C_{IM} are chosen to satisfy equation (3.2).

$$f_{coil} = \frac{1}{2\pi\sqrt{L_{EX}C_{EX}}} = \frac{1}{2\pi\sqrt{L_{IM}C_{IM}}} \tag{3.2}$$
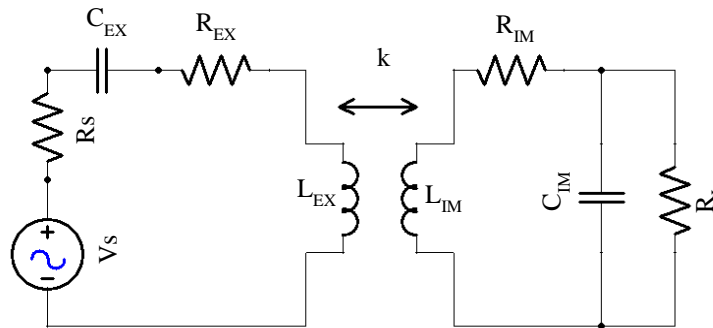
Fig. 3.7. A simplified circuit diagram for the inductive link with matching capacitors.

This circuit was simulated by ANSYS Simplorer.

Table 3.5 summarizes the evaluated values given by the simulation.

Table 3.5. Circuit element parameters for the inductive link**.**

Parameter	EX coil	IM coil
L (μH)	1.783	1.204
R (mΩ)	357.27	567.31
C (pF)	77.26	114.42
R_L (Ω)	50	
R_S (Ω)	50	

3.5   Power and Data Transmission Efficiency

To study the performance of the system we studied the influence of the implanting depth on the stability of resonance frequencies of antennas, f_{oEX} and $f_{oIM,}$ at each resonance frequency of interest (415 MHz, 905MHz, and 1300 MHz). Furthermore, the transmission efficiency (η) at different distances was calculated for coil/antenna combination through equation (3.3).

$$\eta = \left|S_{21}\right|^2 \times 100\% \qquad (3.3)$$

where S_{21} is the transmission coefficient. For the antenna pair, ANSYS HFSS simulation program was used to extract S_{21} directly. Whereas for the coil this value was extracted by importing the coil design into ANYS Maxwell and integrating it with the circuit shown in Fig. 3.7, in ANSYS Simplorer.

The achieved simulated values of f_{oEX} and f_{oIM} at different h between the EX and IM combinations in the range of 15 mm to 110 mm are summarized in Table 3.6. It is notable that the resonance frequency of the antenna for each one of the three designs does not change more than 20 MHz while the implant depth (h) is changed. We conclude that the three proposed G-shape antennas are not affected by the implanting depth and the distance between the EX and IM antennas.

Table 3.6. Resonance frequencies of antennas at different implanting depth.

h (mm)	415 MHz		905 MHz		1300 MHz	
	f_{oEX}	f_{oIM}	f_{oEX}	f_{oEX}	f_{oIM}	f_{oEX}
15	415	415	905	905	1300	1300
20	415	410	910	900	1295	1290
30	415	410	905	905	1300	1300
40	415	410	905	905	1300	1300
50	415	410	905	910	1300	1300
60	415	410	905	905	1300	1300
70	415	410	905	905	1300	1300
80	415	410	905	905	1300	1300
90	415	410	905	905	1300	1300
100	415	410	905	905	1300	1300
110	415	410	905	905	1295	1300

We studied the simulated performance of the antennas at all bands at h=15 mm. The minimum reflection coefficients for the EX and IM antennas, S_{11} and S_{22} with -10 dB bandwidth that are achieved by simulation are summarized in

Table 3.7. The simulated S_{21} with frequency at the same h is drawn in Fig. 3.8. Please note that the maximum value of S_{21} occurs at the 905 MHz and 1300 MHz, whereas at 415 MHz has lower transfer coefficient and efficiency. Radiation patterns are shown in Fig. 3.9 and Fig. 3.10.

Table 3.7. Antennas' performance.

Description	415 MHz	905 MHz	1300 MHz
S_{11} (dB)	-13.81	-45.25	-15.23
-10 dB EX	0.38-0.456	0.82-1.028	1.192-1.45
S_{22} (dB)	-15.88	-24.99	-37.94
-10 dB IM	0.361-0.485	0.79-1.036	1.157-1.472
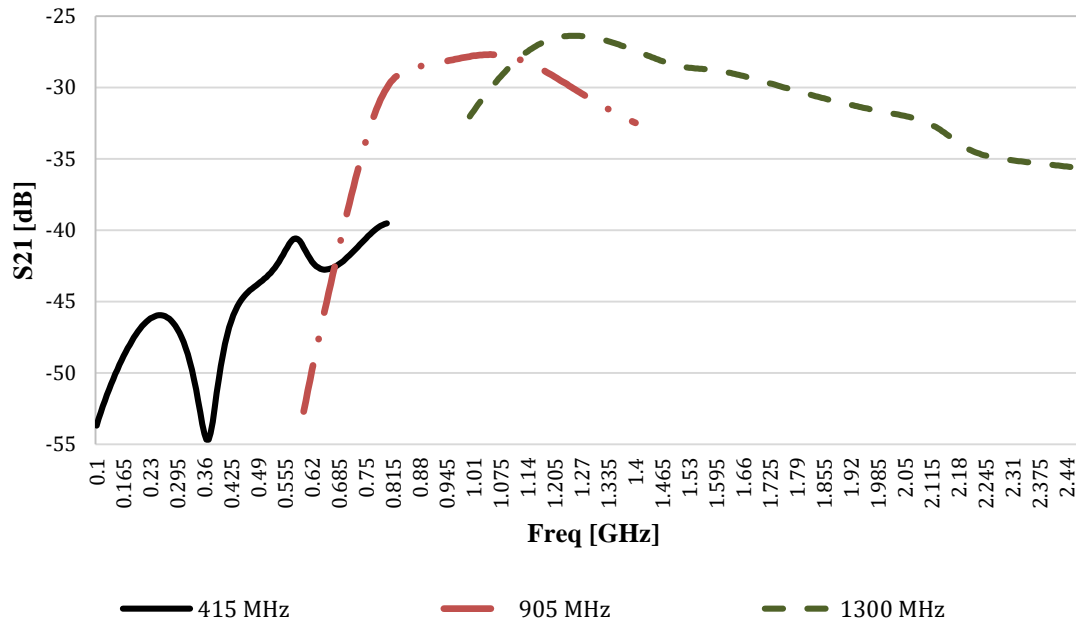
Fig. 3.8. S_{21} vs frequency for all antenna design case.
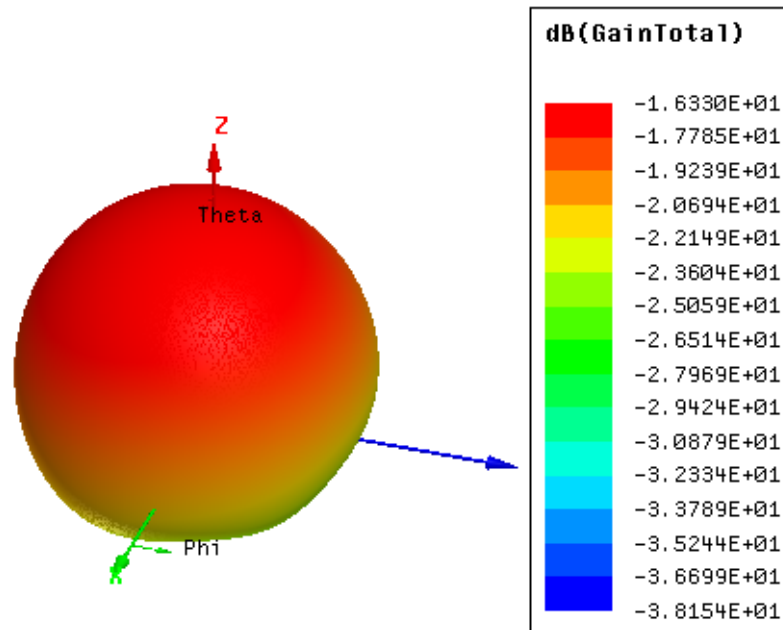
Fig. 3.9. 3D radiation pattern at 905MHz.
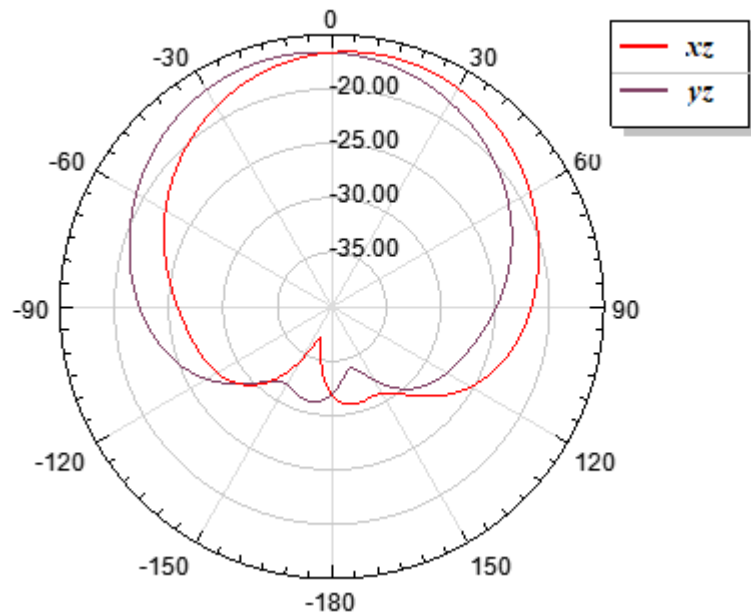
Fig. 3.10. *xz* and *yz* radiation pattern at 905MHz.

We also studied the behavior of S_{21} and η of EX and IM combinations while varying the *h* depth. Results are plotted in Fig. 3.11 and Fig. 3.12. We noticed that the behavior of antennas at 905 MHz and 1300 MHz is approximately the same. As a comparison between η for coil inductive link and the antennas, we noticed that the inductive link has much higher η than the data link. As the distance between EX and IM increases η of both bands is approximately the same after 60 mm.
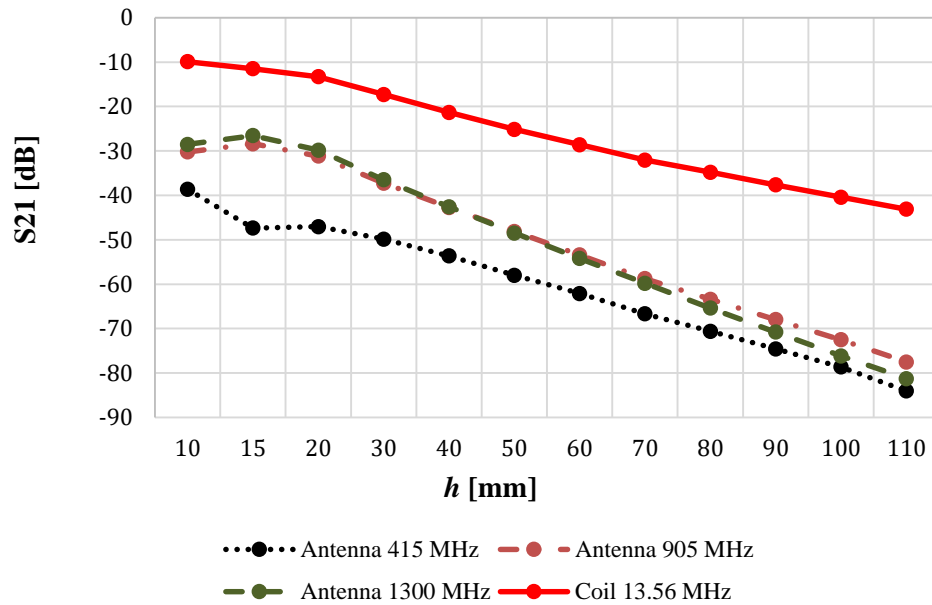
Fig. 3.11. S_{21} versus *h* implant depth.
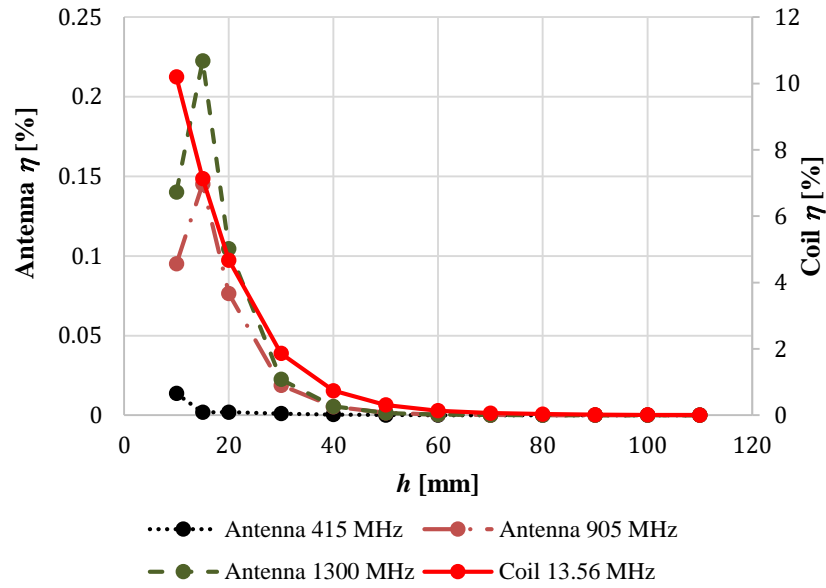
Fig. 3.12. η versus h implant depth. .

3.6   Chapter Summary

In this Chapter, we proposed and investigated the performance of a hybrid system that combines the antennas for communication and coils for WPT. The antennas can be adjusted to work at one of the three different frequencies (415 MHz, 905 MHz, and 1300 MHz). The coils transfer power at 13.56 MHz. We investigated the performance through simulation and measurements of efficiency (η) and transmission coefficient (S_{21}) at different implanting depths.

The system provides a good solution for the combination of WPT and data communication in a compact design.

4 MISALIGNMENT EFFECTS ON HYBRID POWER TRANSFER AND WIRELESS ANTENNA SYSTEM

WPT technique based on the inductive links is one of the promising solutions for powering biomedical implanted devices. Ensuring a stable power transfer and data communication in implanted devices, under conditions such as misalignment is challenging. Misalignment may happen due to changing the biological environment or body movement. An immediate effect on coil and antenna misalignment is changing the coupling factor between EX and IM [103]. Two forms of misalignments (lateral and angular) are being discussed in Sections 4.2.1 and 4.2.2 in this chapter.

In [104], lateral and angular misalignments have been studied for spiral coils to increase the power transfer and system efficiency. However, that system was not designed for data communication. In [80], authors presented an inductive link to transfer power and data, but this system was tested only for lateral misalignment.

In Chapter 3, it was the hybrid system that consists of an EX and IM coils were presented. The effects of lateral and angular misalignments between EX and IM combinations on coupling (k), transmission coefficient (S_{21}), and efficiency (η) are discussed in this chapter as well as the effect of rotating the IM combination around the x-axis.

4.1 Coil and Antenna Design Structure

The proposed system consists of a hybrid EX and IM combinations that consist of a pair of antennas to send/receive data at 905 MHz as discussed in Section 3.2, and a coil design that transfer power at 13.56 MHz and explained in Section 3.3. The EX combination

is placed directly at the outer surface of the skin, and the IM that is embedded in muscle. Electromagnetic properties of each body tissue in the layered body model are the same as those given in Section 3.1.

4.2 Misalignment Types

The simulations were performed observe the changes in k, S_{21}, and η resulting from the following two types of misalignments.

4.2.1 Lateral Misalignment

In lateral misalignment, both the EX and IM are located in parallel planes and separated by a certain depth, while the lateral distance between their centers is d. The distance d was changed from -60 mm to 60 mm, in steps of 10 mm in direction of y-axis. The distance between EX and IM systems was fixed at 15 mm (case 1), and 30 mm (case 2), as shown in   Fig. 4.1.
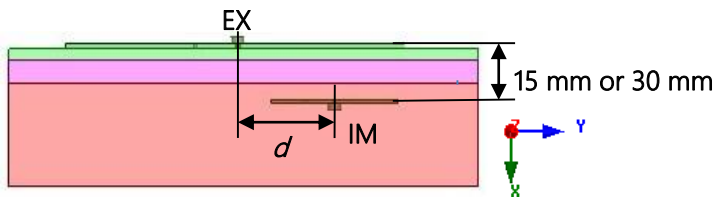
Fig. 4.1. Lateral misalignment between the EX and IM combinations.

4.2.2 Angular Misalignment

In angular misalignment, the plane of IM is tilted by an inclined angle θ, while keeping the EX plane unchanged. Angle θ was changed from -90º to 90º, in steps of 10º , rotating around z-axis. The distance between the centers of EX and IM was kept at 30 mm as shown in Fig. 4.2.

51
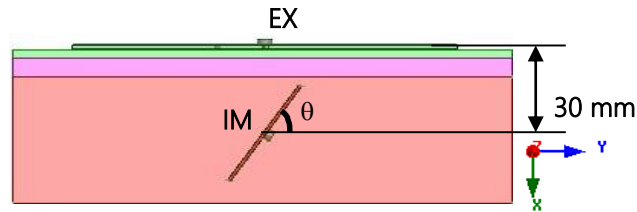
Fig. 4.2. Angular misalignment between the EX and IM combinations.

4.2.3 Rotating IM Combination

The effect of rotating IM combination around x-axis while keeping the EX plane unchanged is also studied. Rotating angle (Φ) was changed from 0° to 180°, in steps of 15°. The distance between the centers of EX and IM was kept at 30 mm.

Fig. 4.3. Rotating angle of IM combinations.

4.3 Circuit Design and Used Simulation

The circuit design discussed in section 0 was used. ANSYS HFSS was used to simulate the antennas at 905 MHz, whereas ANSYS Maxwell was used to simulate the coils at 13.56 MHz. The simulated design was imported to ANSYS Simplorer in order to calculate S_{21} and η.

4.4   Simulation Results

Fig. 4.4 shows S_{21} and η vs. d for both antenna and coil pairs, while EX and IM are separated by 15 mm. It can be noted that the lateral misalignment has a small effect on the values of S_{21} and η for coil in the range of d = [-20 mm to 20 mm]. They reach their maximum of S_{21} = -11.44 dB and η = 7.2% at d = 0, then these values drop rapidly after d increases to more than 30 mm. Similarly, the value of S_{21} for the antenna is maximum at d = 0 (S_{21} = -28.64 dB).
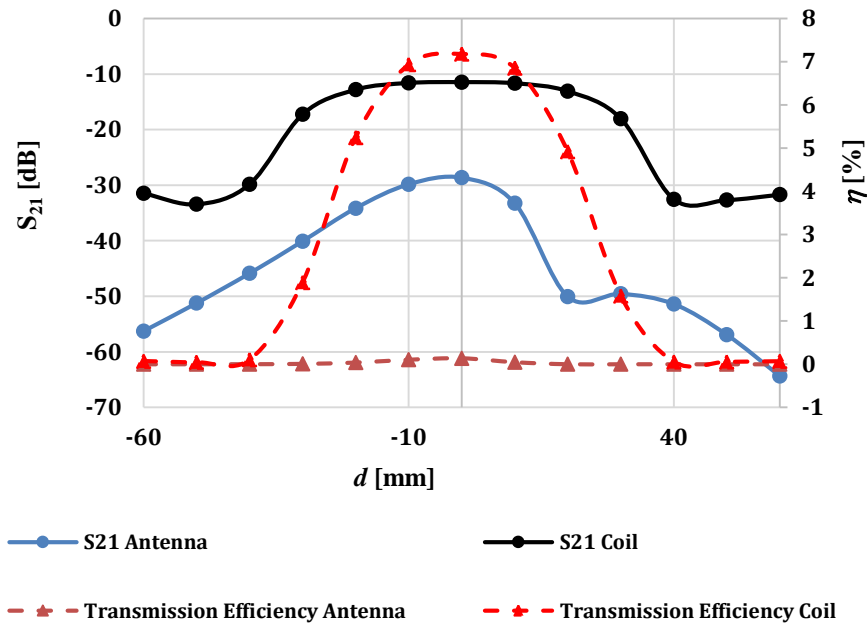
Fig. 4.4. η and S_{21} under lateral misalignment condition at 15 mm depth.

Fig. 4.5 shows S_{21} and η vs. d for both antenna and coil pairs while the separation is kept at 30 mm. It can be noted that the lateral misalignment has a small effect on the values of S_{21} and η for coil in the range of d = [-30 mm to 30 mm]. They reach their maximum of S_{21} = -17.26 dB and η = 1.88% at d = 0. These values drop rapidly after d

53

increases to more than 40 mm. However, the value of S_{21} for the antenna is maximum at d = -10 (S_{21} = -17.14 dB).
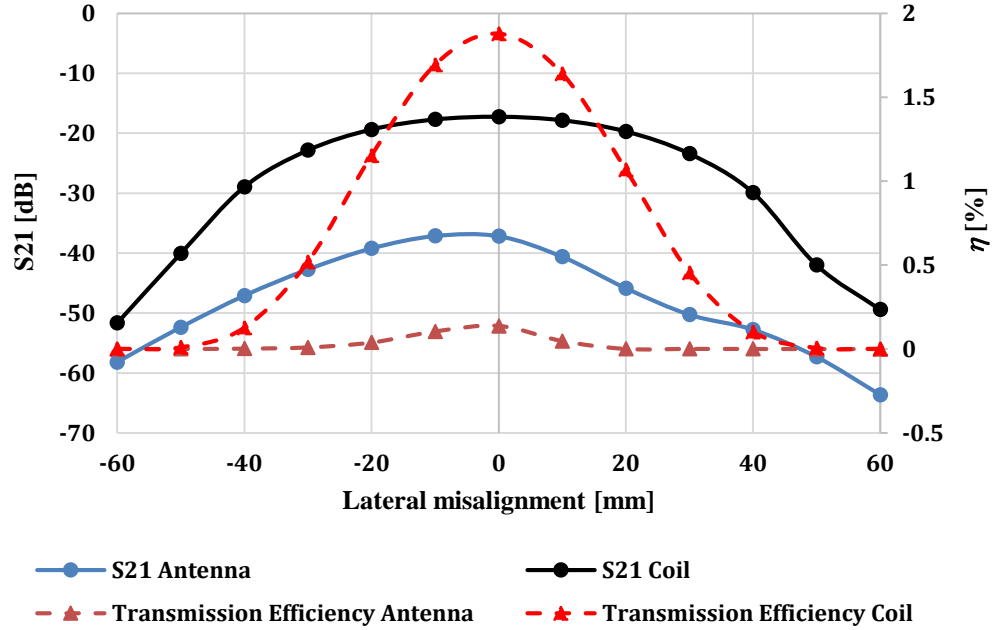
Fig. 4.5. η and S_{21} under lateral misalignment condition at 30 mm depth.

Fig. 4.6 shows S_{21} and η versus θ for both antenna and coil pairs. Maximum η occurred at $\theta = 0^o$ for coil while it occurred at $\theta = 40^o$ for the antenna. The angular misalignment moving counterclockwise around z-axis improves the antenna's performance. This could be due to non-symmetric pattern caused by the shorting pin in the antenna.
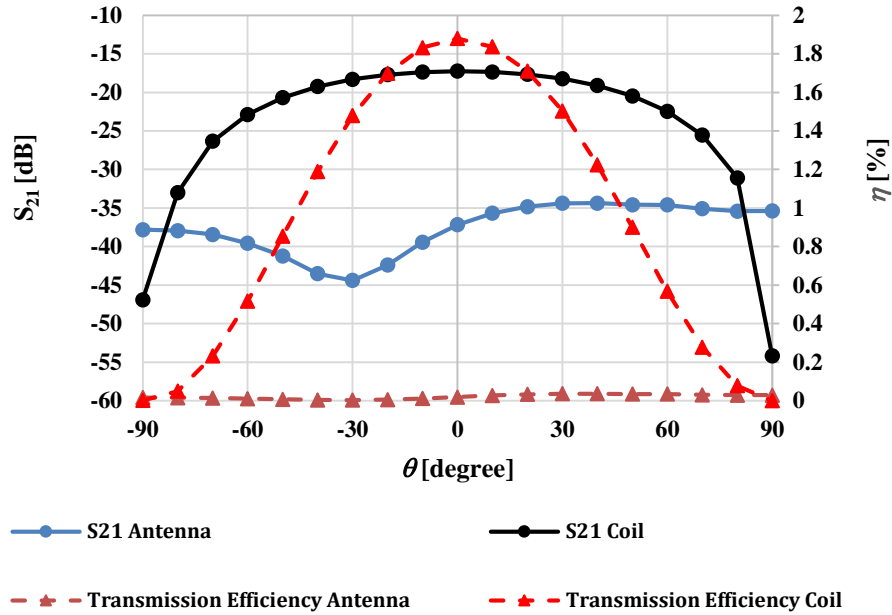
Fig. 4.6. η and S_{21} under angular misalignment condition at 30 mm depth.

We should pay attention to two important points. First, the value of S_{21} for the antenna is not symmetrical around the *y*-axis, this is because of the presence of the shorting pin, that causes non-symmetric patterns. For coils, the presence of the antennas and shorting pin have a small effects on the values of *k*, S_{21} and η. Misalignments (changing *d* and θ) shows symmetrical changes. Second, S_{21} and η for coil pair are much better than the antennas combination, but since the antenna is used for data communication only, the efficiency is still acceptable.

Fig. 4.7 shows S_{21} and η versus *d* for both antenna and coil pairs under rotating IM combination in *x*-axis condition, while EX and IM are separated by 30 mm. It can be noted that it has no effect on the values of S_{21} and η for coil due to its shape symmetry. On the other hand, for the antenna part S_{21} values are stable for angles less than 40° and angles

more than 150°. However, it has effect for angles between 40° to 150°, the worst case occurred at 105°.
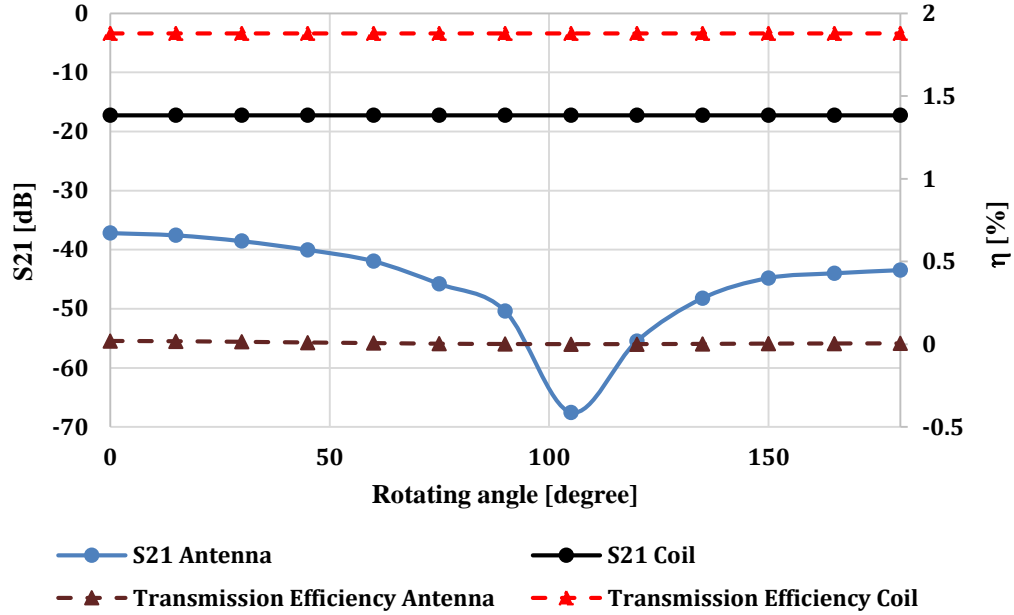
Fig. 4.7. η and S_{21} under rotating IM combination around x-axis at 30 mm depth.

4.5 Chapter Summary

In this Chapter, we studied the lateral and angular misalignment effects on coil/antenna performance for hybrid power transfer and communication system design. As a combined system, under lateral misalignment, our design is stable for d range -10 mm to 10 mm. Comparing to $d = 0$, S_{21} variation is less than 0.2 dB, and 4.6 dB for the coil and antenna pairs, respectively (at 15 mm depth). Furthermore, at 30 mm depth, the system is stable for d changing from -30 mm to 30 mm. On the other hand, the system is stable under angular misalignment for θ changing in the range of 0° to 60° and under Φ less than 40° and more than 150°. Comparing the results with $\theta = 0$, S_{21} changes are less than 5.2 dB for coils pair, and less than 2.6 dB for the antenna pair (at 30 mm depth).

5   OPTIMIZATION OF PLANAR SPIRAL COIL

Optimization method is applied to determine the transmitter and receiver coils dimensions. Optimization is used in order to increase the coupling coefficient and to improve efficiency. For most of the biomedical applications, a strict limitation on receiver size exists. The receiver is implanted in the body inside lossy tissues. Furthermore, there are safety considerations on the power levels. The limitations on size and power, along with the losses requires to maximize the efficiency of the coupling. This study proposes a new design procedure for optimizing the coupling between the coils, and therefore, the efficiency under lateral and angular misalignment conditions can be maximized.

5.1   Theoretical Model of Implanted Spiral Coil

This study provides a procedure for designing single layer PCSs geometries, dimensions and quality factor, and optimizing the mutual inductance and efficiency. The design procedure takes the lateral and angular misalignment between coils into account. The major design constraints imposed by PSC fabrication technology and applications are therefore considered.

Closed-form equations and formulas are used and MATLAB programs are written to be used in combination with ANSYS Maxwell and Simpolorer software, to find the optimal coil geometries, and to simulate it in order to validate the design technique.

Calculations of inductance, resistance, capacitance, and mutual inductance for PSC (configuration shown in Fig. 2.2) are introduced as follows.

5.1.1 Inductance

The ratio between the magnetic flux generated by a current carrying conductor and the current passing through it indicates its self-inductance L [77]. Several closed-form equations have been constructed to approximate L in PSCs. A spiral coil is shown in Fig. 2.2. From [91] was used to calculate the inductance:

$$L_s = \mu\, n^2 d_{avg} \left[\ln\left(\frac{2.46}{\varphi}\right) + 0.2\varphi^2\right] \tag{5.1}$$

$$d_{avg} = \frac{d_o - d_i}{d_o + d_i} \tag{5.2}$$

$$\varphi = \frac{d_o + d_i}{2} \tag{5.3}$$

where μ is the permeability of the conductor and φ is a parameter known as fill factor, which takes values in the range between 0 (when all the turns concentrated on the perimeter) to 1 (when the first turn starts from the center of the spiral coil and d_i is equal zero).

5.1.2 Resistance

The series resistance R_S is dominated by the DC resistance (R_{DC}) which its total value depends on the length of the conductor (l), the resistivity of the conductive material (ρ), coil trace (w) and conductor thickness (t), based on [91]:

$$R_{DC} = \frac{\rho\, l}{wt} \tag{5.4}$$

$$l = \frac{\pi}{4} \frac{(d_o^2 - d_i^2)}{(w + s)} \tag{5.5}$$

At high frequencies, the skin effect increases the AC resistance of the coil as specified in (5.6):

$$R_s = R_{DC} \frac{t}{\delta(1 - e^{-t/\delta})}$$ (5.6)

$$\delta = \sqrt{\frac{\rho}{\pi \mu f}}$$ ((5.7)

where δ is the skin depth, and f is the frequency.

5.1.3 Capacitance

Parasitic capacitance (C_s) (shown in Fig. 2.2(b)) is mainly affected by the spacing between the spiral coil traces and their surrounding materials. This study adopted an approach in finding the value of C_s using a combination of theoretical and measurement results in [91]:

$$C_s = l \frac{27.8\, \varepsilon_{reff}}{ln\left(\frac{\pi(u - w)}{w + t} + 1\right)} \, [pF]$$ (5.8)

$$\begin{cases} \varepsilon_{reff} \cong 1 & u < h \\ \varepsilon_{reff} = \dfrac{\varepsilon_r + 1}{2} & u \approx h \end{cases}$$ (5.9)

where ε_{reff} is the effective relative electric permittivity, u is equal to $(w + s)$ referring to Fig. 2.2(b) and h is the height of the insulator.

5.1.4 Mutual Inductance

A PSC can be considered as a set of single turn coils with a concentric diameter equal to $(d_i + n(w + s))$, connected in series. In this work, we consider the effect of lateral and angular misalignment between the pair of single turn coils to calculate the mutual inductance. Fig. 5.1 shows two types of misalignments. Based on the method used in [103],

we need to define the following parameters in order to calculate the mutual inductance

between inclined circular loop in any position:

a. The diameter of the transmitter and receiver loops, $d_{oTX(i)}$, $d_{oRX(i)}$

b. The parameters $\vec{a}, \vec{b}, and\ \vec{c}$ defining the normal vectors of the plane that
    containing the receiver coil.

c. The center of the receiver coil, (x_c, y_c, z_c).

The partial mutual inductances between every two turns of PSC pair can be

(a)   (b)
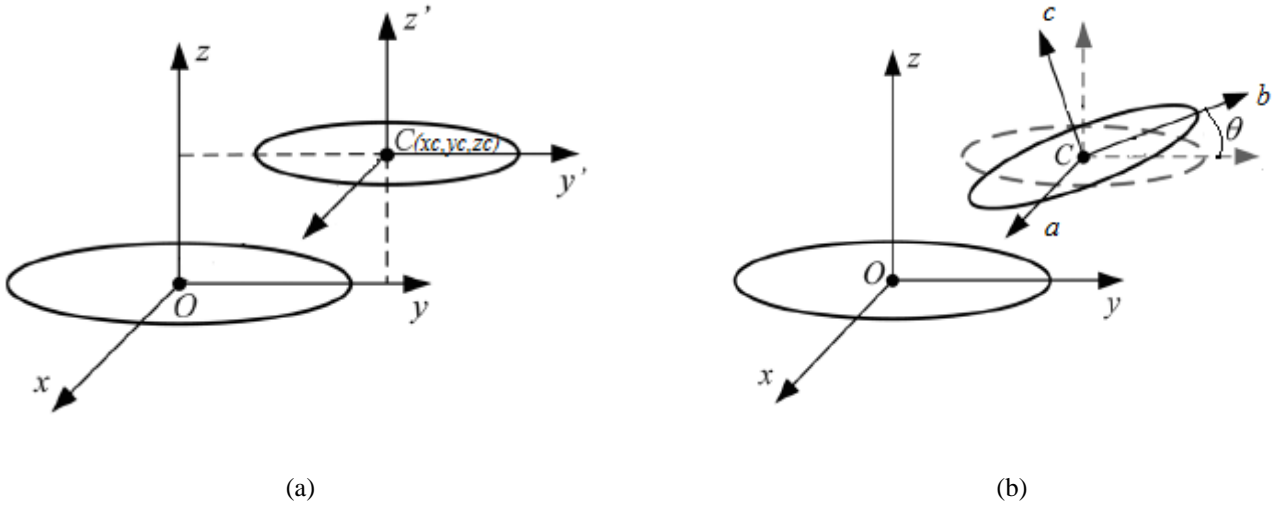
Fig. 5.1. Two types of misalignment (a) lateral. (b) angular.[103].

expressed as follows:

$$M_{ij} = \frac{\mu d_{oRX(j)}}{2\pi} \int_0^{2\pi} \frac{[p_1 \cos\varphi + p_2 \sin\varphi + p_3]\, \Psi(\nabla)}{k\sqrt{V_o^3}}\, d\varphi \tag{5.10}$$

where M_{ij} is the mutual inductance between transmitter coil number i and receiver coil

number j, $\varphi \in [0, 2\pi]$ is a parameter angle and the following sequence of definitions should

be calculated prior to evaluate (5.10):

$$\alpha = \frac{d_{oRX(j)}}{d_{oTX(i)}}, \qquad \beta = \frac{2x_c}{d_{oTX(i)}}, \qquad \gamma = \frac{2y_c}{d_{oTX(i)}}, \qquad \tau = \frac{2z_c}{d_{oTX(i)}}$$

60

$$l = \sqrt{a^2 + c^2}, \qquad L = \sqrt{a^2 + b^2 + c^2}$$

$$p_1 = \frac{\gamma c}{l}, \qquad p_2 = -\frac{\beta l^2 + \gamma ab}{lL}, \qquad p_3 = \frac{\alpha c}{l}, \qquad p_4 = -\frac{\beta ab - \gamma l^2 + \tau bc}{lL}$$

$$p_5 = -\frac{\beta c - \tau a}{l}, \qquad A_o = 1 + \alpha^2 + \beta^2 + \gamma^2 + \tau^2 + 2\alpha(p_4 \cos\varphi + p_5 \sin\varphi)$$

$$V_o^2 = \alpha^2 \left[\left(1 - \frac{b^2 c^2}{l^2 L^2}\right) \cos^2\varphi + \frac{c^2}{l^2} \sin^2\varphi + \frac{abc}{l^2 L} \sin 2\varphi \right] + \beta^2 + \gamma^2$$

$$- 2\alpha \frac{\beta ab - \gamma l^2}{lL} \cos\varphi - \frac{2\alpha\beta c}{l} \sin\varphi,$$

$$\nabla = \sqrt{\frac{4V_o}{A_o + 2V_o}}, \qquad \Psi(\nabla) = \left(1 - \frac{\nabla^2}{2}\right) K(\nabla) - E(\nabla) \qquad (5.11)$$

where $K(\nabla)$ and $E(\nabla)$ are the complete elliptic integrals of the first and second kind, respectively. Once the mutual inductance between a pair of single turn coils has been calculated, the overall mutual inductance can be generated by the summation of the partial mutual inductance between every turn on one coil (transmitter i), and all the other turns of the other coil (receiver j). By adding all the values of partial mutual inductance M is obtained as:

$$M = \sum_{i=1}^{n1} \sum_{j=1}^{n2} M_{ij}(doTX(i), doRX(j)) \qquad (5.12)$$

and

$$k = \frac{M}{\sqrt{L_1 L_2}} \qquad (5.13)$$

where L_1 and L_2 are the inductance of the transmitter coil and receiver coil, respectively, calculated using (5.1).

To validate the results of calculating the value of coupling coefficient generated from MATLAB program, under misalignment condition, a model that has been described in [80] was used. The model is as follows:

a. The transmitter and receiver coils are spiral shape.

b. The value *of d_{oTX}* is 40 mm and d_{oRX} is 20 mm.

c. d_{iTX} and d_{iRX} values are specified relative to the total value of d_{oTX} and d_{oRX}. In this work, it is assumed that $d_i = 0.34d_o$ for both transmitter and receiver.

d. 21 turns for the transmitter and 9 turns for the receiver coils were considered.

e. The distance between the transmitter and receiver coils was 10 mm.

Both coils were simulated on FastHenry-2 and the value of coupling coefficient under lateral misalignments conditions along sweeping X- and Y-axes are recorded in [80]. Fig. 5.2 compares the results reported in [80] and our results.
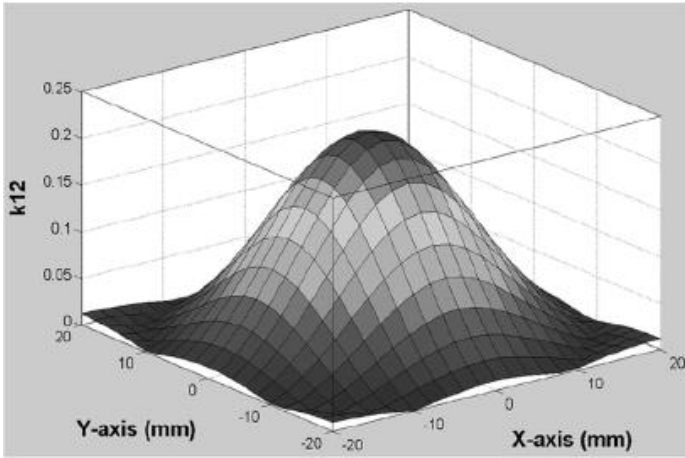
(a) Fig. 7(a) from the paper [80]
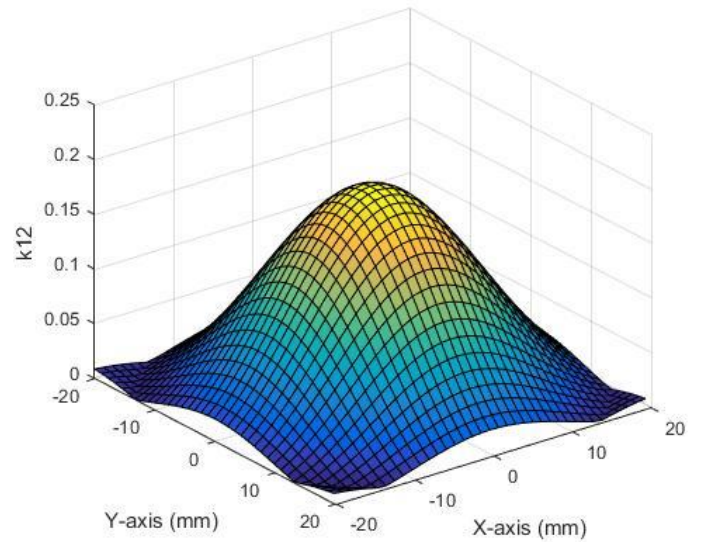
(b) proposed MATLAB Simulation

Fig. 5.2. Calculating coupling coefficient for two spiral coils with lateral misalignments in x and y-directions, (a) results from paper. (b) present work.

Another check for angular misalignment is done in order to compare our calculations. In [1] authors calculated the coupling coefficient between two identical single turn rectangle coils (coil's dimensions are not determined). The distance between the transmitter and receiver is 10 mm. The system was simulated in order to calculate the k for three positions:

A: Coils are in parallel

B: Coils are perpendicular.

C: Coils are on the same plane.

Fig. 5.3 depicts the coils in these three different positions.

(a)   (b)   (c)
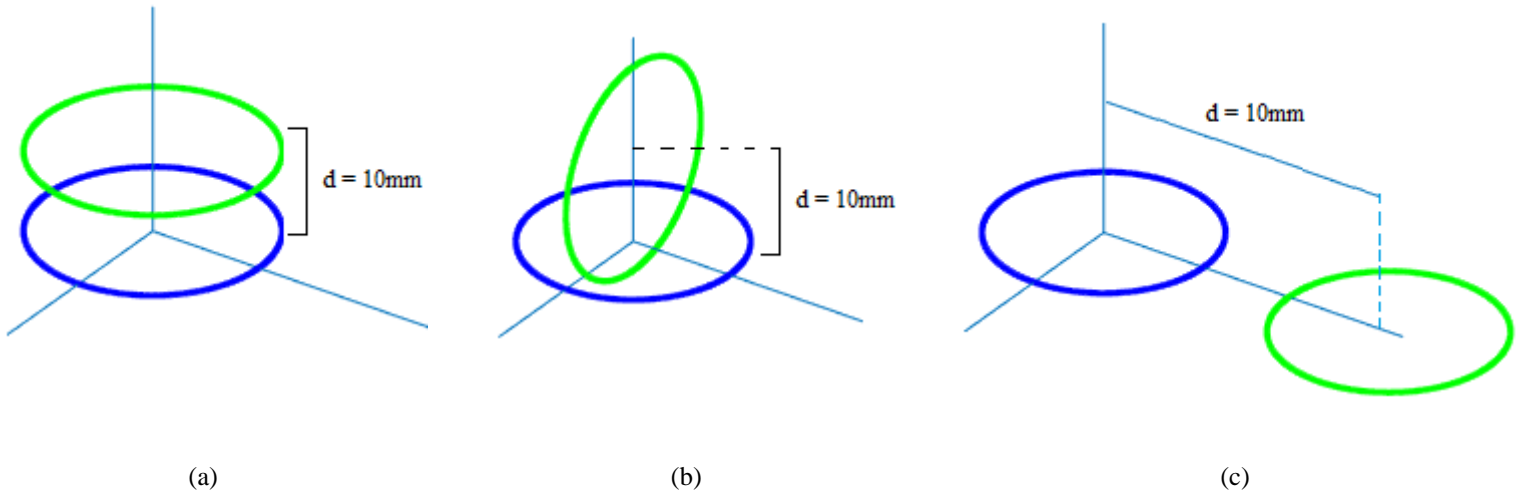
Fig. 5.3. Different positions of coils (a) Position A. (b) Position B. (c) Position C

This calculation was done for circular shape coils, and not for the rectangular ones. The system was modeled in the same manner, but for two identical one turn circle shape coils with 10 mm relative transfer distance between the coils. Table 3.1 provides the values of positions of the coils. The results are shown in Fig. 5.4.

Table 5.1. Values of the three cases studied in [1].

Position	Center of the receiver (x_c, y_c, z_c)	Angular misalignment normal vector $(\vec{a}, \vec{b}, \vec{c})$
A (Parallel)	(0,0,10)mm	(0,0,1)
B (Perpendicular)	(0,0,10)mm	(0,-1,0)
C (Both coils in the same plane)	(0,10,0)mm	(0,0,-1)

64
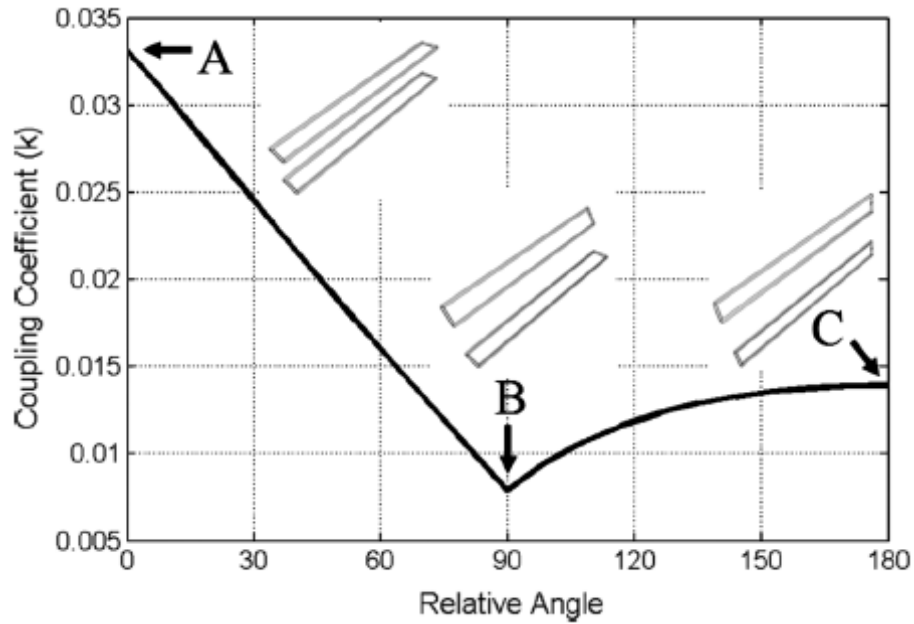
(a)
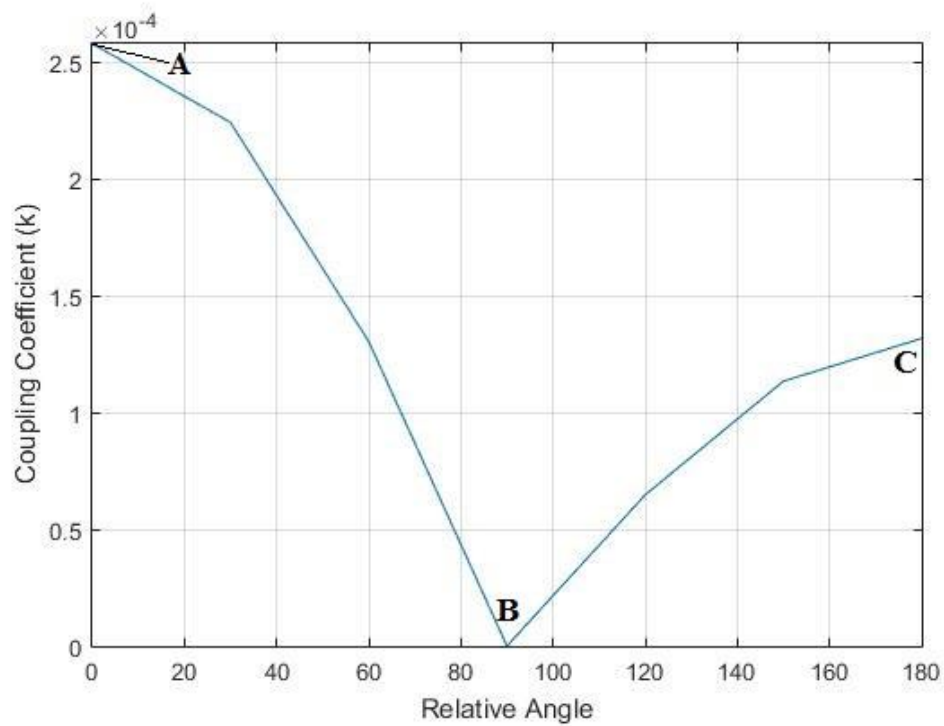
(b)

Fig. 5.4 Calculating coupling coefficient for one turn symmetric coils, (a) Simulation results for one turn identical rectangular coils with unspecified dimensions (distance between coils = 10 mm) [1]. (b) Simulation results of proposed MATLAB program for one turn identical circular coils of 1.4 mm diameter (distance between coils = 10 mm).

The results validate the calculations for k

Authors in [80] studied the effect of misalignments on their design, but did not consider misalignments as part of the optimization process. The proposed optimization method we presented considers the misalignment.

5.2 Circuit Model and Inductive Link Efficiency

Circuit models and equations are the same as the ones presented in Section 2.3. The total η_P is calculated according to (5.14):

$$\eta_P = \frac{k^2 Q_1 Q_2}{1 + k^2 Q_1 Q_2 + \frac{Q_2}{Q_L}} \times \frac{1}{1 + \frac{Q_L}{Q_2}} \tag{5.14}$$

In PSCs, most of the aforementioned parameters are related to each other. For example, increasing the number of turns for the transmitter and receiver coils without making any change in the outer diameter of the coils can increase L and k. However, Q value will be decreased by increasing the value of R_s due to increased length and reduced trace. Therefore, there are optimal PSC geometries that maximize η.

5.3 Optimization Procedures for Power Transfer Efficiency

Iterative design procedures are used to perform the optimization process. This procedure starts with a set of initial values, depending on design constraints and restrictions, taking into consideration the lateral and angular misalignments effects, and ends with the optimal PSCs geometries for both the primary and secondary coils. The flow chart of this procedure is summarized in Fig. 5.5. Results are generated based on matrices calculations to observe the changes in η_p by sweeping parameters included in (5.1)–(5.14) in a wide range, then the maximum value of η_p is selected. ANSYS Maxwell and Simplorer simulations were used for verifying the values suggested by theoretical calculations.

66

1- Applying design values depending on implantable device application and machine fabrication process
Parameters: $f, R_L, w_{min}, s_{min}, \mu, \varepsilon, \sigma, t, h, r, d_{oRX}$

2- Applying the worst case lateral and angular misalignments
Parameters: $Center_{RX}, Normal\ Plane_{RX}$

3- Applying initial values for PSC geometries for both transmitter and receiver coils
Parameters: $d_{oTX}, d_{iTX}, d_{iRX}$

4- Optimization the outer diameter and trace of the transmitter coil
Parameters: d_{oTX}, w_{TX}

5- Optimization the inner diameter and trace of the receiver coil
Parameters: d_{iRX}, w_{RX}

6- Optimization the outer and inner diameter of the transmitter coil
Parameters: d_{oTX}, d_{iTX}

7- Is the efficiency improvement less than 0.1%?

No

Yes

8- Simulate the Optimized design using Ansys-Maxwell and Simplorer

Fig. 5.5. Iterative PSC flowchart.

Step 1, Applying design restrictions:

There is a set of parameters affecting the PTE that are imposed by other factors depending on (1) implantable device application and the location of implant device; and (2) machine fabrication process which defines the minimum trace and spacing we can achieve during preparing the coils prototype. Table 5.2 summarizes these parameters for an implantable device in [105]. The power carrier frequency f has an effect on η and optimal geometries of PSCs. In this design, we consider $f = 1$ MHz to decrease the effect of Self-Resonance Frequency (SRF) of PSC coil.

Table 5.2. Design restriction values.

Parameter	Symbol	Value
Operating frequency	f	1MHz
Load resistance in secondary part	R_L	500Ω
Maximum conductor trace	w_{max}	2500μm
Minimum conductor trace	w_{min}	350μm
Minimum conductor space	s_{min}	250μm
Medium permeability	μ	1
Substrate dielectric constant (FR4)	ε	4.4
Conductor material conductivity	σ	5.88×10^7
Conductor thickness	t	35.56μm
Substrate thickness	h	1.587mm
Transfer distance	r	10mm
Outer diameter of the implanted coil	d_{oRX}	20mm

Step 2, Applying the worst case values of the lateral and angular misalignment:

The lateral and angular misalignments between the primary coil and secondary coil are defined by applying the values of secondary coil's center (x_c, y_c, z_c), and vector of normal plane $(\vec{a}, \vec{b}, \vec{c})$, please refer to Fig. 5.1. These values are selected based on the worst allowed condition. The displacement between the primary and secondary coils is 10 mm. Table 5.3 summarize the conditions that were considered in this study.

68

Table 5.3. Lateral and angular misalignment cases.

Case #	Case description	Ceter$_{RX}$ (x_c, y_c, z_c)mm	Normal Plane$_{RX}$ $(\vec{a}, \vec{b}, \vec{c})$
1	No lateral or angular misalignment	(0,0,10)	(0,0,0)
2	Lateral misalignment 4mm	(0,4,10)	(0,0,0)
3	Lateral misalignment 10mm	(0,10,10)	(0,0,0)
4	Lateral misalignment 15mm	(0,15,10)	(0,0,0)
5	Angular misalignment 15 degree	(0,0,10)	(0,-0.259,0.966)
6	Angular misalignment 30 degree	(0,0,10)	(0,-0.5,0.866)
7	Angular misalignment 45 degree	(0,0,10)	(0,-0.707,0.707)

Step 3, *Applying initial values:*

Initial values for three parameters need to be selected before starting the iterative optimization process. Based on [6], the maximum strength of magnetic field over the distance r (10mm) could be achieved if the primary coil diameter equal to the following:

$$d_{oTX} = 2\sqrt{2}\, r \tag{5.15}$$

Table 5.4 summarize the applied initial values.

Table 5.4. Initial Design values.

Parameter	Symbol	Value (mm)
Outer diameter of primary (Transmitter)	d_{oTX}	28.3
Inner diameter of primary (Transmitter)	d_{iTX}	1.0
Inner diameter of secondary (Receiver)	di_{RX}	1.0

The number of turns n of PSC is defined according to (5.16), a larger number of turns results in an increase of the values of L, M, $R_{s,}$ and Q.

$$n_{TX} = \frac{\varphi_{TX}}{\varphi_{TX} + 1} \times \frac{d_{oTX}}{w_{TX} + s_{TX}} \tag{5.16}$$

Minimum values of w and s were considered to be the minimum values it could be achieved by fabrication resolution.

Step 4, *Optimizing the outer diameter and trace of transmitter PSC:*

In this step, the geometry of the transmitter will be optimized while the geometry of the receiver stays unchanged. (5.1) to (5.14) were applied using initial values from the previous three steps in order to find η_p while sweeping d_{oTX} and w_{TX} in a wide range. After completion of this step, the values of d_{oTX} and w_{TX} will be changed to their optimal values achieved at maximum η_p. Increasing w_{TX} yields to an increase in the efficiency by reducing R_{s1} and increasing Q_1.

Fig. 5.6 shows the result of the final iteration of case 1 for w_{TX}, d_{oTX} and η_p. It can be seen that the best values are $d_{oTX} = 63.3$mm at $w_{TX} = 2500$µm and accordingly $\eta_p = 24\%$.
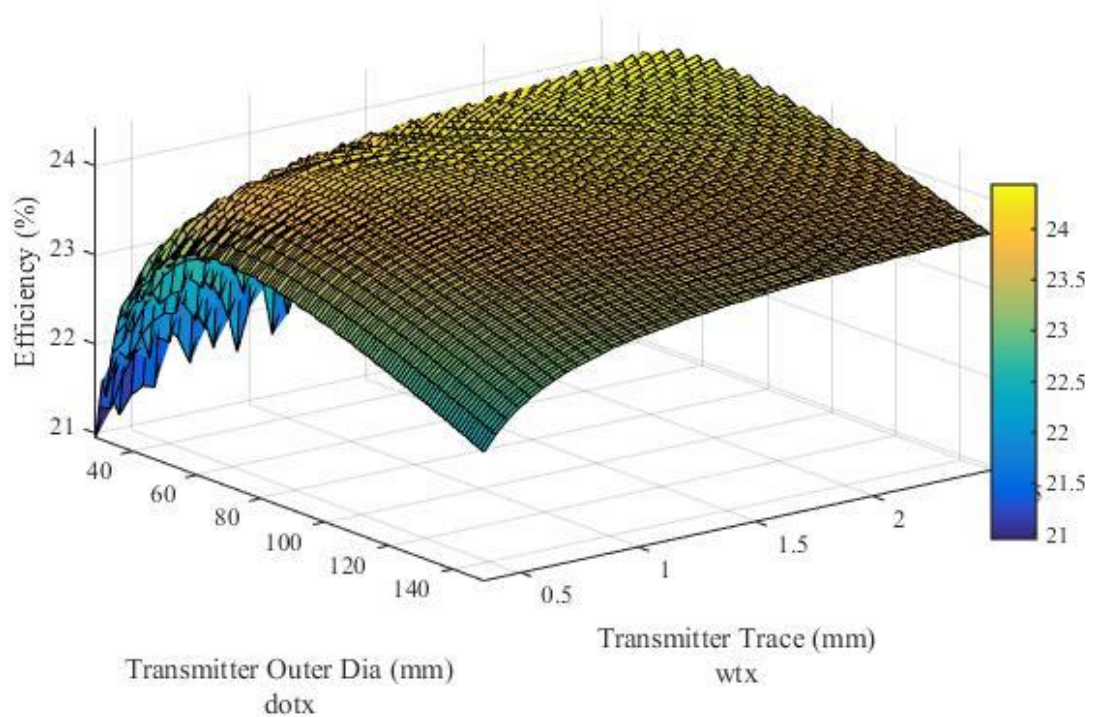
Fig. 5.6. Case 1, η versus d_{oTX} and w_{TX} at 1MHz.

70

Step 5, *Optimizing the inner diameter and trace of receiver PSC:*

After temporarily determine the transmitter PSC geometry in step 4, we focus on the receiver part considering that the d_{oRX} is already specified in step 1. In this step, we applied equations from (5.1) to (5.14) again. η_p is also calculated while sweeping d_{iTX} and w_{RX} in a wide range for the receiver coil. After finishing this step, the values of d_{iTX} and w_{RX} of the receiver PSC will be changed to their optimal values achieved at maximum η_P. Fig. 5.7 shows the results of the final iteration of case 1. The maximum efficiency is achieved at the minimum value of w_{RX}, which is defined by the fabrication technology limits (350μm). The optimal value achieved for $d_{iTX} = 2.5$mm.
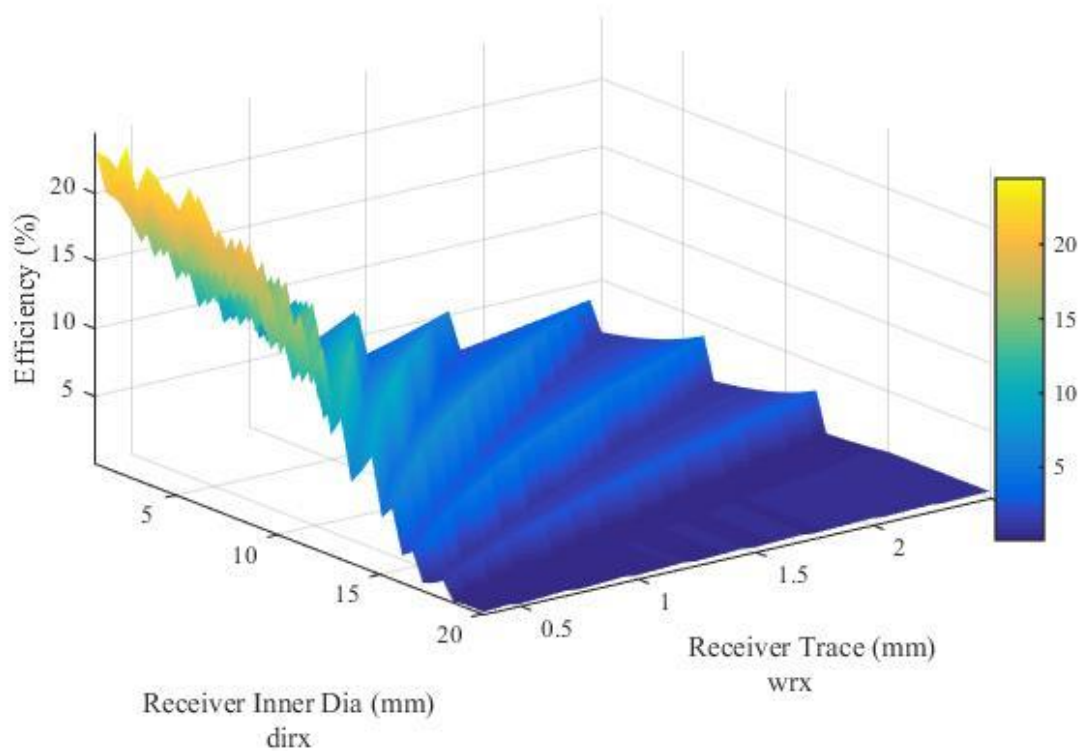
Fig. 5.7. Case 1, η versus d_{iRX} and w_{RX} at 1MHz.

Step 6, *Optimizing the outer and inner diameter of transmitter PSC:*

In this step, we return to the transmitter PSC and also find η while sweeping d_{oTX} and d_{iTX} in a wide range. Since the trace and spacing are constants in this step, they will affect the number of turns directly using (5.16).

After finishing of this step, the values of d_{oTX} and d_{iTX} are changed to their optimal values again. Fig. 5.8 shows the result of the final iteration for case 1. It clearly shows that the efficiency is maximum at $d_{iTX} = 5.5$ mm and $d_{oTX} = 63.3$ mm.
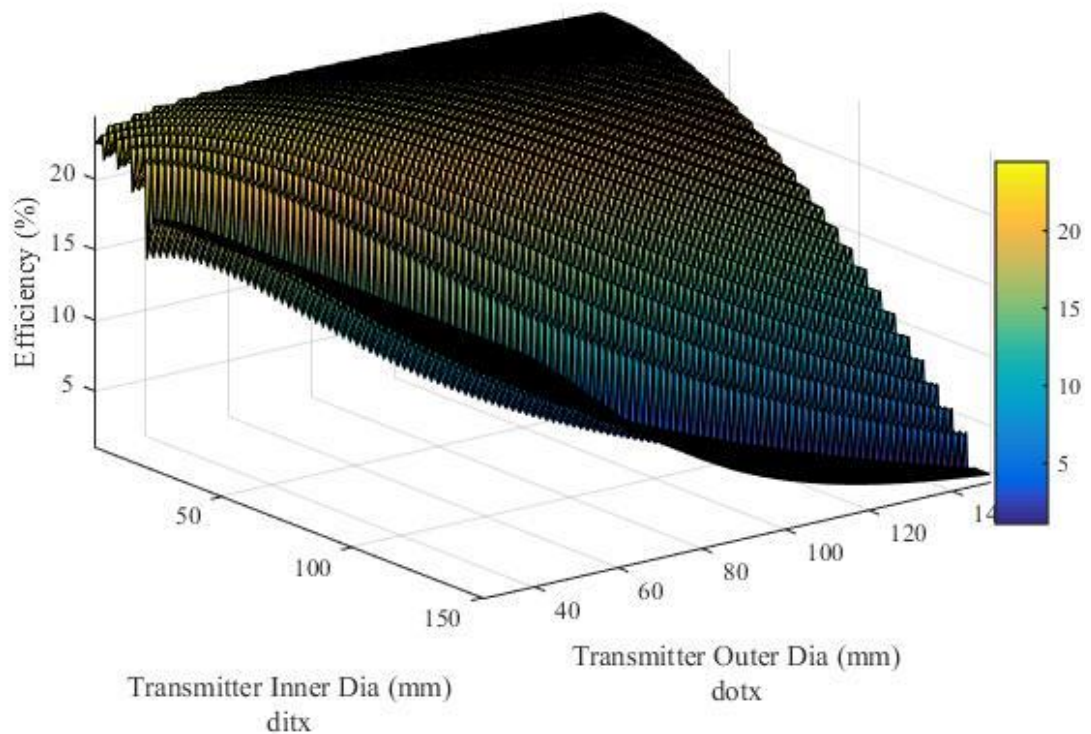
Fig. 5.8. Case 1, η versus d_{oTX} and d_{iTX} at 1MHz.

Step 7, *Iterations by going to step 4:*

The PSC geometries of the transmitter and receiver generated in step 6 improve η_P comparing to initial values in step 1. However, more improvement is possible by iterating from step 4 to step 6. Iterations will be continued until efficiency improvement $(\eta_{P(current\ step)} - \eta_{P(previous\ step)})$ is less than 0.1%.

5.4   Results

The optimization procedures were applied to all the cases in Table 5.3. The results are summarized in Table 5.5.

Table 5.5. Optimized geometries for PSCs.

PSC Parameter	Case 1	Case 2	Case 3	Case 4	Case 5	Case 6	Case 7
d_{oTX}	63.3mm	64.3mm	80.3mm	96.3mm	59.3mm	57.3mm	52.3mm
d_{iTX}	5.5mm	6.5mm	11.5mm	22mm	7mm	5mm	5.5mm
d_{oRX}	20mm	20mm	20mm	20mm	20mm	20mm	20mm
d_{iRX}	2.5mm	2.5mm	2.5mm	2.5mm	2.5mm	2.5mm	2.5mm
w_{TX}	2500μm	2500μm	2500μm	2500μm	2500μm	2500μm	2500μm
w_{RX}	350μm	350μm	350μm	350μm	350μm	350μm	350μm
n_{TX}	11	11	13	14	10	10	9
n_{RX}	15	15	15	15	15	15	15
η_P at r=10mm	24.2	24.07	23.47	22.71	24.11	23.85	24.67

The final geometries of all cases were simulated using ANSYS Maxwell and Simplorer, to validate the theoretical results. Fig. 5.9 shows the simulation setups of case 2 and case 6.

(a)   (b)
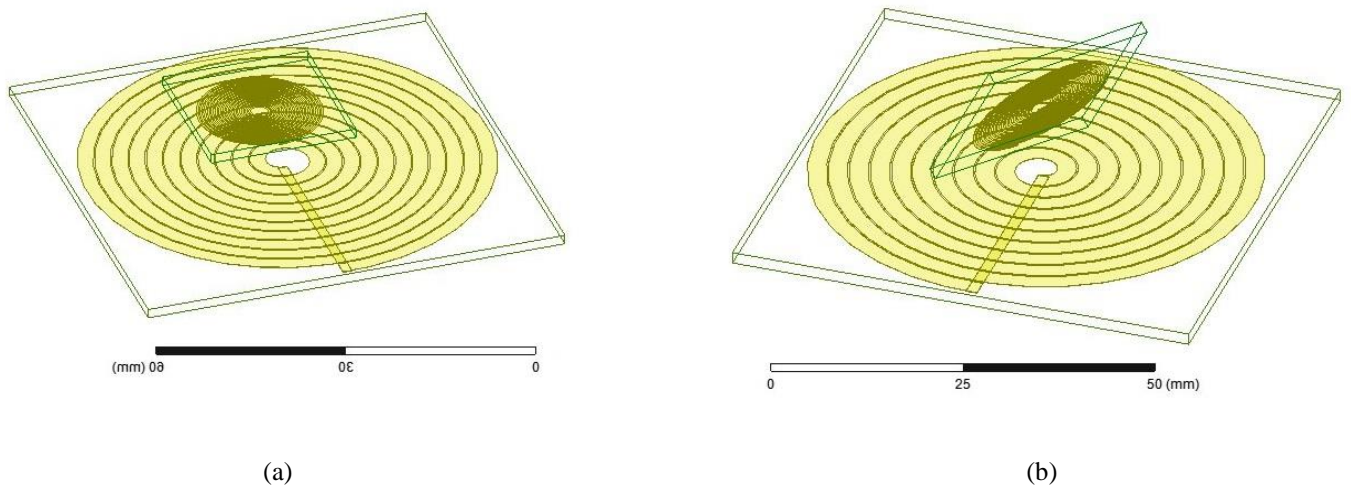
Fig. 5.9. ANSYS Maxwell simulations for (a) Case 2. (b) Case 6.
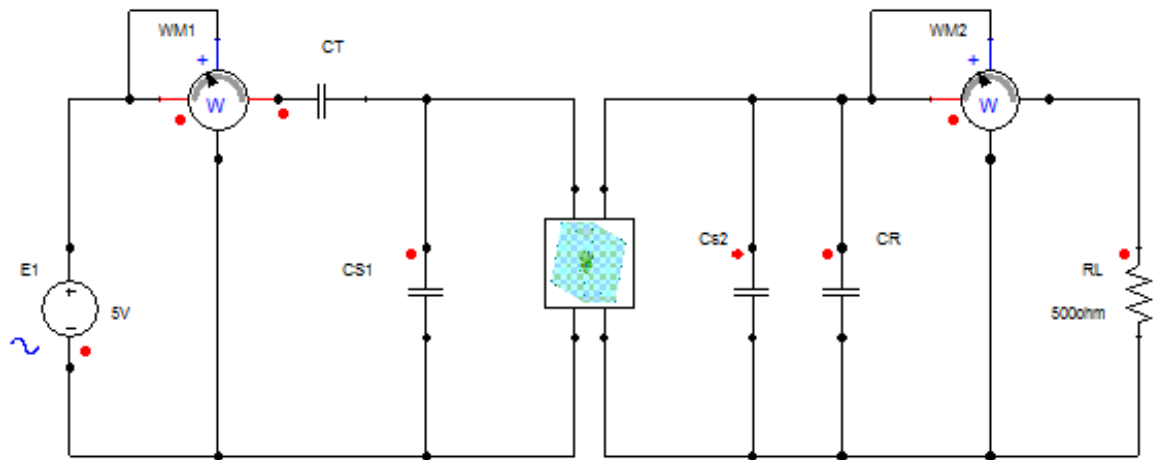
Fig. 5.10. Circuit schematic in ANSYS Simplorer simulation.

The simulation results compared with the calculations for all cases of misalignments are shown in Fig. 5.11.

74
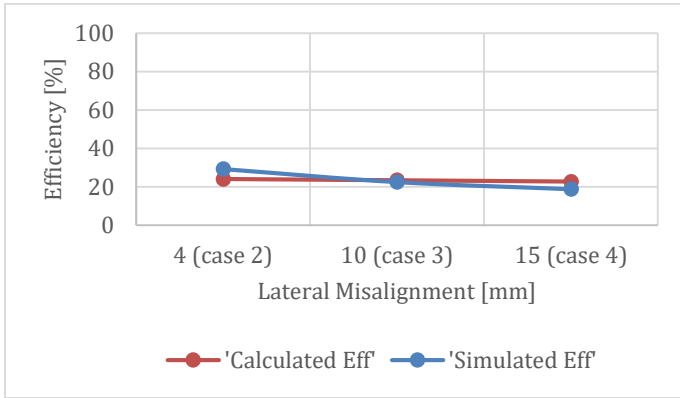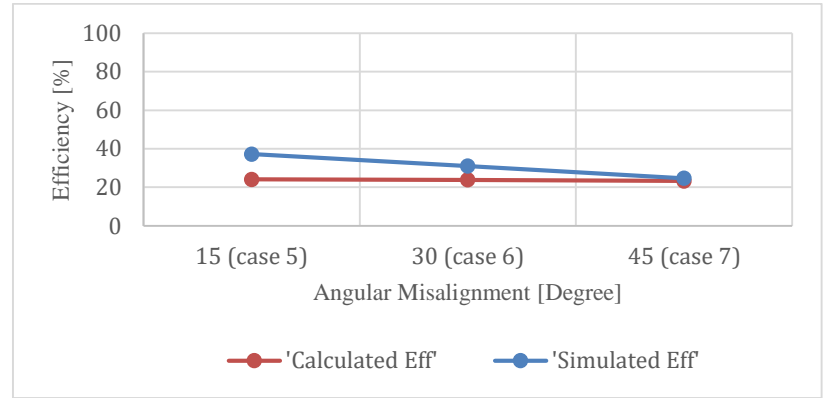
Fig. 5.11. Simulation and calculation result for efficiency for (a) lateral misalignment, and (b) angular misalignment.

In order to study how increasing the value of lateral and angular misalignments affect the optimal design value of d_{oTX} and d_{iTX} on the transmitter side, the followings steps are taken (1) In Fig. 5.12 the maximum value of lateral misalignment that has been considered in Table 5.3 with the optimum values of d_{oTX} and d_{iTX} that have been achieved in each case are shown and summarized in Table 5.5. Fig. 5.12 shows that both optimum values of d_{oTX} and d_{iTX} are increased when a larger value of lateral misalignment is considered. In Fig. 5.12(a) optimum value of d_{oTX} equals to 64.3 mm at 4mm lateral misalignments between coils. Optimum d_{oTX} starts to increase to approximately 25% more for the next two cases then, until it reaches 96.3 mm at 15 mm lateral misalignment. Lateral misalignments also affect the optimal value of d_{iTX}. This value is increased when the lateral misalignment is increased. The rate of increase in the optimum value d_{iTX} is much more than the rate of increase in the optimum value of d_{oTX} .

75
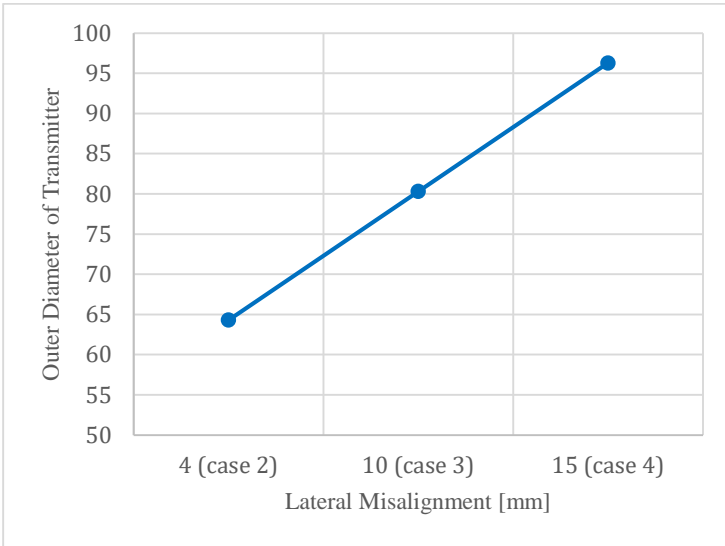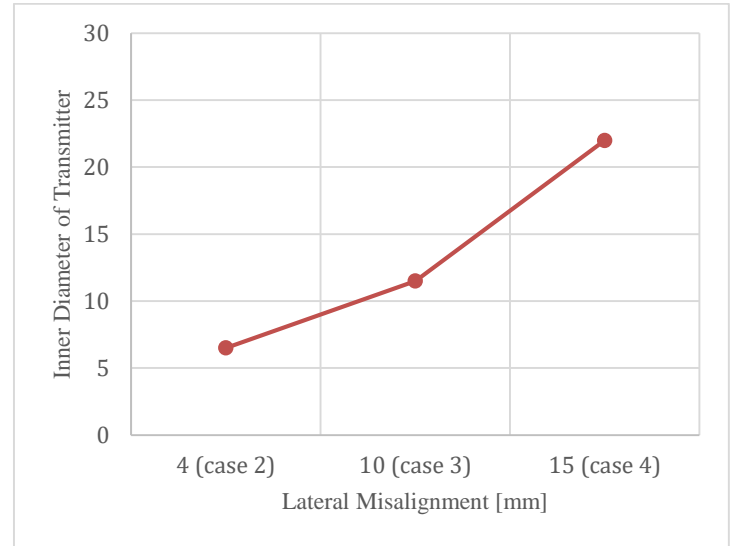
(a)   (b)

Fig. 5.12. Maximum value of lateral misalignment vs. (a) Outer diameter $d_{oTX.}$. (b) Inner diameter d_{iTX}.

Angular misalignments also affect the optimum values of d_{oTX} and d_{iTX}, In Fig. 5.13 one can see that the optimal achieved value of d_{oTX} is decreased while the angle of misalignment is increased. On the other hand, the optimum value of d_{iTX} has decreased initially, and then it is increased, with a smaller rate, as the misalignment angle is increased.
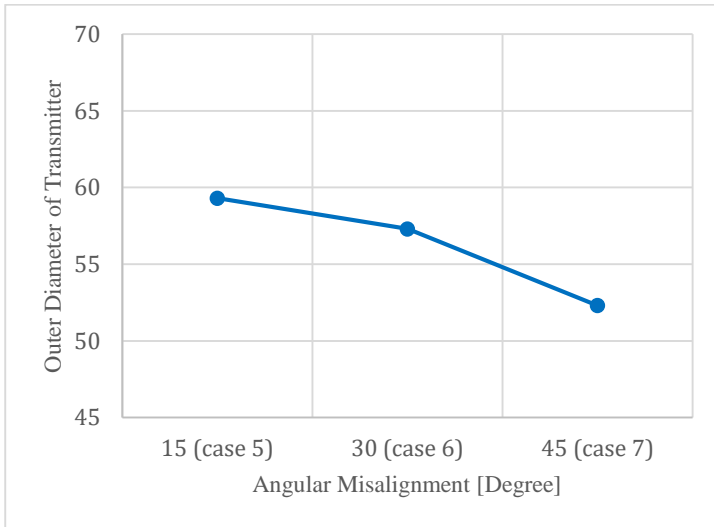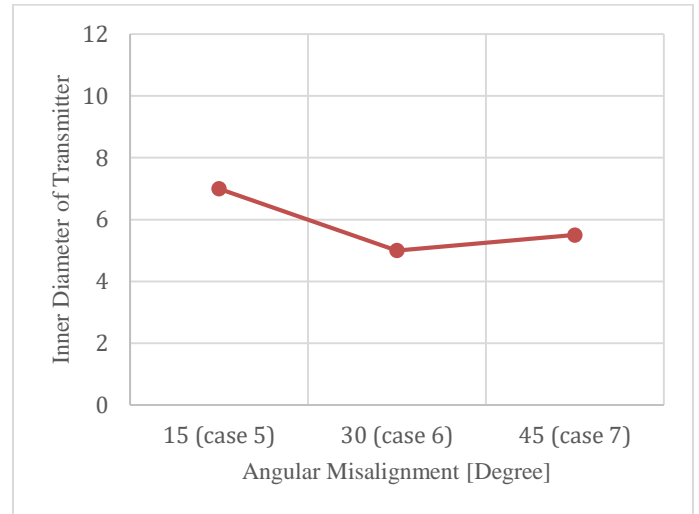
(a)   (b)

Fig. 5.13. Maximum value of angular misalignment vs. (a) outer diameter $d_{oTX.}$, and (b) inner diameter d_{iTX}.

76

6   EFFECTS OF BENDING ON HYBRID IMPLANTED POWER TRANSFER AND WIRELESS ANTENNA SYSTEM

Recently, industrial and academic researchers have shown significant interest in the field of designing unified systems consisting of WPT and a communication data link, especially for biomedical applications. Ideally, the maximum coupling occurs when the position of the EX combination and the IM combination is aligned. However, in practice, bending of IM combination can easily occur due to patient movement or the location of IM and anatomical shape of surrounding [106]. Additionally, the bending may be done intentionally to conform the IM device on a curved surface such as capsule or sphere, in order to make it suitable for implanting.

In [107], authors presented a miniaturized flexible electronic system design with wireless power and near-field communication capabilities for wearable devices. This chapter presents the results of our study of the bending IM. *Rad* presents the bending radius. The effects of *Rad* variation on S_{11}, S_{22} and S_{21} for the antennas, S_{21}, k, and η for the coils are studied numerically.

6.1   Coil and Antenna Design Structure

The proposed system consists of a hybrid EX and IM combinations that consist of a pair of antennas to send/receive data at 905 MHz, and a coil design that transfer power at 13.56 MHz and explained in Section 3.3. The EX combination is placed directly at the outer surface of the skin, and the IM that is embedded in a layer of muscle at 30 mm distance away from the EX. IM is considered to be printed on flexible Kapton material. The location of shorting pin to enable the EX and IM antenna to operate at 905 MHz are

77

summarized in Table 6.1. Electromagnetic properties of each body tissue in the layered body model are the same as discussed in Section 3.1.

Table 6.1. Shorting pin location for 905 MHz resonance.

Antenna location	x (mm)	y (mm)
EX	6.75	-13
IM	0.3	-9

6.2   Bending

In order to investigate the impacts of bending IM coil/antenna on the system performance, we conducted the simulations and conditions ($Rad = 40$ mm, 80 mm, and 120 mm) as shown in Fig. 6.1. The same circuit design as discussed in Section 0 was used.

(a) $Rad = 40$ mm   (b) $Rad = 80$ mm   (c) $Rad = 120$ mm
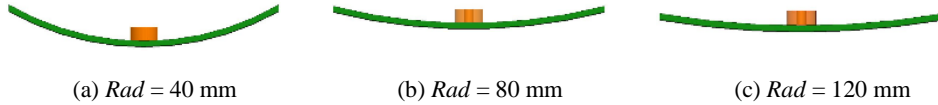
Fig. 6.1. IM hybrid design under bending condition.

6.3   Simulation Results

Fig. 6.2 shows S_{22} and S_{21} for the IM antenna. Table 6.2 shows these values at the resonance frequency for each bending radius. It can be noted that f_{oIM} vary as much as -100 MHz at $Rad = 80$ mm to +15 MHz at $Rad = 120$ mm, compared to its value at f_{oIM} for the flat case. Please note that the larger Rad the closer to the flat case.
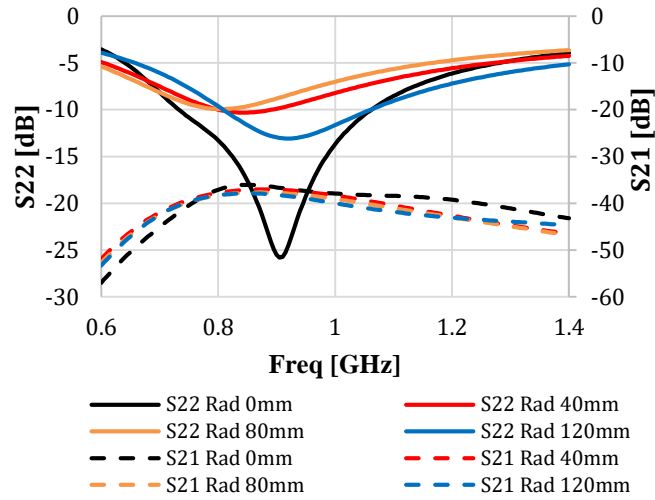
Fig. 6.2. S_{22} and S_{21} for the receiver (IM) antenna.

Table 6.2. Antenna characteristic under bending conditions.

Rad	f_{oIM} (MHz)	S_{22} [dB] @ f_{oIM}	S_{21} [dB] @ 905 MHz
0 mm	905	-25.82	-36.68
40 mm	845	-10.31	-37.12
80 mm	805	-9.93	-37.8
120 mm	920	-13.08	-38.25

While S_{21} does not vary more than 1.57 dB, bending IM has significant effects on the resonance frequency of the IM antenna and the level of S_{22}. This value is increased by 15.51 dB, 15.89 dB, and 12.74 dB at *Rad* equals to 40 mm, 80 mm, and 120 mm, respectively. Moreover, the bandwidth of he antenna under bending condition increases, as shown in Fig. 6.2.

Table 6.3 shows *k* coupling values under all bending condition case at 13.56 MHz. It can be noted that bending has very small and negligible effect on the inductive link. The minimum *k* was at *Rad* = 80 mm with around 0.005 change in comparison to the flat case.

79

Table 6.3. Coils coupling coefficient under bending conditions.

Rad	0 mm	40 mm	80 mm	120 mm
k	0.057	0.054	0.052	0.054

Fig. 6.3 shows S_{21} and η at each bending case for both antenna and coil pairs. The maximum S_{21} and η occurred at Rad = 40 mm for antenna and coil pairs. Whereas the minimum S_{21} and η occurred at Rad = 80 mm for the coil pair, and at Rad = 120 mm for the antenna pair. In general the values of S_{21} and η are not changed significantly. It should be noted that both the efficiency and transmission coefficient for coils are less affected by bending than those for the antenna pair.
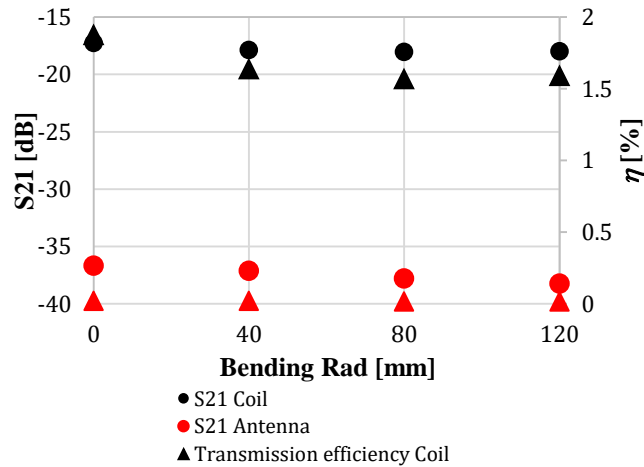
Fig. 6.3. η and S_{21} under bending condition at 30 mm depth.

6.4 Chapter Summary

In this chapter, we studied the bending effects on the performance of a hybrid power transfer and communication system design. Two main conclusions are as follow. First, for the inductive link, the system is stable at all three bending conditions. Second, for the data communication link, the system performance is acceptable under bending as much as *Rad* = 120 mm. However, increasing the bending (decreasing *Rad*) may cause severe loss in communication link and is not recommended.

7   EXPERIMENTAL VERIFICATION

7.1   Introduction

In this chapter, a thorough examination of the experimental techniques used in the verification of the simulated model are presented. The experimental setup as well as the equipment used in the experimentation are described. In addition, the experimental results for each design are introduced, and a detailed discussion of the obtained results from the simulated model and the experimental data are presented.

7.2   Phantom Preparation

Some studies have used animal tissues (beef or pig muscle) to represent structural complexities of tissue. However, variations of properties among samples are unpredictable, and may vary from typical values of human tissues.

Physical tissue models, or phantoms, are used for experimental validation of transcutaneous systems. In general, phantoms should represent the dielectric permittivity, conductivity, and losses at the frequency of interest, in addition to preferably mimicking tissue structure and shape.

An advantage of fabricated phantoms is the ability to design it for the properties at room temperature that mimic tissues at body temperature. We fabricated a phantom based on the method described in [108] to represent the muscle tissue model. Fig. 7.1 shows one fabricated sample of this phantom.

Fig. 7.1. A sample of fabricated tissue phantom.

The phantom properties were measured by Keysight high performance dielectric probe. Fig. 7.2 shows the measured permittivity of the phantom.
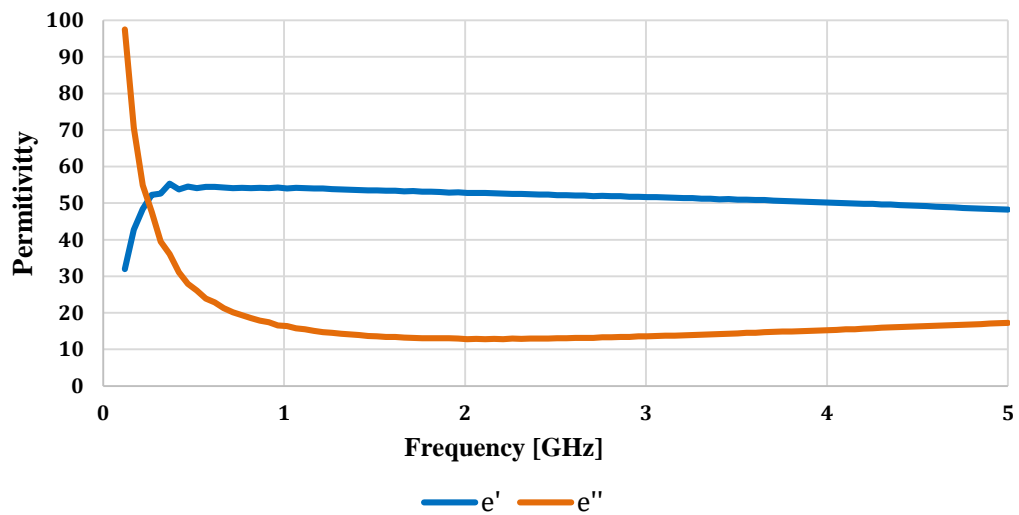
Fig. 7.2. Measured complex permittivity for the muscle phantom.

7.3 Experimental Setup and Results

7.3.1 Aligned Hybrid Design Measurements

The EX and IM coil/antenna combinations at three frequency bands (415 MHz, 905 MHz, and 1300 MHz) were fabricated on FR-4 substrate, as shown in Fig. 7.3. The system was measured in the phantom for the antenna part, and for in the air for inductive coil part. Fig. 7.4 shows the measurements setups.

(a)

(b)
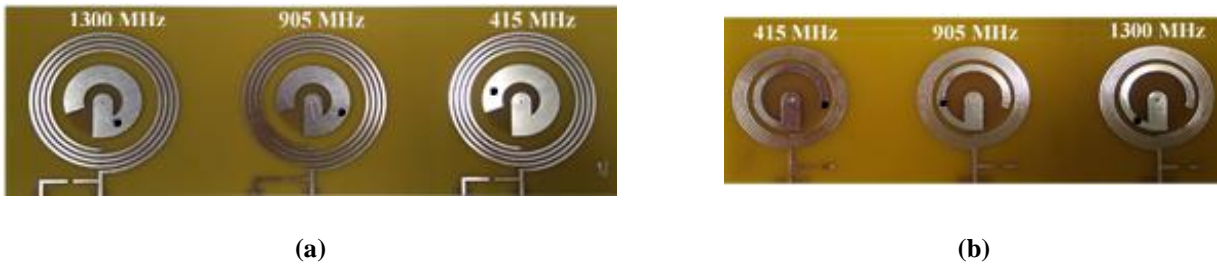
Fig. 7.3. Fabricated combinations of coil/antenna for (a) EX and, (b) IM.

(a)

(b)
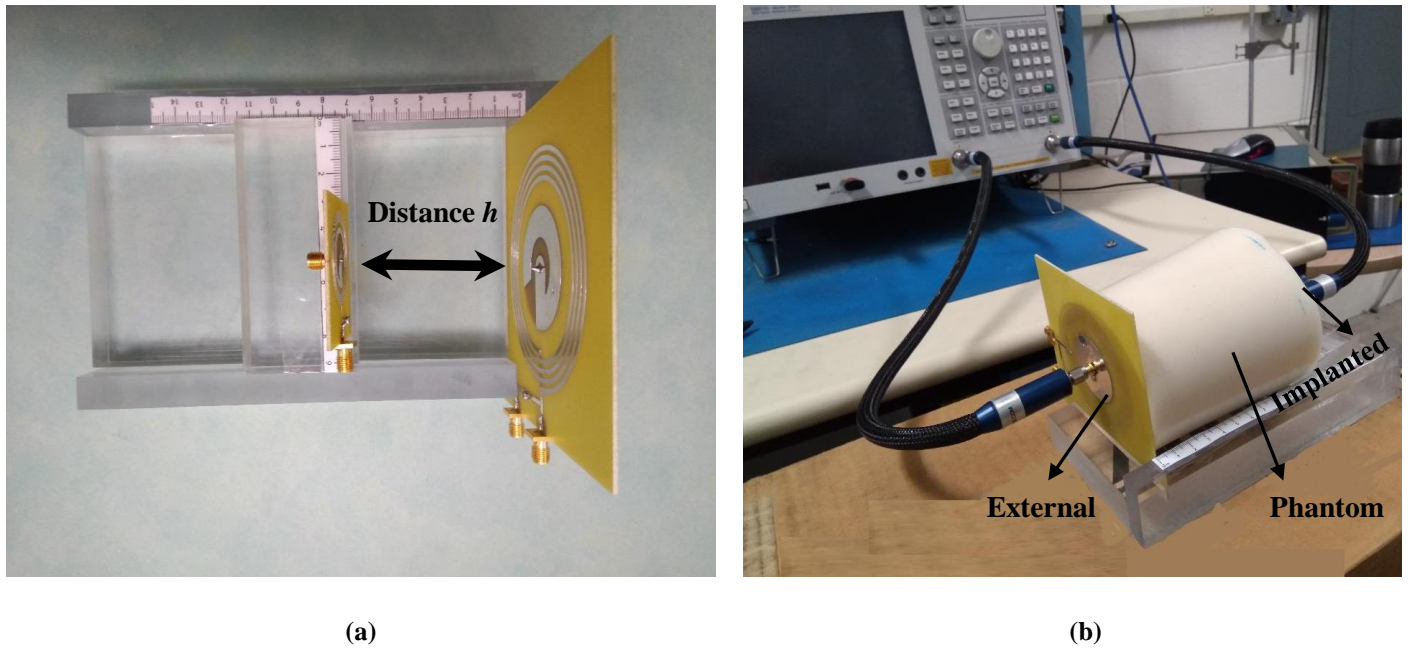
Fig. 7.4. Measurement setup in (a) air and, (b) phantom.

S-parameters were measured by a vector network analyzer (VNA). We studied the simulated performance of the antennas at all UHF bands at h=15 mm. The simulated and the measured S_{11}, S_{22} and, S_{21} with frequency at the same h are drawn in Fig. 7.5, Fig. 7.6, and Fig. 7.7. These measurements validate the simulated results.
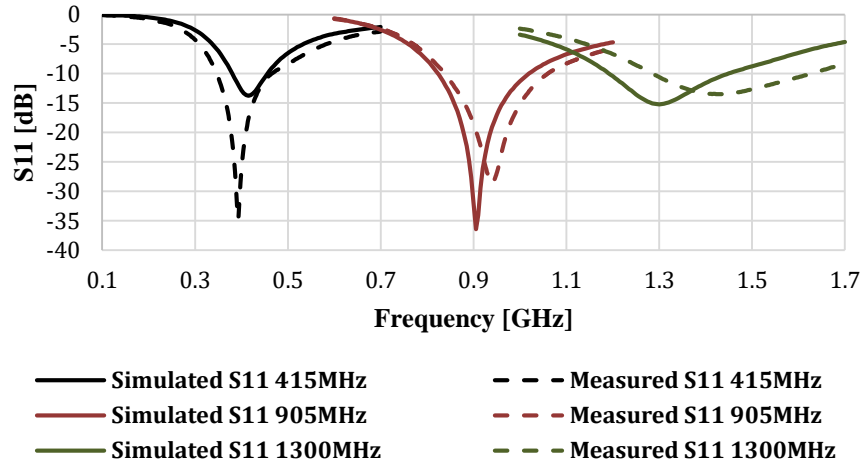
Fig. 7.5. Simulated and measured S_{11} versus frequency for UHF antenna.
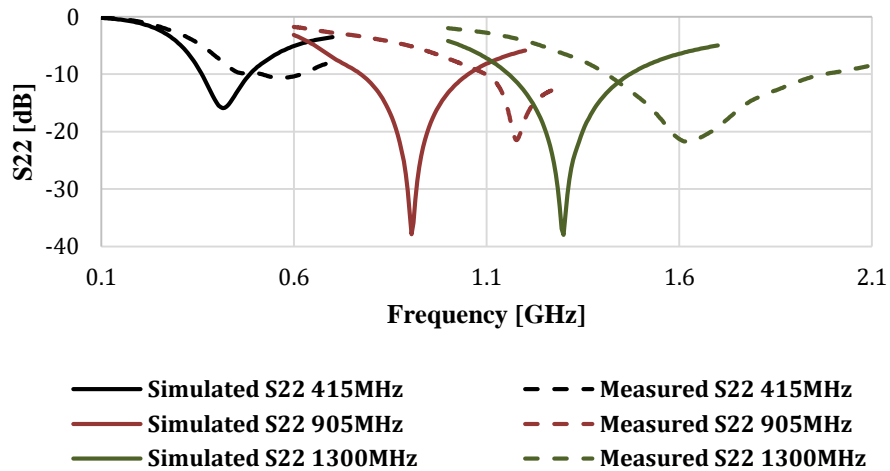
Fig. 7.6. Simulated and measured S_{22} versus frequency for UHF antenna.
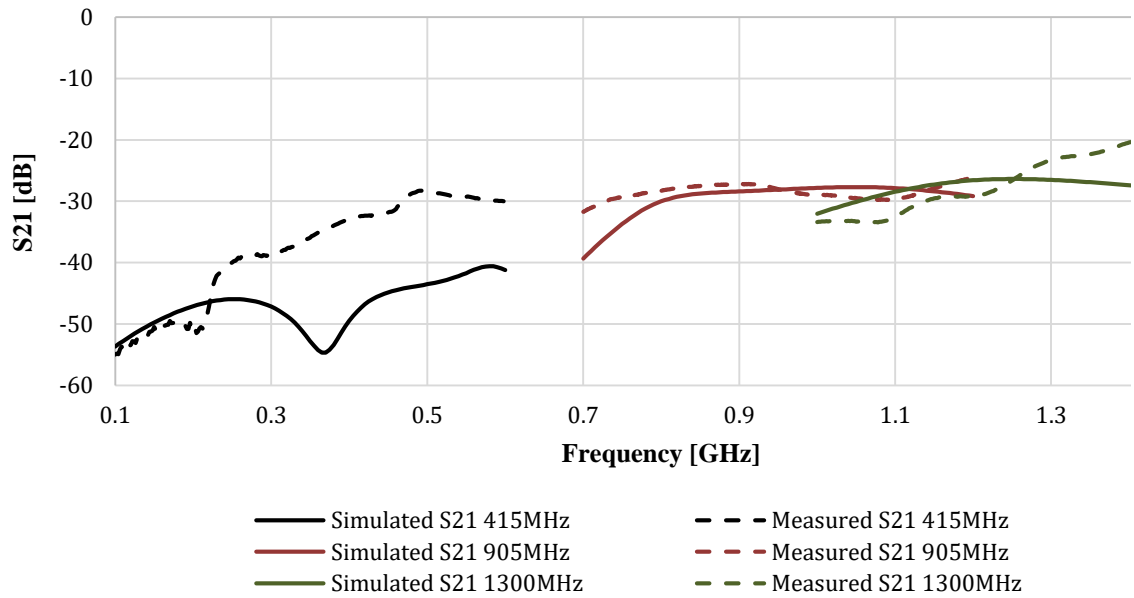
Fig. 7.7. Simulated and measured S_{21} versus frequency for UHF antenna.

We also measured the values of S_{21} at a different depth for at each of the UHF antennas, as well as for the inductive HF coils. The measured and simulated results are compared in Fig. 7.8. The measured values are approximately the same as simulated ones for the HF coils. We noticed that the measured values are close to the simulated ones for the UHF antennas, especially for *h* less than 70 mm at 905 MHz, the differences may be due to reflection and refraction that may occur as the distances are increased.
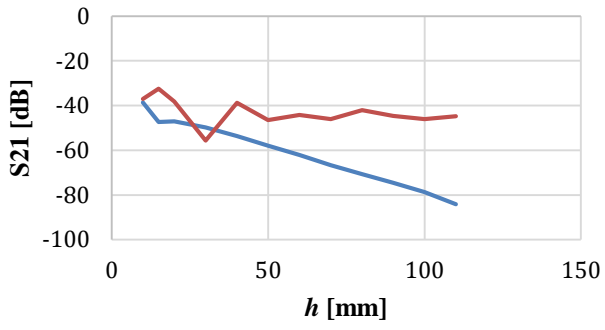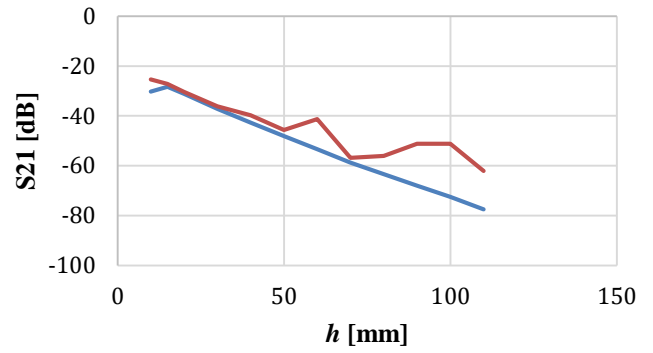
(a) 415 MHz.

(b) 905 MHz.
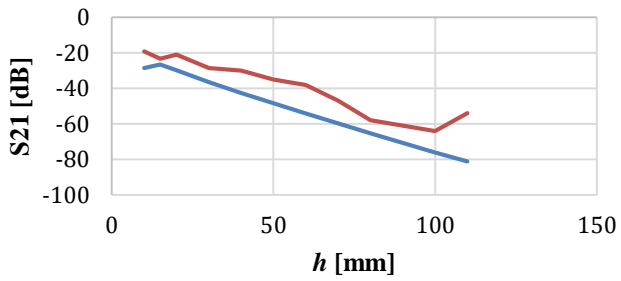
(c) 1300 MHz.
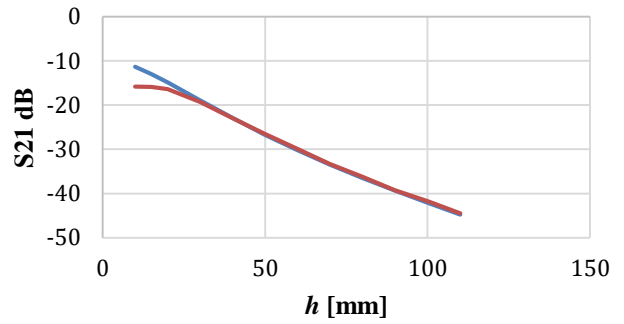
(d) 13.56 MHz (coil).

Fig. 7.8. S_{21} versus depth h .

87

7.3.2 Misalignment Measurements

In this section simulated results presented in Chapter 4 for the EX and IM combinations design under misalignment conditions are compared with the measurement results. The measurements are done for both inductive coil and antenna radiative links.

a. Inductive Coil Link

Fig. 7.9 shows the measurement setup for the inductive link, the system was tested in air at 13.56 MHz for both lateral misalignment at 15 mm and 30 mm depth, and for angular misalignment at 30 mm depth.
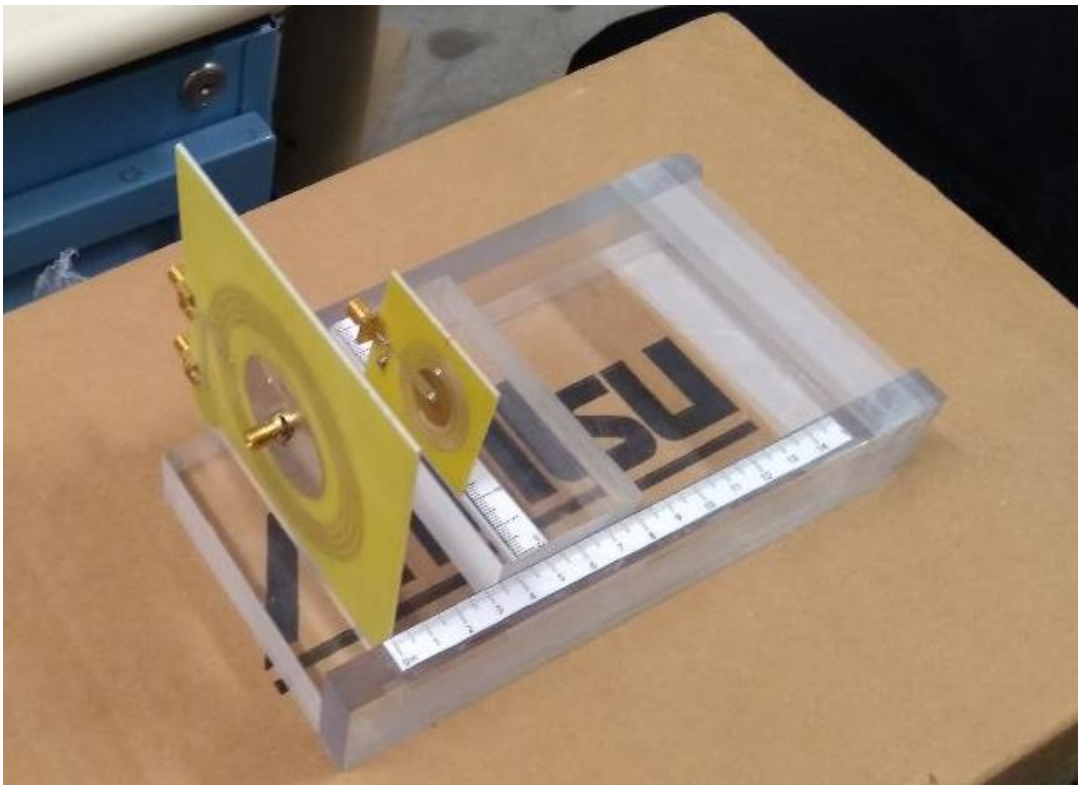
Fig. 7.9. Measurement setup for inductive link part under misalignment condition.

Fig. 7.10 shows the achieved measured values of S_{21} vs the simulated one at different misalignments conditions. The measured values are in agreement with the simulated ones, validating the proposed design.
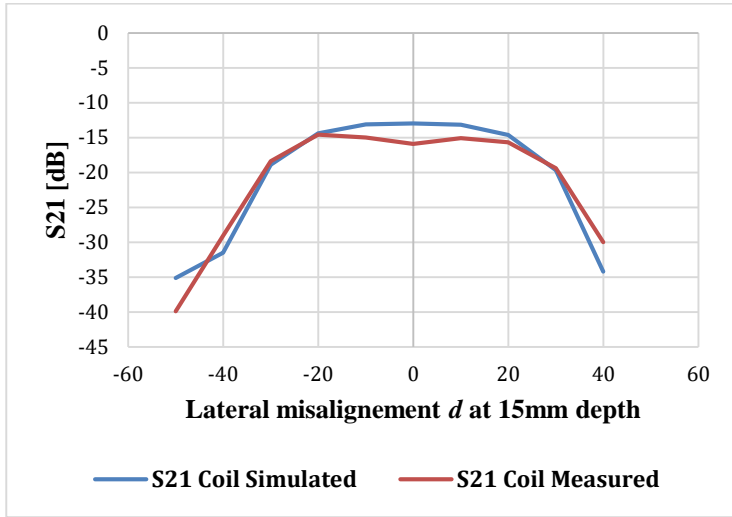
(a) Lateral misalignment at $h = 15$ mm.
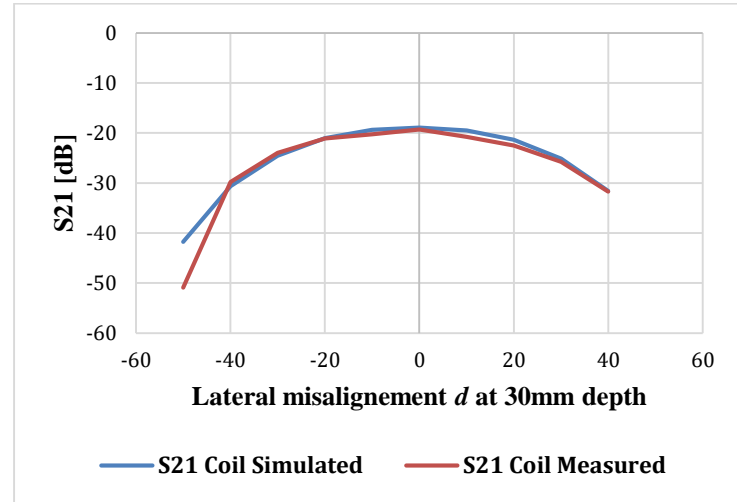
(b) Lateral misalignment at $h = 30$ mm.
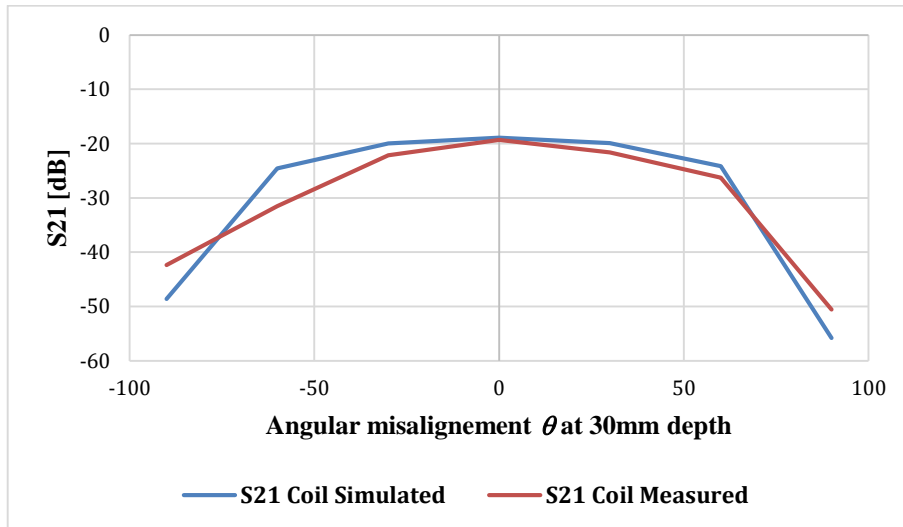
(c) Angular misalignment at $h = 30$ mm.

Fig. 7.10. Measured and simulated S_{21} for hybrid design under misalignment conditions.

b. Radiative Antenna link

Fig. 7.11 shows the measurement setup for the radiative link. The system was tested in a phantom medium at 905 MHz for also lateral misalignment at 15 mm and 30 mm depth, and for angular misalignment at 30 mm depth.
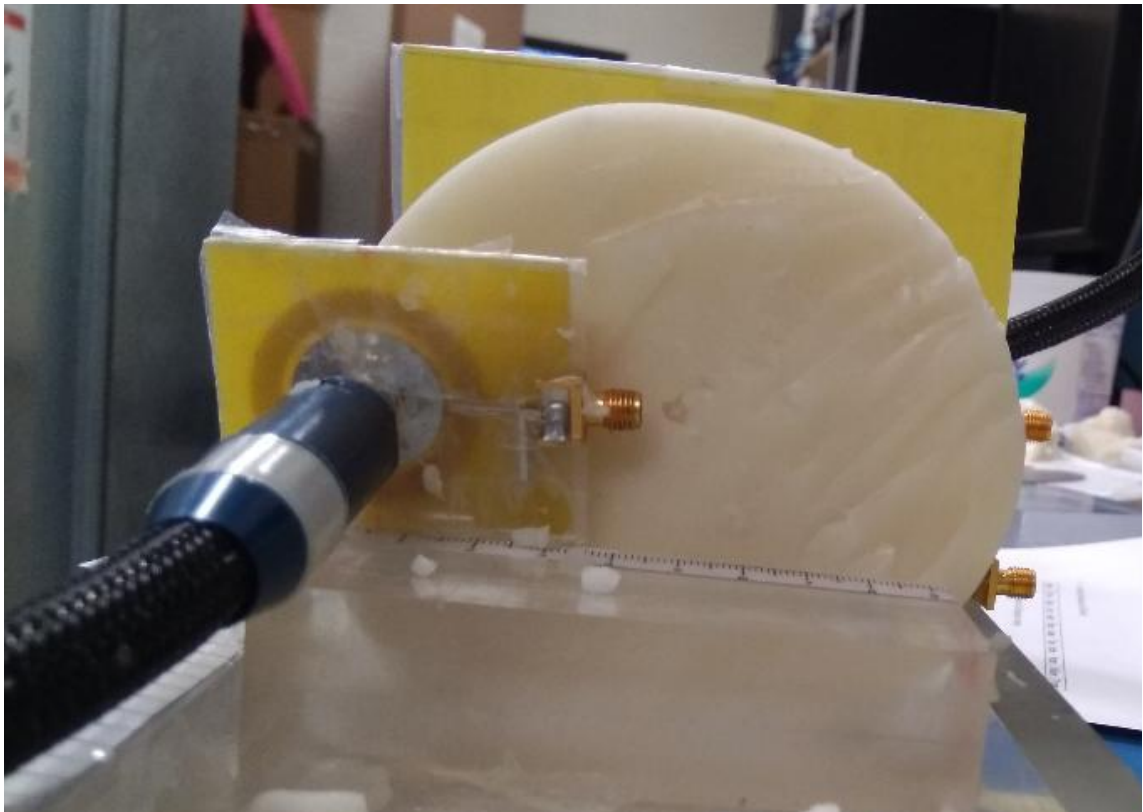
Fig. 7.11. Measurement setup for inductive link under misalignment condition.

Fig. 7.12 shows the measured values of S_{21}, comparing that with the simulated one at different misalignments conditions. Good agreement is observed. Some fluctuations are observed in Fig. 7.12 (b), this is due to reflection and refraction of radiative wave as the IM combination has been laterally moved, this is due that some part of IM combination is not

covered by phantom because of movement, also the back phantom thickness is thinner than the simulated one.
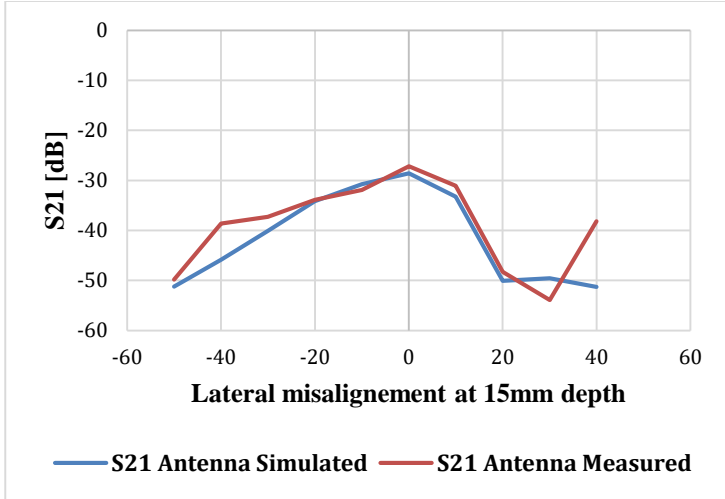
(a) Lateral misalignment at $h = 15$ mm.
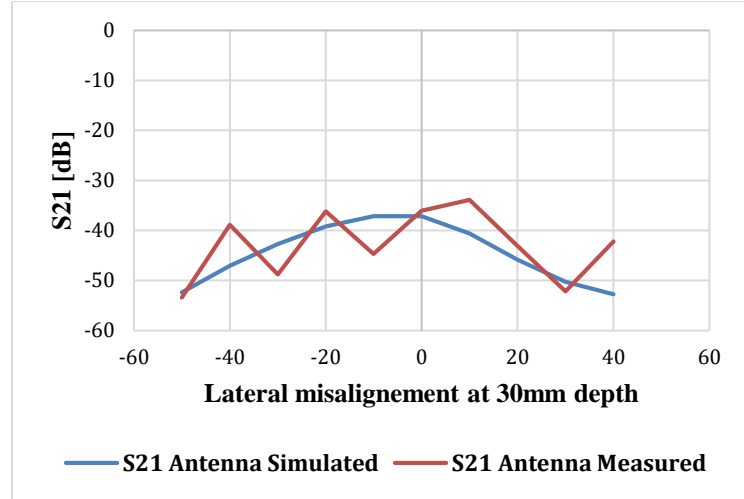
(b) Lateral misalignment at $h = 30$ mm.
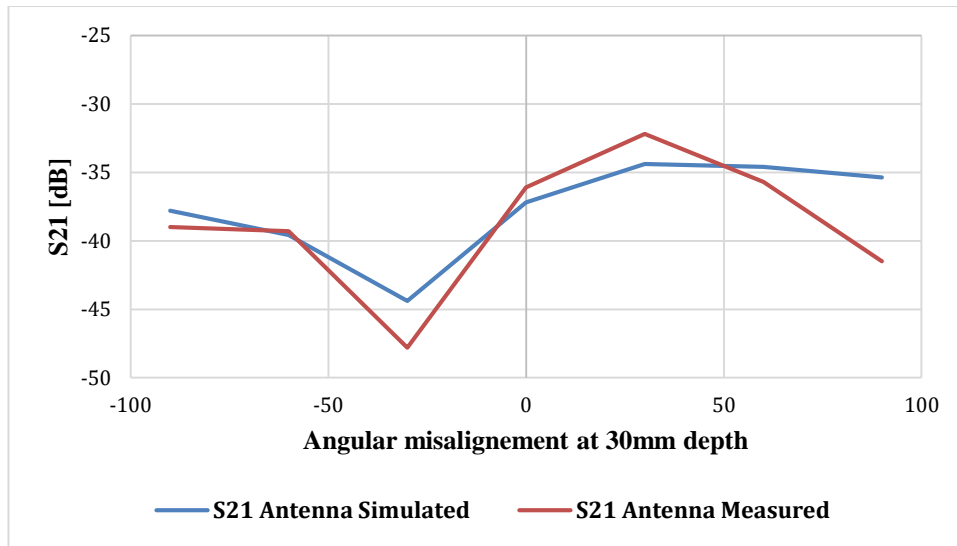
(c) Angular misalignment at $h = 30$ mm.

Fig. 7.12. Measured and simulated S_{21} for hybrid radiative design under misalignment conditions.

8 SAFE AND SECURE RADIO FREQUENCY WIRELESS POWER TRANSFER

8.1 Introduction

Recently, electromagnetic WPT systems have been developed in a rapid manner, and it is widely used for electronic products. The applicability of WPT includes low power applications, like sensors or active small medical implants, medium power applications that consume several tens of Watts [109], and high power devices that consume hundreds or thousands of Watts, like charging electric vehicles [110]. Consequently, the geometrical dimensions of the coils used in these devices range from a few millimeters to more than a meter.

Many WPT devices operate in a frequency range from 1 MHz to 50 MHz [13], while several low power medical applications use frequencies in 402 MHz – 430 MHz, and 902 MHz – 928 MHz, to transmit both data and power [111]. The strong reactive electromagnetic radiation of these systems may induce large fields in human body tissues. Therefore, it is essential to demonstrate and test the compliance of a WPT with human exposure limits to electromagnetic fields, especially before market release.

Electromagnetic field exposure is a major concern for wireless charging. Human body can be under exposure of power while using electric vehicles, sensors, and medical implants. Electromagnetic exposure needs to be rigorously analyzed to be within acceptable levels specified by safety standards, in all possible conditions. These might be daily usage such as consumer electronics, electric vehicles, and implanted devices, or occasional use, such as medical surgeries, medical examination, power transfer in emergency and disaster recoveries.

Analytical, simulations and experimental modeling are the main methods for evaluating the WPT safety. In general, existing models are limited by imprecision in anatomy of body models, tissue properties, phantom fabrication, and ignoring the physical dimensions or conditions, and the factor of duration and environmental conditions. Additionally, there is a tradeoff in modeling precision and simulation complexity. Also, there is a difficulty in constructing an accurate experimental method to measure specific absorption rate (SAR). In the following sections, we will discuss safety standards in more details.

8.2   Existing Standards

The safety of electromagnetic field exposure has been a topic of study for many years. Many countries and multiple scientific committees of national and international organizations have developed several guidelines and procedures. A comprehensive overview of the development processes of the safety guidelines in their historical manner can be found in [112] and [113].

The most prominent of these standards are as follows:

The European Union:

- International commission on non-ionizing radiation protection (ICNIRP) Guidelines [114] was published in 1998.

- In 2004, the European Union issued a directive guideline to protect workers from possible hazardous effects from electromagnetic fields.

- A revised version of ICNIRP guidelines, including scientific evidence concerning exposure to high-frequency electromagnetic fields and the resulting health consequences, was published in 2009 [115].

The United States and Japan:

- Guidelines of the National Council on Radiation Protection, which was published in 1986.

- The guidelines of the IEEE C95.1 standard [116], published in 1992. C95.1 was updated and a new version was published in 2005 [117]. The latest version was not adopted by federal communications commission (FCC).

Switzerland:

- National regulations in Switzerland used ICNIRP Guidelines published in 1998, but it was the first country to introduce precautionary limits that are 20 dB below the ICNIRP guidelines for fixed installations in the sensitive areas (e.g., schools, living areas, hospitals)

Commonwealth of Independent States (CIS):

- In these standards the exposure to electromagnetic fields is limited according to the sanitary and epidemiologic rules and regulations.

China:

- National standard for electromagnetic radiation GB 8702-88 (published in 1988) formulated by the national environmental protection agency and National standard GB 9175 (1988), formulated by the Ministry of Health [118] are used.

Two consortiums have been established to set up a technical standard for building WPT devices. However, they still use the existing safety regulations without updating them. A brief description of work of each of consortiums is as follows:

a. **Alliance for Wireless Power (A4WP):**

- The A4WP standard is used to deliver power, typically for wireless charging.

- The core of its technology is the inductive power transfer techniques used by other competing standards.

- A4WP uses a large area of the magnetic field, and this enables the device positioning requirements to be less critical, and it also allows a single power transmitter to charge multiple devices at any time.

- A4WP states that it uses magnetic resonance charging. Essentially it uses the same magnetic inductive techniques.

- A further advantage of A4WP is that it enables the possibility of charging placement. This means that chargers can be built deeper into other objects, like a desk, whilst still allowing the electromagnetic fields to penetrate into the material.

b. **Qi**:

- Qi wireless charging is a standard built cooperatively by some of the world's leading companies.

- Qi was first published for low power up WPT, to 5W. Specifications were published in August 2009. In 2011, the Wireless Power Consortium began to extend the Qi specification to medium power up to 120 W. In 2015, WPC demonstrated a high power specification that will deliver up to 1 kW.

- Official website for Qi is: https://www.wirelesspowerconsortium.com/

Generally, safety guidelines define two different kinds of exposure limits: (1) the basic restrictions shown in

Table 8.1, which define the threshold values above which the biological effects can be expected. The basic restrictions consider current density, SAR, and the internal fields to determine the safety limit. But since the direct measurement of the basic restrictions is technically difficult, the exposure guidelines organizations define (2) the maximum permissible exposure or reference levels of the incident electric and magnetic fields shown in

Table 8.2.

Table 8.1.Basic Restrictions on the SAR in W/kg according to the exposure guidelines above 100 KHz.

Standard	Average Mass	Body Region	General Public	Occupational
ICNIRP 1998 [114]	10g contiguous volume	Head and trunk	2	10
	10g contiguous volume	limbs	4	20
	Whole body	-	0.08	0.4
IEEE 2005 [117]	10g cubical volume	All without extremities and pinna	2	10
	10g cubical volume	Extremities and pinna	4	20
	Whole body	-	0.08	0.4
IEEE 1992 [116]	1g cubical volume	All without extremities	1.6	8
	1g cubical volume	Extremities	4	20
	Whole body	-	0.08	0.4
China GB 8702-88	10g cubical volume	-	2	
	Whole body	-	0.02	0.1

Both the general public and the uncontrolled mean the area where there is no knowledge or control of their exposure. Accordingly, the maximum permissible expose in the occupational and controlled environments are much higher than the general public and the uncontrolled environments.

Table 8.2. Reference Levels in the frequency range to the exposure guidelines.

Standard	f_M MHz	E General Public	E Occupational	H General Public	H Occupational
ICNIRP 1998 [114]	0.15-1	87	610	$0.73/f_M$	$1.6/f_M$
	1-10	$87/(f_M)^{0.5}$	$610/f_M$	$0.73/f_M$	$1.6/f_M$
	10-400	28	61	0.073	0.16
IEEE 2005 [117]	0.1-1	614	1842	$16.3/f_M$	$16.3/f_M$
	1-1.34	614	$1842/f_M$	$16.3/f_M$	$16.3/f_M$
	1.34-3	$823.8/f_M$	$1842/f_M$	$16.3/f_M$	$16.3/f_M$
	3-30	$823.8/f_M$	$1842/f_M$	$16.3/f_M$	$16.3/f_M$

Based on the existing standards that were summarized in

Table **8.1** and

Table 8.2, two points are concluded:

1- The magnetic field generated by typical low power transfers like the percutaneous transfer could comply with the standard documents. However, for those high-power systems that transfer tens of watts, the magnetic flux density may reach 1.25–10 µT [13], whereas the limitation is about 2 µT and 0.2 µT at 10 MHz in the IEEE 2005 and ICINRP 1998 respectively, so wireless power transfer does not always comply with magnetic field permissible international standard.

2- For electric field, for high power wireless power transfers, they may easily exceed the limitation. For example, to transfer 60 W over 2 m, previous research produced an electrical field in the range from 210 V/m to 1.4 kV/m in the frequency of 9.9 MHz [13]. The suggested maximal electric field is only 61 V/m

and 184.2 V/m for the occupational environment in the ICNIRP 1998 and IEEE 2005 guideline respectively. so wireless power transfer does not always comply with the permissible electric field international standard.

We concluded that the wireless power transfer doesn't comply with the permissible electric field and magnetic flux density mentioned in the existing standards and summarized in

Table 8.1 and

Table 8.2, which implies our need to have a specific standard for WPT safety.

8.3   CHALLENGES

Development of safety guidelines for a human having medical implanted systems
In general, safety standards do not consider the potentially strong field enhancements in the presence of active and passive metallic implants. In [119], authors objective of study was to investigate if persons with implantable medical devices are intrinsically protected by the current electromagnetic safety guidelines, they concluded that:

- The current safety guidelines do not adequately protect human with implants.
- Special considerations are required, especially in the case of novel and emerging technologies that feature strong near-fields at frequencies below 10 MHz.

More Reliable Human Numerical Models

Obviously, there are tissue variations among different body areas such as tissue thickness, and tissue properties. Also, the type of tissue is different in head or eyes than chest, hands, or feet. The differences among tissues also exist between patients, such as differences in fat, skin thickness and muscle mass.

Reviews of anatomical body models can be found in [120]–[124]. Anatomical models were developed for different genders, and age, due to the variety of tissue responses to exposure. For example, in [125] author found that children's head absorbs over two times of radio frequency than adults, furthermore, the absorption of the skull's bone marrow can be ten times greater than adults. Tissue of fetus such as nervous system seems vulnerable to temperature rises caused by high electromagnetic especially during organogenesis [126].

The most recent anatomical models are independent of the mesh with respect to their resolution and orientation in the computational domain. The virtual population models are available with special software to move and rotate them and to export them in a generic data format, which can be used with the finite difference time domain algorithm at different mesh resolutions. Recently, in [127] the models were developed by IT'IS as human numerical phantoms. However, more effort is needed to develop models suited to be used as the standard models for wireless power transfer safety.

Experimental Equipment (probes, and tissue equivalent phantoms) for Different Frequency Ranges

Tissue is a lossy dielectric material, its electromagnetic properties are defined by its conductivity, permittivity, and permeability. WPT efficiency depends on the tissue properties. However, WPT safety is a particular concern since the absorption of

electromagnetic energy by tissues can lead to tissue heating which will cause pain for patients and even tissue damage. Moreover, its reported that heating tissue that exceeds 1 degree centigrade may interfere with its behavioral and biological functions [128]. Tissue geometry and properties may be affected by electromagnetic power transfer and absorption.

In some studies animal tissue samples were used to model the structural complexity of tissue, as shown in Fig. 8.1. However, tissue properties variations are unpredictable among samples and may be different from the human tissues. In order to model the tissue in more precise manner, gel and liquid phantoms are used for experimental validation of tissue model. In general, phantoms are used to represent the dielectric permittivity, conductivity, and losses at the frequency of interest of the specified tissue.
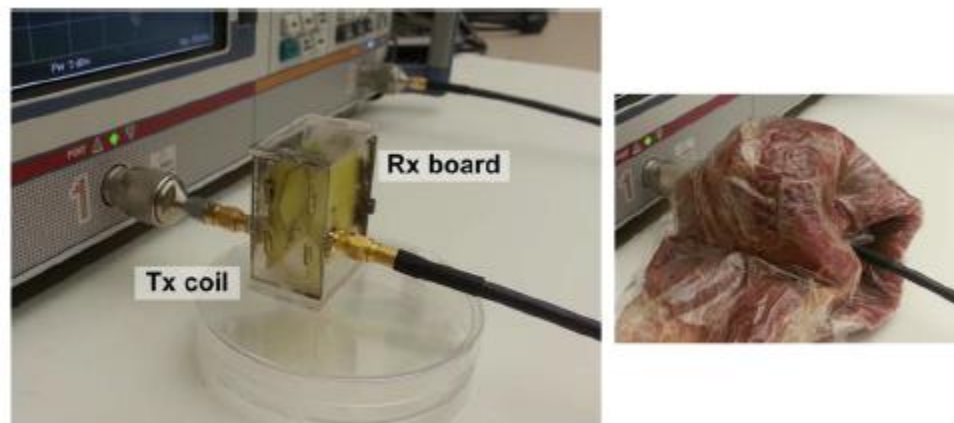
Fig. 8.1. Use of animal tissue to measure the WPT efficiency [53].

Phantom's geometry and dimension are an important consideration in addition to its structure and dielectric properties. It is difficult to fabricate phantoms that are identical to the desired anatomy. It is also difficult to match the dielectric properties of the phantoms over the frequency range. The formulations for making phantoms rely on the principle of

chemistry to achieve the required electromagnetic properties. There are several ways to fabricate the phantoms [108] [129]. Currently, benchmarking phantoms made with a standardized method of fabrication at a specific range of frequency does not exist. It is quite difficult to compare various studies as they use various types of phantoms.

Modeling the Property Variations in Tissue Models

Dielectric properties of any material are subjected to change with orientation, temperature, pressure, mixture, and molecular structure [130]. Tissue variations depend on the changes in the body composition, tissue geometry and the changes in the water content. For example, the conductivity of the body varies by 2% per degree Celsius [131].

Variation in tissue properties is a challenge in evaluating the system efficiency for wireless transcutaneous powering, the complexity and variations of tissue structure make predicting tissue properties and phantom fabrication so difficult. A good review of this topic is found in [132].

It is important to consider the representation of tissue variability in WPT design to get the right result for human safety levels.

SAR Measurements

IEEE standard C95.3 attempts to provide a standard for measuring SAR. However, the complexity of measuring electric field distribution and temperature leads to relying on the estimation of SAR through simulations. In [133], authors provide a review for measurement system and procedure for two SAR methods: (1) electric field probe method, and (2) the thermographic method. In the first method, a robot arm moves an electric field

<div align="center">(a)</div>
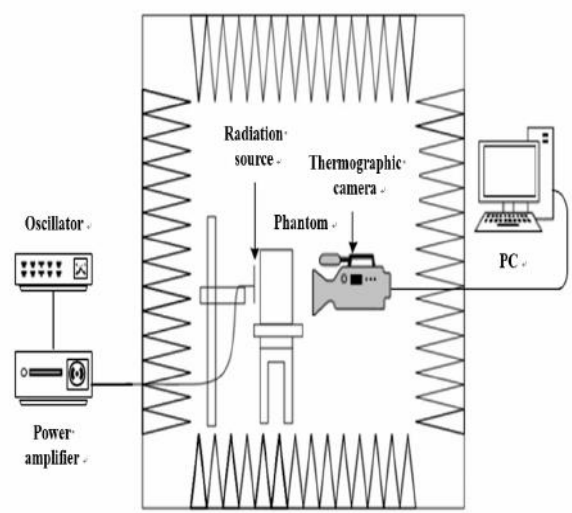
<div align="center">(b)</div>

Fig. 8.2. Measuring SAR by (a) electric field probe method, and (b) thermographic method [133].

probe in a controlled pattern in a liquid phantom to determine the peak local and the average

SAR as shown in Fig. 2(a). In the second method, a thermographic camera records

temperature distribution in phantoms over a specified plane as shown in Fig. 2(b). It is still

a challenge to find a unique standardized method for measuring SAR.

SAR Calculation

In general, SAR analysis is used to measure the amount of electromagnetic energy

absorbed in a lossy dielectric material. The equation for SAR calculation is:

$$SAR = \frac{\sigma}{2\rho} E^2 \qquad (92.1)$$

where σ is the conductivity of the tissue, ρ is the mass density of the mass of tissue per unit

volume and E is the electric field strength inside the tissue.

We studied the SAR calculation in our designed hybrid system that is explanted in

Chapter 3. The time domain solver in HFSS was used to calculate the SAR at the implant

side, the system was tested at all the three UHF bands. The peak SAR values reaches 0.43

W/kg, 0.58 W/kg, and 0.65 W/kg in 10 g of average mass at 415 MHz, 915 MHz, and 1300

MHz, respectively, which is well below the regulatory limit of 2 W/kg averaged over 10 g of tissue based on ICNIRP regulation [114]. Fig. 8.3 shows cross-section of *yz*-plane for the worst-case values of SAR analysis at 1300 MHz. Tthe small dialog box indicates the value for each color.
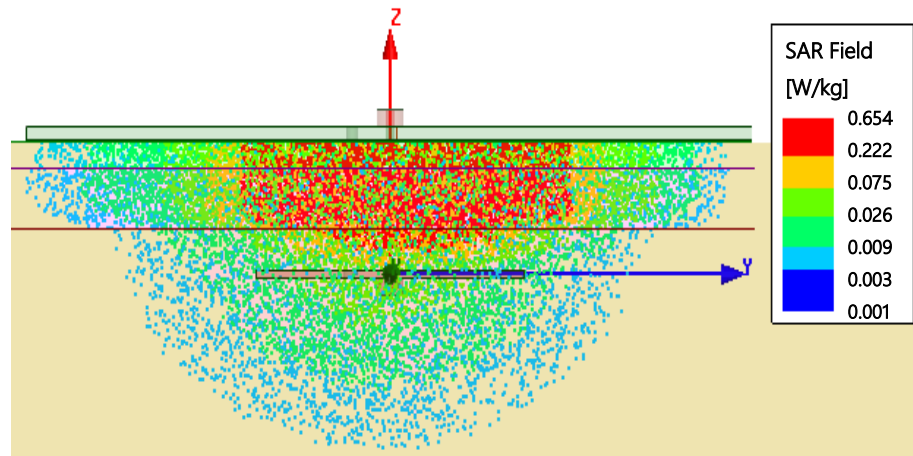
Fig. 8.3. Simulated antenna SAR analysis at 1300 MHz.

8.4   WPT Security

Security is one of the critical issues for WPT. The main interest to offer a secure channel for WPT is to ensure the traditional security properties, integrity, confidentially, and availability [134] of wireless power. Furthermore, communication and data are usually concurrently sent wirelessly. Therefore, the security of communication channel and secrecy of the data is also required. There are several aspects that affect the security of WPT, some of them are described here:

- WPT energy cannot be encrypted or authenticated to ensure the confidentiality of charging a specific device. This will make the WPT channel exposed to the

attack that might threaten the user's security. Moreover, it may also interfere with other communication channels.

- Usually, WPT system has a higher energy and radiated power compared to the communication signal power. As a result, the radiation power level can easily exceed the safety threshold, unless a control system for the WPT channels exists that comply with the safety regulation.

- Wireless power harvesting receivers are very sensitive to the surroundings and environmental conditions, such as the existence of people and devices, absorbing or reflecting materials, temperature and humidity. Unless the receiver has the ability to monitor the environmental conditions, the absence of its security mechanism might lead to unexpected susceptibility in the WPT network.

There are multiple types of security attacks that may affect the WPT safety and security [113], furthermore. The main security issues that the WPT are subjecting to are as follows:

Charging Conflicts

One of the security problems is the charging conflict, which results from charging multiple receivers by multiple transmitters. Suppose that receiver no. 1 is being charged by TX no. 1, if RX no. 2 has a low battery and sends a request to TX no. 2 to start transmitting energy, and once TX no. 2 turns on, RX no. 1 will also receive energy too from TX no. 2. This may cause the energy exposure to exceed the safety threshold limit for a RX no. 1.

An advanced control system is required to detect the possibility of the power transfer in every point and keep the power level at the safety limits. This is a challenging task for

all receivers to keep track of the energy levels beam toward them, which in turn leads to additional energy consumption for them.

Interference Attacks

Interference is generated by surrounding devices, using the same frequency band. The interference can cause a degradation in charging performance. Furthermore, interference might be generated by an attacker in order to interrupt and confuse WPT operations. There are two types of interference attacks, as follows:

Beamforming Attacks

When multiple transmitters emit electromagnetic waves at the same frequency band simultaneously, the received waves by the receiver can be either destructive or constructive. The received power level is bigger than that of the power sent by any individual transmitters if the waves are received in an constructive manner. (in phase). On the other hand, the total received power could be very little and much less than power received by any individual transmitters, if the waves are destructive (out of phase). An attack may generate a destructive interference to threat and disturb the WPT operations. This could potentially lead to fully collapse the system's functionality.

Jamming Attacks

This type of attack is created intentionally to interrupt the communication between the transmitter and the receiver. confusing signals can affect one channel jamming or multiple channels by sweep between all communication channels to jam them all. There are now several attempts to solve this issue, such as detecting the interference by turning off the power transmission periodically and keep watching the channels against outside attacker. However, attackers can also synchronize themselves to the interference detection

period, so that they will remain silent, leading to misdetection. Therefore, more sophisticated methods are required in order to detect the existence of this type of interference.

Spoofing Attacks

If an attacker can snoop on the information that the transmitter and the receiver send/receive to each other such as energy level, and device identity. The attackers may use this information maliciously. For example, the attacker can predict the moment that one receiver will run out of energy. Then attacker may cancel the request signal for power charging just in time in order to prevent the transmitter from sending energy to the required device. Eventually the receiver will run out of power and will stop its operation. A standard solution for spoofing attacks is required by using digital encoding and decoding process to provide both data integrity and security in order to detect the attacking nodes.

Software Attacks

The software application is another source of the attack that can be harmful to the transmitter and the receiver. In this type of attack, a signal is generated to send frequent charging requests to the transmitters, which might interrupt the charging operation or decrease system efficiency. In such cases, it may also force the receivers to stop operating altogether at the same time.

Monitoring Attacks

Monitoring attacks are passive, and it is challenging to detect them since they do not involve any alteration of the data flowing through WPT network. In this type, the attacker can introduce a fake receiver that receives energy from a transmitter to disclose private information without the approval from the users. This type of attack could be as a sensor

106

that collects measurements and notifies an attacker about the potential events inside the WPT network.

There is a solution to detect monitoring attacks by listening to the communication channel periodically in order to detect an information exchange between the fake receiver and an attacker. However, if the disturbance communication is performed on a different channel, detection becomes more complicated.

8.5 Chapter Summary

As a summary the following open issues should be addressed:

a. WPT Safety

- There are currently no specific regulatory guidelines which allow manufacturers to quantify the exposure to power transmission systems. Each standard should consider the range of required delivered power (low, medium, and high) and operating frequency.

- An additional specific safety guideline should be established to protect humans with medical implants.

- Unifying the phantom fabrication procedures at each specific range of frequencies. This will allow and help the researchers to define a WPT safety standards for measuring SAR.

- It is important to compensate the variation in tissue model during phantom fabrication. We recommend development of a set of benchmarking phantoms to study WPT system against them.

- Standardize experimental and numerical simulation procedures for SAR and power exposures should be established.

b. WPT Security

- Better measurement and estimation techniques are required for transmitters by adding sensors to collect the electromagnetic field exposure to obtain the power distribution without any feedback from the receiver.

- More secure systems should be developed to protect WPT devices that are working at the same frequency band.

- A standard solution is required by using digital encoding and decoding process to provide both data integrity and security in order to detect the attacking nodes.

9 CONCLUSION AND FUTURE WORK

9.1 Conclusion

In this research, we present a hybrid system consisting of a novel design of a microstrip antenna that can resonates at various UHF (415 MHz, 905 MHz, and 1300MHz) and a design of HF coil (13.56 MHz). The EX system has 79.6 mm diameter and the IM system has 31.5 mm-diameter. The antennas are using a shorting pin technique to adjust to any of the three resonant frequencies. We consider that the EX antenna/coil combination is placed directly at the outer surface of the skin, and the IM antenna/coil combination is embedded inside the muscle tissue. A layered body model consisting of three tissue layers: the skin layer (3 mm), the fat layer (7 mm), and the muscle layer (125 mm). All three layers have 212 mm $\times$ 212 mm surface area. IM and EX are assumed to be covered by a layer of silicone with a thickness of 100 μm. Both designs were fabricated on an FR-4 substrate. The challenge of minimizing the coupling effect between the coil and the antenna is addressed by optimizing their dimensions. The hybrid system was numerically designed, simulated, fabricated, and measured, antenna part was measured using phantom as a medium to model a muscle tissue whereas air is used as a medium for inductive coil measurement. Also, the performance was tested and measured at varies depths inside a body tissue model, we studied the behavior of S_{21} and η of EX and IM combinations while varying the h depth.

We concluded that at all resonance frequencies f_{oEX} and $f_{oIM,}$ are not sensitive to the change of the depth of implanted antenna inside the tissue. The system provides a good solution for the combination of power transfer and multi-band data communication.

109

The effects of lateral the and angular misalignments between EX and IM combinations are studied too. In lateral misalignment both the EX and IM are located in parallel planes while the lateral distance between their centers was changed from -60 mm to 60 mm, in steps of 10 mm in direction of y-axis. The distance between EX and IM systems was fixed at 15 mm (case 1), and 30 mm (case 2).

We concluded that under lateral misalignment, our design is stable for d ranges from -20 mm to +20 mm at 15 mm depth. Furthermore, at the depth of 30 mm our system is stable for d range from -30 mm to 30 mm.

In angular misalignment, the plane of IM is tilted by an inclined angle while keeping the EX plane unchanged. Inclined angle was changed from -90° to 90°, in steps of 10°, rotating around z-axis. The distance between the centers of EX and IM was kept at 30 mm. it was concluded that the system is stable for θ range from 0° to 60°.

The system was tested too for the effect of rotating IM combination around x-axis while keeping the EX plane unchanged. Rotating angle was changed from 0° to 180°, in steps of 15°. The distance between the centers of EX and IM was kept at 30 mm.

We concluded that the rotating angle has no effect on the values of S_{21} and η for coil at all cases due to its shape symmetry. On the other hand, for the antenna part S_{21} values are stable for angles less than 40° and angles bigger than 150°. However, it has effect for angles between 40° to 150°, the worst case is occurred at 105°.

We also studied the bending effect on the hybrid system design, The EX combination is placed directly at the outer surface of the skin, and the IM that is embedded in a layer of muscle at 30 mm distance away from the EX. IM is considered to be printed on flexible Kapton material. The location of shorting pin to enable the EX and IM antenna to operate

at 905 MHz are optimized too. In order to investigate the impacts of bending IM coil/antenna on the system performance, we conducted the simulations and conditions (*Rad* = 40 mm, 80 mm, and 120 mm)

Two main conclusions are as follow. First, for the inductive link, the system is stable at all three bending conditions (*Rad* = 40 mm*, Rad* = 80 mm*, and Rad* = 120 mm). Second, for the data communication link, the system performance is acceptable under bending up to the radius of *Rad* = 120 mm. However, increasing the bending (decreasing *Rad*) may cause severe loss in communication link and is not recommended.

WPT safety has been studies too, there are currently no specific regulatory guidelines which allow manufacturers to quantify the exposure to power transmission systems. Each standard should consider the range of required delivered power (low, medium, and high) and operating frequency.

In additional specific safety guideline should be established to protect humans with medical implants. And unifying the phantom fabrication procedures at each specific range of frequencies will allow and help the researchers to define a WPT safety standards for measuring SAR.

We concluded that it is important to compensate the variation in tissue model during phantom fabrication. We recommend development of a set of benchmarking phantoms to study WPT system against them and establish a standardize experimental and numerical simulation procedures for SAR and power exposures.

For WPT security a better measurement and estimation techniques are required for transmitters by adding sensors to collect the electromagnetic field exposure to obtain the

power distribution without any feedback from the receiver. And more secure systems should be developed to protect WPT devices that are working at the same frequency band.

9.2   Future Work

More work needs to be done on the optimization scheme, such as expanding the parameters and adding different geometries, including the rectangular-shaped or hexagonal-shaped resonators. In addition, the use of ferrite materials with different implementations can be investigated further. The research can include shielding and take all of the other parts of an electronic device into consideration to investigate their effects on the transmission efficiency of WPT systems.

To extend the transmission distance of the system there are some methods that can be investigated such as:.(1) Multiple series coils which could be used to increase the power efficiency of laterally, axially and angularly misaligned receiver, and (2) optimization of coil geometries with more uniform field distribution.

The use of flexible and bio-compatible materials need to be investigated and their effects on the performance, especially under bending conditions should be studied.

Also adding a switch to antenna design to turn on/off the shorting pin in order to resonate antenna at different frequency could be studied in order to increase the data rate performance.

Finally, the overall system performance and DC-DC performance needs to be carefully studied.

REFERENCES

[1]   Y. K. Tan, *Energy harvesting autonomous sensor systems design, analysis, and practical implementation*. 2013.

[2]   N. Tesla, "System of electric lighting," U.S. Patent 54 622, 1891.

[3]   M. Hutin and M. Lebanc, "Transformer system for electric railways," U.S. Patent 527 857, 1894.

[4]   "Tesla's wireless power experiment." [Online]. Available: http://www.tfcbooks.com/articles/witricity.htm.

[5]   N. Tesla, "System of transmission of electrical energy," U.S. Patent 645 576, 1900.

[6]   T. Sun, X. Xie, and Z. Wang, *Wireless power transfer for medical microsystems*. 2013.

[7]   W. C. Brown, "The History of Power Transmission by Radio Waves," *IEEE Trans. Microw. Theory Tech.*, vol. 32, no. 9, pp. 1230–1242, 1984.

[8]   P. E. Glaser, "Power from the sun: Its future," *Science (80-.).*, vol. 162, no. 3856, pp. 857–861, 1968.

[9]   J. C. Olivares-Galvan, E. Campero-Littlewood, S. Maximov, S. Magdaleno-Adame, and W. Xu, "Wireless power transfer: literature survey," *2013 IEEE Int. Autumn Meet. Power Electron. Comput.*, pp. 1–7, 2013.

[10]   R. Shadid, S. Noghanian, and A. Nejadpak, "A literature survey of wireless power transfer," in *IEEE International Conference on Electro Information Technology*, 2016, vol. 2016–Augus.

[11]   S. Y. R. Hui, W. Zhong, and C. K. Lee, "A critical review of recent progress in mid-range wireless power transfer," *IEEE Transactions on Power Electronics*, vol. 29,

no. 9. pp. 4500–4511, 2014.

[12] D. W. Baarman, F. Innovation, and J. Schwannecke, "Understanding wireless power," *Innovation*, no. December, pp. 1–13, 2009.

[13] A. Kurs, A. Karalis, R. Moffatt, J. D. Joannopoulos, P. Fisher, and M. Soljacic, "Wireless power transfer via strongly coupled magnetic resonances.," *Science*, vol. 317, no. 5834, pp. 83–6, 2007.

[14] B. L. Cannon, J. F. Hoburg, D. D. Stancil, and S. C. Goldstein, "Magnetic Resonant Coupling As a Potential Means for Wireless Power Transfer to Multiple Small Receivers," *IEEE Trans. Power Electron.*, vol. 24, no. 7, pp. 1819–1825, 2009.

[15] T. Imura and Y. Hori, "Maximizing air gap and efficiency of magnetic resonant coupling for wireless power transfer using equivalent circuit and Neumann formula," *IEEE Trans. Ind. Electron.*, vol. 58, no. 10, pp. 4746–4752, 2011.

[16] C. Park, S. Lee, G. H. Cho, and C. T. Rim, "Innovative 5-m-off-distance inductive power transfer systems with optimally shaped dipole coils," *IEEE Trans. Power Electron.*, vol. 30, no. 2, pp. 817–827, 2015.

[17] C. Liu, Y. Guo, and S. Xiao, "A Review of implantable antennas for wireless biomedical devices," *Forum Electromagn. Res. Methods Appl. Technol.*

[18] G. A. Landis, "Re-evaluating satellite solar power systems for earth," in *Conference Record of the 2006 IEEE 4th World Conference on Photovoltaic Energy Conversion, WCPEC-4*, 2007, vol. 2, pp. 1939–1942.

[19] N. Shinohara, "Beam efficiency of wireless power transmission via radio waves from short range to long range," *J. Electromagn. Eng. Sci.*, vol. 10, no. 4, pp. 224–230, 2010.

[20] N. Shinohara, Y. Kubo, and H. Tonomura, "Wireless charging for electric vehicle with microwaves," in *Electric Drives Production Conference (EDPC), 2013 3rd International*, 2013, pp. 1–4.

[21] M. Erol-Kantarci and H. T. Mouftah, "Radio-frequency-based wireless energy transfer in LTE-A heterogenous networks," in *Computers and Communication (ISCC), 2014 IEEE Symposium on*, 2014, pp. 1–6.

[22] K. Huang and X. Zhou, "Cutting the last wires for mobile communications by microwave power transfer," *IEEE Commun. Mag.*, vol. 53, no. 6, pp. 86–93, 2015.

[23] S. A. Ahson and M. Ilyas, *RFID handbook: applications, technology, security, and privacy*. CRC press, 2008.

[24] A. P. Sample, D. J. Yeager, P. S. Powledge, A. V. Mamishev, and J. R. Smith, "Design of an RFID-based battery-free programmable sensing platform," *IEEE Trans. Instrum. Meas.*, vol. 57, no. 11, pp. 2608–2615, 2008.

[25] Y. J. Hong, J. Kang, S. J. Kim, S. J. Kim, and U. K. Kwon, "Ultra-low power sensor platform with wireless charging system," in *ISCAS 2012 - 2012 IEEE International Symposium on Circuits and Systems*, 2012, pp. 978–981.

[26] S. Percy, C. Knight, F. Cooray, and K. Smart, "Supplying the power requirements to a sensor network using radio frequency power transfer.," *Sensors (Basel).*, vol. 12, no. 7, pp. 8571–85, 2012.

[27] C. Cato and S. Lim, "UHF far-field wireless power transfer for remotely powering wireless sensors," in *IEEE Antennas and Propagation Society, AP-S International Symposium (Digest)*, 2014, pp. 1337–1338.

[28] X. Lu, P. Wang, D. Niyato, D. I. Kim, and Z. Han, "Wireless networks with rf energy

harvesting: A contemporary survey," *IEEE Commun. Surv. Tutorials*, vol. 17, no. 2, pp. 757–789, 2015.

[29] C. R. Valenta and G. D. Durgin, "Harvesting wireless power: Survey of energy-harvester conversion efficiency in far-field, wireless power transfer systems," *IEEE Microw. Mag.*, vol. 15, no. 4, pp. 108–120, 2014.

[30] X. Lu, D. Niyato, P. Wang, D. I. Kim, and H. Zhu, "Wireless charger networking for mobile devices: Fundamentals, standards, and applications," *IEEE Wirel. Commun.*, vol. 22, no. 2, pp. 126–135, 2015.

[31] R. Vyas, B. Cook, Y. Kawahara, and M. Tentzeris, "A self-sustaining, autonomous, wireless-sensor beacon powered from long-range, ambient, RF energy," in *Microwave Symposium Digest (IMS), 2013 IEEE MTT-S International*, 2013, pp. 1–3.

[32] X. Wang and A. Mortazawi, "High sensitivity RF energy harvesting from AM broadcasting stations for civilian infrastructure degradation monitoring," in *Wireless Symposium (IWS), 2013 IEEE International*, 2013, pp. 1–3.

[33] L. M. Borges *et al.*, "Design and evaluation of multi-band RF energy harvesting circuits and antennas for WSNs," in *Telecommunications (ICT), 2014 21st International Conference on*, 2014, pp. 308–312.

[34] E. A. Kadir, A. P. Hu, M. Biglari-Abhari, and K. C. Aw, "Indoor WiFi energy harvester with multiple antenna for low-power wireless applications," in *Industrial Electronics (ISIE), 2014 IEEE 23rd International Symposium on*, 2014, pp. 526–530.

[35] A. N. Parks, A. P. Sample, Y. Zhao, and J. R. Smith, "A wireless sensing platform

utilizing ambient RF energy," in *BioWireleSS 2013 - Proceedings: 2013 IEEE Topical Conference on Biomedical Wireless Technologies, Networks, and Sensing Systems - 2013 IEEE Radio and Wireless Week, RWW 2013*, 2013, pp. 154–156.

[36] A. Takacs, H. Aubert, L. Despoisse, and S. Fredon, "Microwave energy harvesting for satellite applications," *Electron. Lett.*, vol. 49, no. 11, pp. 722–724, 2013.

[37] A. Takacs, H. Aubert, S. Fredon, and L. Despoisse, "K-band energy harvesting circuits for satellite application," in *Microwave Conference (EuMC), 2013 European*, 2013, pp. 991–994.

[38] J. O. McSpadden and J. C. Mankins, "Space solar power programs and microwave wireless power transmission technology," *IEEE Microw. Mag.*, vol. 3, no. 4, pp. 46–57, 2002.

[39] J. S. J. S. Ho, S. Kim, and A. S. Y. Poon, "Midfield wireless powering for implantable Systems," *Proc. IEEE*, vol. 101, no. 6, pp. 1369–1378, 2013.

[40] J. C. Schuder, "Powering an artificial heart: birth of the inductively coupled-radio frequency system in 1960," *Artif. Organs*, vol. 26, no. 11, pp. 909–915, 2002.

[41] F. C. Flack, E. D. James, and D. M. Schlapp, "Mutual inductance of air-cored coils: Effect on design of radio-frequency coupled implants," *Med. Bol. Eng.*, vol. 9, no. 2, pp. 79–85, 1971.

[42] J. C. Schuder, J. H. Gold, and H. E. Stephenson, "An inductively coupled RF system for the transmission of 1 kW of power through the skin," *IEEE Trans. Biomed. Eng.*, vol. 18 BME, no. 4, pp. 265–273, 1971.

[43] W. H. Ko, S. P. Liang, and C. D. F. Fung, "Design of radio-frequency powered coils for implant instruments," *Med. Biol. Eng. Comput.*, vol. 15, no. 6, pp. 634–640,

1977.

[44] N. D. Donaldson and T. A. Perkins, "Analysis of resonant coupled coils in the design of radio frequency transcutaneous links," *Med. Biol. Eng. Comput.*, vol. 21, no. 5, pp. 612–627, 1983.

[45] J. A. Von Arx and K. Najafi, "A wireless single-chip telemetry-powered neural stimulation system," *1999 IEEE Int. Solid-State Circuits Conf. Dig. Tech. Pap. ISSCC. First Ed. (Cat. No.99CH36278)*, no. June 1995, pp. 214–215, 1999.

[46] W. J. Heetderks, "RF powering of millimeter- and submillimeter-sized neural prosthetic implants," *IEEE Trans. Biomed. Eng.*, vol. 35, no. 5, pp. 323–327, 1988.

[47] C. M. Zierhofer and E. S. Hochmair, "High-efficiency coupling-insensitive transcutaneous power and data transmission via an inductive link," *IEEE Trans. Biomed. Eng.*, vol. 37, no. 7, pp. 716–722, 1990.

[48] M. Soma, G. DOUGLAS, and R. WHITE, "Radio-frequency coils in implantable devices: misalignment analysis and design procedure," *IEEE Trans. Biomed. Eng.*, vol. BME-34, pp. 276–282, 1987.

[49] K. Van Schuylenbergh and R. Puers, "Self Tuning Inductive Powering For Implantable Telemetric Monitoring Systems," *Proc. Int. Solid-State Sensors Actuators Conf. - TRANSDUCERS '95*, vol. 1, pp. 1–7, 1995.

[50] T. Akin, K. Najafi, and R. M. Bradley, "A wireless implantable multichannel digital neural recording system for a micromachined sieve electrode," *IEEE J. Solid-State Circuits*, vol. 33, no. 1, pp. 109–118, 1998.

[51] O. Knecht, R. Bosshard, and J. Kolar, "High efficiency transcutaneous energy transfer for implantable mechanical heart support systems," *IEEE Trans. Power*

Electron., vol. PP, no. 99, p. 1, 2015.

[52] O. Knecht, R. Bosshard, J. W. Kolar, and C. T. Starck, "Optimization of transcutaneous energy transfer coils for high power medical applications," in *2014 IEEE 15th Workshop on Control and Modeling for Power Electronics, COMPEL 2014*, 2014.

[53] D. Ahn and M. Ghovanloo, "Optimal Design of Wireless Power Transmission Links for Millimeter-Sized Biomedical Implants," *IEEE Trans. Biomed. Circuits Syst.*, vol. PP, no. 99, pp. 1–1, 2015.

[54] S. Mutashar, M. A. Hannan, S. A. Samad, and A. Hussain, "Analysis and optimization of spiral circular inductive coupling link for bio-implanted applications on air and within human tissue," *Sensors (Switzerland)*, vol. 14, no. 7, pp. 11522–11541, 2014.

[55] S. M. Abbas, M. A. Hannan, S. A. Samad, and A. Hussain, "Inductive coupling links for lowest misalignment effects in transcutaneous implanted devices," *Biomed. Tech.*, vol. 59, no. 3, pp. 257–268, 2014.

[56] D. Ahn and S. Hong, "Wireless power transmission with self-regulated output voltage for biomedical implant," *IEEE Trans. Ind. Electron.*, vol. 61, no. 5, pp. 2225–2235, 2014.

[57] M. Zargham and P. G. Gulak, "A 0.13μm CMOS integrated wireless power receiver for biomedical applications," *2013 Proc. ESSCIRC*, pp. 137–140, 2013.

[58] M. Zargham and P. G. Gulak, "Maximum achievable efficiency in near-field coupled power-transfer systems," *IEEE Trans. Biomed. Circuits Syst.*, vol. 6, no. 3, pp. 228–245, 2012.

[59] R. Wu, S. Raju, M. Chan, J. K. O. Sin, and C. P. Yue, "Silicon-embedded receiving coil for high-efficiency wireless power transfer to implantable biomedical ics," *IEEE Electron Device Lett.*, vol. 34, no. 1, pp. 9–11, 2013.

[60] R. F. Xue, K. W. Cheng, and M. Je, "High-efficiency wireless power transfer for biomedical implants by optimal resonant load transformation," *IEEE Trans. Circuits Syst. I Regul. Pap.*, vol. 60, no. 4, pp. 867–874, 2013.

[61] U. Jow and M. Ghovanloo, "Design and optimization of printed spiral coils for efficient transcutaneous inductive power transmission," *IEEE Trans. bio-medical circuits syst*, vol. 1, no. 3, pp. 193–202, 2007.

[62] R. Wu, S. Raju, M. Chan, J. K. O. Sin, and C. P. Yue, "Wireless power link design using silicon-embedded inductors for brain-machine interface," in *2012 International Symposium on VLSI Design, Automation and Test, VLSI-DAT 2012 - Proceedings of Technical Papers*, 2012, pp. 1–4.

[63] M. Ghovanloo and U.-M. Jow, "Modeling and optimization of printed spiral coils in air, saline, and muscle issue environments," *IEEE Trans. bio-medical circuits syst*, vol. 3, no. 5, pp. 339–347, 2009.

[64] M. Baker and R. Sarpeshkar, "Feedback analysis and design of RF power links for low-power bionic systems," *IEEE Trans. Biomed. Circuits Syst.*, vol. 1, no. 1, pp. 28–38, 2007.

[65] R. R. Harrison, "Designing efficient inductive power links for implantable devices," *IEEE Int. Symp. Circuits Syst.*, pp. 2080–2083, 2007.

[66] G. A. Kendir *et al.*, "An optimal design methodology for inductive power link with Class-E amplifier," *IEEE Trans. Circuits Syst. I Regul. Pap.*, vol. 52, no. 5, pp. 857–

866, 2005.

[67] G. Wang, W. Liu, M. Sivaprakasam, and G. A. Kendir, "Design and analysis of an adaptive transcutaneous power telemetry for biomedical implants," *IEEE Trans. Circuits Syst. I Regul. Pap.*, vol. 52, no. 10, pp. 2109–2117, 2005.

[68] M. Catrysse, B. Hermans, and R. Puers, "An inductive power system with integrated bi-directional data-transmission," in *Sensors and Actuators, A: Physical*, 2004, vol. 115, no. 2–3 SPEC. ISS., pp. 221–229.

[69] M. A. Adeeb, A. B. Islam, M. R. Haider, F. S. Tulip, M. N. Ericson, and S. K. Islam, "An inductive link-based wireless power transfer system for biomedical applications," *Act. Passiv. Electron. Components*, vol. 2012, 2012.

[70] M. Kiani, K. Y. Kwon, F. Zhang, K. Oweiss, and M. Ghovanloo, "Evaluation of a closed loop inductive power transmission system on an awake behaving animal subject," in *Proceedings of the Annual International Conference of the IEEE Engineering in Medicine and Biology Society, EMBS*, 2011, pp. 7658–7661.

[71] M. Kiani, U. M. Jow, and M. Ghovanloo, "Design and optimization of a 3 coil inductive link for efficient wireless power transmission," *IEEE Trans. Biomed. Circuits Syst.*, vol. 5, no. 6, pp. 579–591, 2011.

[72] R. Carta, J. Thoné, G. Gosset, G. Cogels, D. Flandre, and R. Puers, "A self-tuning inductive powering system for biomedical implants," in *Procedia Engineering*, 2011, vol. 25, pp. 1585–1588.

[73] K. Ramrakhyani, S. Mirabbasi, Mu Chiao, and C. M, "Design and optimization of resonance-based efficient wireless power delivery systems for biomedical implants.," *IEEE Trans. Biomed. Circuits Syst.*, vol. 5, no. 1, pp. 48–63, 2011.

[74] A. Laskovski and M. Yuce, "Class-E oscillators as wireless power transmitters for biomedical implants," *Proc. 3rd Int. Symp. Appl. Sci. Biomed. Commun. Tech*, pp. 1–5, 2010.

[75] A. Laskovski, M. Yuce, and T. Dissanayake, "Stacked spirals for use in biomedical implants," *Asia Pacific Microw. Conf.*, pp. 389–392, 2009.

[76] M. Kiani and M. Ghovanloo, "An RFID-based closed-loop wireless power transmission system for biomedical applications," *IEEE Trans. Circuits Syst. II Express Briefs*, vol. 57, no. 4, pp. 260–264, 2010.

[77] U. M. Jow and M. Ghovanloo, "Design and optimization of printed spiral coils for efficient inductive power transmission," *IEEE Trans. Biomed. Circuits Syst.*, vol. 1, no. 3, pp. 193–202, 2007.

[78] U. M. Jow and M. Ghovanloo, "Optimization of data coils in a multiband wireless link for neuroprosthetic implantable devices," *IEEE Trans. Biomed. Circuits Syst.*, vol. 4, no. 5, pp. 301–310, 2010.

[79] M. Yin and M. Ghovanloo, "A flexible clockless 32-ch simultaneous wireless neural recording system with adjustable resolution," in *Digest of Technical Papers - IEEE International Solid-State Circuits Conference*, 2009.

[80] M. Ghovanloo and S. Atluri, "A wide-band power-efficient inductive wireless link for implantable microelectronic devices using multiple carriers," *IEEE Trans. Circuits Syst. I Regul. Pap.*, vol. 54, no. 10, pp. 2211–2221, 2007.

[81] C. M. Zierhofer and E. S. Hochmair, "Geometric approach for coupling enhancement of magnetically coupled coils," *IEEE Trans. Biomed. Eng.*, vol. 43, no. 7, pp. 708–714, 1996.

[82] E. S. Hochmair, "System Optimization for Improved Accuracy in Transcutaneous Signal and Power Transmission," *IEEE Trans. Biomed. Eng.*, vol. BME-31, no. 2, pp. 177–186, 1984.

[83] A. Ghahary and B. Cho, "Design of transcutaneous energy transmission system using a series resonant converter," *IEEE Trans. power Electron.*, vol. 7, no. 2, pp. 261–269, 1992.

[84] G. B. Joung and B. H. Cho, "An energy transmission system for an artificial heart using leakage inductance compensation of transcutaneous transformer," *IEEE Trans. power Electron.*, vol. 13, no. 6, pp. 1013–1022, 1998.

[85] E. Hochmair, "System optimization for improved accuracy in transcutaneous signal and power transmission," *IEEE Trans. Biomed. Eng.*, vol. BME-31, no. 2, pp. 177–186, 2007.

[86] A. Ghahary, "Design of transctaneous energy transmission system using Series resonant converter," Univ. Verginia Power Electronic Center, 1989.

[87] T. Sun, X. Xie, G. Li, Y. Gu, Y. Deng, and Z. Wang, "A two-hop wireless power transfer system with an efficiency-enhanced power receiver for motion-free capsule endoscopy inspection," *IEEE Trans. Biomed. Eng.*, vol. 59, no. 12 PART2, pp. 3247–3254, 2012.

[88] M. Ryu, J. D. Kim, H. U. Chin, J. Kim, and S. Y. Song, "Three-dimensional power receiver for in vivo robotic capsules," *Med. Biol. Eng. Comput.*, vol. 45, no. 10, pp. 997–1002, 2007.

[89] R. Carta, N. Pateromichelakis, J. Thoné, M. Sfakiotakis, D. P. Tsakiris, and R. Puers, "A wireless powering system for a vibratory-actuated endoscopic capsule," in

Procedia Engineering, 2010, vol. 5, pp. 572–575.

[90] R. Shadid, S. Sajal, and S. Noghanian, "Efficiency comparison of inductive and microwave power transfer for biomedical applications," in *2017 IEEE AP-S Symposium on Antennas and Propagation and USNC-URSI Radio Science Meeting*, 2017.

[91] M. Zolog, D. Pitică, and O. Pop, "Characterization of spiral planar inductors built on printed circuit boards," in *ISSE 2007 - 30th International Spring Seminar on Electronics Technology 2007; Conference Proceedings: Emerging Technologies for Electronics Packaging*, 2007, pp. 308–313.

[92] "Institute of Applied Physics (IFAC)." [Online]. Available: http://niremf.ifac.cnr.it/tissprop/htmlclie/htmlclie.php.

[93] "Roger Corporation." [Online]. Available: www.rogercorp.com.

[94] "Ansys, Inc." [Online]. Available: www.ansoft.com.

[95] G. Clark, *Cochlear implants : fundamentals and applications*. 2003.

[96] J. D. Weiland and M. S. Humayun, "Retinal prosthesis," *IEEE Trans. Biomed. Eng.*, vol. 61, no. 5, pp. 1412–1424, 2014.

[97] C. Hannachi and S. O. Tatu, "Performance comparison of 60 GHz printed patch antennas with different geometrical shapes using miniature hybrid microwave integrated circuits technology," *IET Microwaves, Antennas Propag.*, vol. 11, no. 1, pp. 106–112, 2017.

[98] R. Chair, K. M. Luk, and K. F. Lee, "Small dual patch antenna," *Electron. Lett.*, vol. 35, no. 10, p. 762, 1999.

[99] C. Y. Chiu, C. H. Chan, and K. M. Luk, "Small dual-band antenna with folded-patch

technique," *IEEE Antennas Wirel. Propag. Lett.*, vol. 3, no. 1, pp. 108–110, 2004.

[100] Xueyi Yu, Guolin Li, and Zhihua Wang, "Design of Compact 2.45 GHz Microstrip Antenna," in *2005 IEEE International Symposium on Microwave, Antenna, Propagation and EMC Technologies for Wireless Communications*, 2005, vol. 1, pp. 153–156.

[101] V. V. Thakare, P. Singhal, and K. Das, "Calculation of Microstrip antenna bandwidth using Artificial Neural Network," *2008 IEEE Int. RF Microw. Conf.*, pp. 404–406, 2008.

[102] R. Shadid and S. Noghanian, "Hybrid power transfer and wireless antenna system design for biomedical implanted devices," in *ACES Conference in Denver*, 2018.

[103] S. Babic, F. Sirois, C. Akyel, and C. Girardi, "Mutual inductance calculation between circular filaments arbitrarily positioned in space: Alternative to grover's formula," *IEEE Trans. Magn.*, vol. 46, no. 9, pp. 3591–3600, 2010.

[104] M. Q. Nguyen, Z. Hughes, P. Woods, Y.-S. Seo, S. Rao, and J.-C. Chiao, "Field Distribution Models of Spiral Coil for Misalignment Analysis in Wireless Power Transfer Systems," *IEEE Trans. Microw. Theory Tech.*, vol. 62, no. 4, pp. 920–930, 2014.

[105] M. R. Shah, R. P. Phillips, and R. A. Normann, "A study of printed spiral coils for neuroprosthetic transcranial telemetry applications," *IEEE Trans. Biomed. Eng.*, vol. 45, no. 7, pp. 867–876, 1998.

[106] K. Fotopoulou and B. W. Flynn, "Wireless power transfer in loosely coupled links: Coil misalignment model," *IEEE Trans. Magn.*, vol. 47, no. 2 PART 2, pp. 416–430, 2011.

[107] J. Kim *et al.*, "Miniaturized Flexible Electronic Systems with Wireless Power and Near-Field Communication Capabilities," *Adv. Funct. Mater.*, vol. 25, no. 30, pp. 4761–4767, 2015.

[108] T. Yilmaz, R. Foster, and Y. Hao, "Broadband tissue mimicking phantoms and a patch resonator for evaluating noninvasive monitoring of blood glucose levels," *IEEE Trans. Antennas Propag.*, vol. 62, no. 6, pp. 3064–3075, 2014.

[109] Z. N. Low, R. A. Chinga, R. Tseng, and J. Lin, "Design and test of a high-power high-efficiency loosely coupled planar wireless power transfer system," *IEEE Trans. Ind. Electron.*, vol. 56, no. 5, pp. 1801–1812, 2009.

[110] Siqi Li and C. C. Mi, "Wireless Power Transfer for Electric Vehicle Applications," *IEEE J. Emerg. Sel. Top. Power Electron.*, vol. 3, no. 1, pp. 4–17, 2015.

[111] A. Sharma, E. Kampianakis, and M. S. Reynolds, "A Dual-band HF and UHF antenna system for implanted neural recording and stimulation devices," *IEEE Antennas Wirel. Propag. Lett.*, vol. 16, pp. 493–496, 2017.

[112] J. M. Osepchuk and R. C. Petersen, "Safety standards for exposure to RF electromagnetic fields," *IEEE Microw. Mag.*, vol. 2, no. 2, 2001.

[113] Q. Liu, K. S. Yildirim, P. Pawełczak, and M. Warnier, "Safe and secure wireless power transfer networks: challenges and opportunities in RF-based systems," *IEEE Commun. Mag.*, vol. 54, no. 9, pp. 74–79, 2016.

[114] International Commission on Non-Ionizing Radiation Protection, "GUIDELINES FOR LIMITING EXPOSURE TO TIME-VARYING ELECTRIC, MAGNETIC, AND ELECTROMAGNETIC FIELDS (UP TO 300 GHz)," *Health Phys.*, vol. 75, no. 5, p. 535, 1998.

[115] "High Frequency Review of International Commission on Non-Ionizing Radiation Protection (ICNIRP)," 2009. [Online]. Available: http://www.icnirp.org/en/publications/article/hf-review-2009.html.

[116] IEEE, *IEEE Standard for Safety Levels with Respect to Human Exposure to Radio Frequency Electromagnetic Fields, 3 kHz to 300 GHz, C95.1*. 1992.

[117] IEEE, *IEEE Standard for Safety Levels With Respect to Human Exposure to Radio Frequency Electromagnetic Fields, 3 kHz to 300 GHz*, vol. 2005, no. April. 2006.

[118] H. M. Madjar, "Human radio frequency exposure limits: An update of reference levels in Europe, USA, Canada, China, Japan and Korea," in *IEEE International Symposium on Electromagnetic Compatibility*, 2016, vol. 2016–Novem, pp. 467–473.

[119] A. Kyriakou, A. Christ, E. Neufeld, and N. Kuster, "Local tissue temperature increase of a generic implant compared to the basic restrictions defined in safety guidelines," *Bioelectromagnetics*, vol. 33, no. 5, pp. 366–374, 2012.

[120] A. Christ *et al.*, "The Virtual Family - Development of surface-based anatomical models of two adults and two children for dosimetric simulations," *Phys. Med. Biol.*, vol. 55, no. 2, 2010.

[121] M. Caon, "Voxel-based computational models of real human anatomy: A review," *Radiation and Environmental Biophysics*, vol. 42, no. 4. pp. 229–235, 2004.

[122] T. Nagaoka *et al.*, "Development of realistic high-resolution whole-body voxel models of Japanese adult males and females of average height and weight, and application of models to radio-frequency electromagnetic-field dosimetry," *Phys. Med. Biol.*, vol. 49, no. 1, pp. 1–15, 2004.

[123] H. Zaidi and X. G. Xu, "Computational Anthropomorphic Models of the Human Anatomy: The Path to Realistic Monte Carlo Modeling in Radiological Sciences," *Annu. Rev. Biomed. Eng.*, vol. 9, no. 1, pp. 471–500, 2007.

[124] H. Zaidi and B. M. W. Tsui, "Review of computational anthropomorphic anatomical and physiological models," *Proceedings of the IEEE*, vol. 97, no. 12. pp. 1938–1953, 2009.

[125] O. P. Gandhi, L. L. Morgan, A. A. De Salles, Y. Y. Han, R. B. Herberman, and D. L. Davis, "Exposure Limits: The underestimation of absorbed cell phone radiation, especially in children," *Electromagnetic Biology and Medicine*, vol. 31, no. 1. pp. 34–51, 2012.

[126] M. J. Edwards, R. D. Saunders, and K. Shiota, "Effects of heat on embryos and foetuses," in *International Journal of Hyperthermia*, 2003, vol. 19, no. 3, pp. 295–324.

[127] M. C. Gosselin *et al.*, "Development of a new generation of high-resolution anatomical models for medical device evaluation: The Virtual Population 3.0," *Phys. Med. Biol.*, vol. 59, no. 18, pp. 5287–5303, 2014.

[128] Y. P. Shkolnikov and W. H. Bailey, "Electromagnetic interference and exposure from household wireless networks," in *ISPCE 2011 - 2011 IEEE Symposium on Product Compliance Engineering, Proceedings*, 2011.

[129] T. Karacolak, A. Z. Hood, and E. Topsakal, "Design of a dual-band implantable antenna and development of skin mimicking gels for continuous glucose monitoring," *IEEE Trans. Microw. Theory Tech.*, vol. 56, no. 4, pp. 1001–1008, 2008.

[130] Agilent Technologies, "Basics of Measuring the Dielectric Properties of Materials," *Appl. Note*, pp. 1–32, 2006.

[131] J. L. Schepps and K. R. Foster, "The UHF and microwave dielectric properties of normal and tumour tissues: Variation in dielectric properties with tissue water content," *Phys. Med. Biol.*, vol. 25, no. 6, pp. 1149–1159, 1980.

[132] K. N. Bocan, M. H. Mickle, and E. Sejdic, "Multi-Disciplinary Challenges in Tissue Modeling for Wireless Electromagnetic Powering: A Review," *IEEE Sens. J.*, vol. 17, no. 20, pp. 6498–6509, 2017.

[133] J. C. Wang, E. G. Lim, M. Leach, Z. Wang, and K. L. Man, "Review of SAR measurement methods in relation to wearable devices," *Engineering Letters*, vol. 24, no. 3. pp. 256–262, 2016.

[134] W. Trappe, R. Howard, and R. S. Moore, "Low-energy security: Limits and opportunities in the internet of things," *IEEE Secur. Priv.*, vol. 13, no. 1, pp. 14–21, 2015.

Publications resulted from this research:

1- R. Shadid and S. Noghanian, "A Literature Survey on Wireless Power Transfer for Biomedical Devices," accepted in International Journal of Antennas and Propagation (Hindawi 2018).

2- R. Shadid and S. Noghanian, "Hybrid power transfer and wireless antenna system design for biomedical implanted devices," accepted in 2018 ACES Conference in Denver, Colarodo.

3- R. Shadid and S. Noghanian, "Study of misalignment effects on hybrid power transfer and wireless antenna system for implanted devices," accepted in 2018 IEEE AP-S Symposium on Antennas and Propagation and USNC-URSI Radio Science Meeting, Boston, 2018.

4- R. Shadid and S. Noghanian, "Study of Bending Effect on Hybrid Power Transfer and Wireless Antenna System for Implanted Devices," are submitted to 2018 - 18th International Symposium on Antenna Technology and Applied Electromagnetics (ANTEM conference, 2018).

5- R. Shadid and S. Noghanian, "Hybrid Inductive Power Transfer and Wireless Multi-Band Antenna System for Biomedical Implanted Devices" are planned to be submitted to PIER Journal.

6- R. Shadid, S. Noghanian, and A. Nejadpak, "A literature survey of wireless power transfer," in IEEE International Conference on Electro Information Technology, August 2016.

7- R. Shadid, S. Sajal, and S. Noghanian, "Efficiency comparison of inductive and microwave power transfer for biomedical applications," in 2017 IEEE AP-S Symposium on Antennas and Propagation and USNC-URSI Radio Science Meeting, 2017.